

# Modeling PWR Fuel Corrosion Product Deposition and Growth Processes



**WARNING:**  
Please read the Export Control  
and License Agreement on the  
back cover before removing the  
Wrapping Material.

*Technical Report*

---



# **Modeling PWR Fuel Corrosion Product Deposition and Growth Processes**

**1009734**

Interim Report, December, 2004

EPRI Project Manager  
J. Deshon

## **DISCLAIMER OF WARRANTIES AND LIMITATION OF LIABILITIES**

THIS DOCUMENT WAS PREPARED BY THE ORGANIZATION(S) NAMED BELOW AS AN ACCOUNT OF WORK SPONSORED OR COSPONSORED BY THE ELECTRIC POWER RESEARCH INSTITUTE, INC. (EPRI). NEITHER EPRI, ANY MEMBER OF EPRI, ANY COSPONSOR, THE ORGANIZATION(S) BELOW, NOR ANY PERSON ACTING ON BEHALF OF ANY OF THEM:

(A) MAKES ANY WARRANTY OR REPRESENTATION WHATSOEVER, EXPRESS OR IMPLIED, (I) WITH RESPECT TO THE USE OF ANY INFORMATION, APPARATUS, METHOD, PROCESS, OR SIMILAR ITEM DISCLOSED IN THIS DOCUMENT, INCLUDING MERCHANTABILITY AND FITNESS FOR A PARTICULAR PURPOSE, OR (II) THAT SUCH USE DOES NOT INFRINGE ON OR INTERFERE WITH PRIVATELY OWNED RIGHTS, INCLUDING ANY PARTY'S INTELLECTUAL PROPERTY, OR (III) THAT THIS DOCUMENT IS SUITABLE TO ANY PARTICULAR USER'S CIRCUMSTANCE; OR

(B) ASSUMES RESPONSIBILITY FOR ANY DAMAGES OR OTHER LIABILITY WHATSOEVER (INCLUDING ANY CONSEQUENTIAL DAMAGES, EVEN IF EPRI OR ANY EPRI REPRESENTATIVE HAS BEEN ADVISED OF THE POSSIBILITY OF SUCH DAMAGES) RESULTING FROM YOUR SELECTION OR USE OF THIS DOCUMENT OR ANY INFORMATION, APPARATUS, METHOD, PROCESS, OR SIMILAR ITEM DISCLOSED IN THIS DOCUMENT.

ORGANIZATION(S) THAT PREPARED THIS DOCUMENT

**BNFL, Nuclear Sciences and Technology Services**

## **ORDERING INFORMATION**

Requests for copies of this report should be directed to EPRI Orders and Conferences, 1355 Willow Way, Suite 278, Concord, CA 94520, (800) 313-3774, press 2 or internally x5379, (925) 609-9169, (925) 609-1310 (fax).

Electric Power Research Institute and EPRI are registered service marks of the Electric Power Research Institute, Inc. EPRI. ELECTRIFY THE WORLD is a service mark of the Electric Power Research Institute, Inc.

Copyright © 2004 Electric Power Research Institute, Inc. All rights reserved.

# CITATIONS

---

This report was prepared by

BNFL  
Nuclear Sciences and Technology Services  
Building 168 Harwell International Business Centre  
Didcot, Oxfordshire, UK, OX11 0QJ

Principal Investigators

S. Dickinson  
J. Henshaw  
J. C. McGurk  
H. E. Sims  
A. Tuson

This report describes research sponsored by EPRI.

The report is a corporate document that should be cited in the literature in the following manner:

*Modeling PWR Fuel Corrosion Product Deposition and Growth Processes*, EPRI, Palo Alto, CA: 2004. 1009734.



# REPORT SUMMARY

---

Development of axial offset anomaly (AOA) in pressurized water reactors (PWRs) drove industry to conduct crud scrape campaigns at a number of units to characterize and better understand the material being deposited on the fuel clad surface. This report describes the first phase of a program to develop models that describe the crud deposition and growth process, including the many phenomena that influence not only the deposit mass, but the composition. The models will be benchmarked against published crud scrape data.

## Background

A number of PWRs operating at high duty and for long cycles have shown a discrepancy between the measured axial offset (AO) and calculated AO, resulting in the AOA phenomenon. AOA is due to boron entrainment in fuel crud in the top part of the core. Significant crud buildup in this region is necessary for AOA to manifest, and this buildup occurs because of enhanced sub-cooled nucleate boiling on the clad surface for high-duty plants. Results from several PWR crud scrape campaigns have shown that crud mass and composition vary between plant to plant and from those units that have and have not experienced AOA. This prompted the desire to explain why crud from these units could be so different and which system parameters had the greatest influence in the differences.

## Objectives

- To understand the conditions external to and within the crud (pH, temperature, redox) and the consequences of these conditions in explaining several observations that have been made on fuel crud scrape samples.
- To understand the relative importance of soluble and insoluble material in the coolant leading to crud buildup.
- To understand the form of boron within the crud (soluble, crystalline, or adsorbed).

## Approach

Two computer models were developed, one to examine crud deposition processes and the other to simulate the conditions inside the fuel crud. The deposition model simulated mass transfer processes in the core region, calculating the extent of soluble material in the system using thermodynamics. Conditions within the crud were simulated using a new wick boiling model that couples thermal hydraulics and chemistry. This model calculates the effect of soluble material on the saturation temperature, which influences the heat transport through the crud, which in turn alters species concentrations.

## Results

The crud deposition model indicates that the amount of soluble material within the coolant is sufficient to lead to thick crud deposits when sufficient sub-cooled nucleate boiling occurs. Both lithium and boron concentrate in the crud as water is evaporated, and this concentration process leads to an increase in saturation temperature and an increase in crud temperature. Since the enthalpy of vaporization of water falls with increasing temperature, heat loss due to evaporation decreases, leading to high temperatures in thick deposits (> 60 $\mu$ m). Temperatures may be near or above the critical temperature of water, and such extreme conditions may be why the mineral bonaccordite has been observed in thick crud deposits. Since the solubility of lithium metaborate (LiBO<sub>2</sub>) falls with increasing temperature, this mineral precipitates out when crud thickness is approximately 35 $\mu$ m, which also is the point at which AOA has been observed, based on the crud scrape data. The crud chemistry model, therefore, explains a number of the crud scrape observations.

## EPRI Perspective

This work describes the first phase of model development designed to evaluate known chemical and physical phenomena that lead to crud buildup at the clad surface of PWRs. For those phenomena that have been incorporated into the model thus far, sensitivity studies have been conducted to gauge the relative importance (impact) of each. As additional processes are introduced into the model, the model output will be compared to results from published crud scrape campaigns (EPRI reports 1003129, *Characterization of Corrosion Products on the Callaway Cycle 9 PWR Core*, and 1009951, *Evaluation of Fuel Clad Corrosion Product Deposits and Circulating Corrosion Products in PWRs*). A follow-on report is anticipated in 2005, which will complete the current work. It is anticipated the final report will offer reasonable explanations for the measured results observed from the crud scrape campaigns and provide insight to the crud deposition and growth process and the development of AOA.

## Keywords

Axial offset anomaly

AOA

Crud

PWR Crud

Crud modeling

# ACKNOWLEDGEMENTS

---

The authors of this report would like to thank the staff at EPRI, NII, British Energy and Westinghouse for their helpful support of this work. In particular, thanks are given to Haydn Starkie (NII), Jeff Deshon (EPRI), Art Byers, Dave Chapman (Westinghouse), Keith Garbett, Ed Thornton and Chris Bates (BE).



## EXECUTIVE SUMMARY

---

Two models have been used to investigate crud deposition and growth and axial offset anomaly (AOA) problems in PWR reactors; the crud deposition model (CDM) models the crud deposition process; the crud chemistry model (CCM) models the chemistry inside the crud. These models are based on fundamental physical and chemical principles and do not involve any fitting of parameters to plant data. CDM uses thermodynamic data for nickel ferrite ( $\text{NiFe}_2\text{O}_4$ ) and calculated mass transfer rates to estimate the amount of soluble material likely to deposit on fuel pins undergoing sub-cooled nucleate boiling. CCM is a wick boiling model that is coupled to the chemistry taking place inside the crud. This coupling occurs because the species concentrations in the crud affect the water saturation temperature, which affects the heat transport in the wick boiling model. CCM models boron/lithium chemistry, Ni/Fe chemistry and water radiolysis. Partitioning of volatile species such as  $\text{H}_2$ ,  $\text{O}_2$  and  $\text{H}_3\text{BO}_3$ , as well various precipitation processes are also modeled.

Calculations with the CDM indicate:

- Soluble material can account for crud deposits 10 – 100 $\mu\text{m}$  thick under boiling conditions over a 12month cycle.
- Decreasing the amount of soluble material by increasing Li, decreasing B or decreasing  $\text{H}_2$  will lower the amount of crud. Sensitivity studies with CDM indicate the relative importance of the parameters in determining crud thickness are heat flux > [B] > [ $\text{H}_2$ ] > [Li].

Calculations with the CCM indicate:

- $\text{LiBO}_2(\text{s})$  precipitates out for a crud thickness typical of that observed in AOA plants, and for typical plant conditions this starts at a crud thickness of approximately 35 $\mu\text{m}$ .
- There is a significant amount of soluble boron in thick crud (on the order of 4M).
- The temperature at the bottom of the crud can be as large as 400°C for thick crud. This might explain the formation of bonaccordite within the crud.
- Significant local concentrations (10s – 100s ppb) of hydrogen peroxide can be generated in the crud under certain operational conditions.
- The calculated pH variation through the crud may explain the layer of  $\text{ZrO}_2$  that has been observed in thick crud deposits.

The work presented in this report utilized models still in the development phase and further expansion and refinement of the models are required before they provide a more complete picture of crud deposition and crud chemistry. These developments are outlined in the report.



# CONTENTS

---

<b>1 INTRODUCTION .....</b>	<b>1-1</b>
<b>2 CRUD DEPOSITION MODEL (CDM).....</b>	<b>2-1</b>
2.1 Soluble Species Equations.....	2-3
2.2 Insoluble Species Equations .....	2-4
2.3 Chemistry used in CDM .....	2-5
<b>3 CRUD DEPOSITION MODEL (CDM) RESULTS .....</b>	<b>3-1</b>
<b>4 CRUD CHEMISTRY MODEL (CCM).....</b>	<b>4-1</b>
4.1 Physical basis of CCM .....	4-2
4.1.1 Thermal hydraulics .....	4-2
4.1.2 Transport in The Porous Shell.....	4-5
4.1.3 Partitioning and transport of volatile species .....	4-6
4.1.4 Analytical solution.....	4-8
4.2 Chemistry used in CCM .....	4-9
4.3 Thermodynamic Problems .....	4-12
4.3.1 Equilibrium expressions.....	4-12
4.3.2 Calculation of Non-ideal parameters .....	4-15
4.3.3 Saturation temperature.....	4-18
4.3.4 Vaporization enthalpy of water .....	4-19
4.4 High Temperature Water and Solution Properties .....	4-20
4.4.1 Pure water properties .....	4-20
4.4.2 Solution properties.....	4-21
4.4.3 Heat Transfer Parameters .....	4-25
<b>5 RESULTS FROM CRUD CHEMISTRY MODEL (CCM).....</b>	<b>5-1</b>
5.1 Standard Operating Conditions .....	5-1
5.2 Lithium.....	5-9

5.3 Boron.....	5-12
5.4 Hydrogen.....	5-16
5.5 Heat Flux.....	5-16
5.6 Neutron Flux.....	5-19
5.7 Calculations under plant conditions.....	5-21
<b>6 DISCUSSION.....</b>	<b>6-1</b>
<b>7 CONCLUSIONS .....</b>	<b>7-1</b>
<b>8 RECOMMENDATIONS - MODEL DEVELOPMENTS.....</b>	<b>8-1</b>
8.1 Physical Parameters .....	8-1
Enthalpy of vaporization .....	8-1
Evaporative heat coefficient .....	8-1
Convection.....	8-1
Thermal conductivity of water.....	8-2
8.2 Chemistry Parameters.....	8-2
Boric Acid Adsorption .....	8-2
MULTEQ data.....	8-2
High Temperature Radiolysis Rate Constant .....	8-2
Ni/Fe Radiolysis Chemistry .....	8-2
8.3 General .....	8-3
<b>9 REFERENCES .....</b>	<b>9-1</b>
 <b>A APPENDIX A: NI-FE THERMODYNAMICS AND DEPOSITION TRANSPORT</b>	
<b>COEFFICIENTS.....</b>	<b>A-1</b>
Thermodynamics.....	A-1
Deposition and Transfer coefficients.....	A-3
Mass Flux equations .....	A-6
References.....	A-6
 <b>B APPENDIX B: D CHAPMAN (WESTINGHOUSE) CALCULATION OF PLANT</b>	
<b>OPERATING CONDITIONS.....</b>	<b>B-1</b>
Methodology and Calculations .....	B-1
Radiation Data (Monte Carlo Calculations) .....	B-1
Description of Models .....	B-2

Description of the Source .....	B-3
Variance Reduction .....	B-3
Radiation Environment Tallies .....	B-3
Nuclear Data.....	B-3
Results.....	B-3
Conclusions.....	B-4
References .....	B-5
<b>C APPENDIX C: NUMERICAL SOLUTION OF CCM .....</b>	<b>C-1</b>
Numerical Solution of CCM.....	C-1
Thermal Hydraulic Equations .....	C-1
Transport and chemical kinetic equations .....	C-4
References.....	C-7
<b>D APPENDIX D: USING THE FACSIMILE CCM .....</b>	<b>D-1</b>
FACSIMILE CCM .....	D-1
References .....	D-4
<b>E APPENDIX E: THE <math>^{10}\text{B}(\text{N}, \alpha)^7\text{Li}</math> REACTION.....</b>	<b>E-1</b>
Neutron Fluxes .....	E-3
References .....	E-3



## LIST OF FIGURES

---

Figure 2-1 Schematic diagram of modelled loop components along with soluble species transport constants.....	2-2
Figure 3-1 Plot of crud thickness on the boiling fuel surface against applied heat flux. Calculation for 1200ppm B, 2ppm Li and 25 cc kg <sup>-1</sup> (STP) H <sub>2</sub> .....	3-3
Figure 3-2 Plot of crud thickness on the boiling fuel surface against bulk hydrogen concentration. Calculation for 1200ppm B and a heat flux of 5x10 <sup>5</sup> Wm <sup>-2</sup> .....	3-3
Figure 3-3 Plot of crud thickness on the boiling fuel surface against bulk lithium concentration. Calculation for 1200ppm B and a heat flux of 1x10 <sup>6</sup> Wm <sup>-2</sup> .....	3-4
Figure 3-4 Plot of crud thickness on the boiling fuel surface against bulk boron concentration. Calculation for [Li] of 1ppm and a heat flux of 1x10 <sup>6</sup> Wm <sup>-2</sup> .....	3-4
Figure 3-5 Plot of crud thickness on the boiling and non-boiling fuel surface against bulk particulate concentration. Calculation for [B] = 1200ppm, [Li] 2ppm, H <sub>2</sub> 25cc kg <sup>-1</sup> (STP) and a heat flux of 1x10 <sup>6</sup> Wm <sup>-2</sup> .....	3-5
Figure 4-1 Calculated points and fitted polynomial line for saturation temperature as a function of the activity of water.....	4-24
Figure 4-2 Vaporization enthalpy of water in solution, H <sub>v</sub> , and of pure water, H <sub>v</sub> <sup>0</sup> versus temperature.....	4-25
Figure 5-1 Temperature and amount of LiBO <sub>2</sub> (s) at the bottom of the deposit verses deposit depth. Conditions: Boron 1200 ppm, Lithium 2 ppm, Heat Flux = 1.0 MW m <sup>-2</sup> , Bulk H <sub>2</sub> = 25cc(STP) kg <sup>-1</sup> .....	5-3
Figure 5-2 pH and crud temperature against deposit depth for a 35μm thick deposit. Calculation with 2ppm Li, 1200ppm B and 25cm <sup>3</sup> kg <sup>-1</sup> (STP) H <sub>2</sub> .....	5-3
Figure 5-3 Boric acid and lithium ion concentration against depth for a 35μm thick deposit. Calculation with 2ppm Li, 1200ppm B and 25cm <sup>3</sup> kg <sup>-1</sup> (STP) H <sub>2</sub> .....	5-4
Figure 5-4 Soluble Ni/Fe ratio against depth for a 35μm thick deposit. Calculation with 2ppm Li, 1200ppm B and 25cm <sup>3</sup> kg <sup>-1</sup> (STP) H <sub>2</sub> .....	5-4
Figure 5-5 H <sub>2</sub> , H <sub>2</sub> O <sub>2</sub> and OH against depth for a 35μm thick deposit. Calculation with 2ppm Li, 1200ppm B and 25cm <sup>3</sup> kg <sup>-1</sup> (STP) H <sub>2</sub> .....	5-6
Figure 5-6 pH, Li <sup>+</sup> , Boric acid concentration and amount of LiBO <sub>2</sub> (s) against depth for a 59μm thick deposit. Calculation with 2ppm Li, 1200ppm B and 25cm <sup>3</sup> kg <sup>-1</sup> (STP) H <sub>2</sub> .....	5-6
Figure 5-7 Deposit temperature against depth for a 59μm thick deposit. Calculation with 2ppm Li, 1200ppm B and 25cm <sup>3</sup> kg <sup>-1</sup> (STP) H <sub>2</sub> .....	5-7
Figure 5-8 Soluble Ni/Fe ratio against depth for a 35μm thick deposit. Calculation with 2ppm Li, 1200ppm B and 25cm <sup>3</sup> kg <sup>-1</sup> (STP) H <sub>2</sub> .....	5-7
Figure 5-9 H <sub>2</sub> , H <sub>2</sub> O <sub>2</sub> and OH against depth for a 59μm thick deposit. Calculation with 2ppm Li, 1200ppm B and 25cm <sup>3</sup> kg <sup>-1</sup> (STP) H <sub>2</sub> .....	5-8

Figure 5-10 H <sub>2</sub> O <sub>2</sub> plotted against H <sub>2</sub> through part of the 59 μm thick deposit. Calculation with 2ppm Li, 1200ppm B and 25cm <sup>3</sup> kg <sup>-1</sup> (STP) H <sub>2</sub> .....	5-8
Figure 5-11 Temperature at the bottom of the deposit against crud thickness for initial Li concentrations of 1, 2 and 3ppm.....	5-10
Figure 5-12 Amount of LiBO <sub>2</sub> (s) at the bottom of the deposit against crud thickness for initial Li concentrations of 1, 2 and 3ppm.....	5-10
Figure 5-13 pH at the bottom of the deposit against crud thickness for initial Li concentrations of 1, 2 and 3ppm.....	5-11
Figure 5-14 Total soluble boron at the bottom of the deposit against crud thickness for initial Li concentrations of 1, 2 and 3ppm.....	5-11
Figure 5-15 H <sub>2</sub> O <sub>2</sub> concentration at the bottom of the deposit against crud thickness for initial Li concentrations of 1, 2 and 3ppm.....	5-12
Figure 5-16 Temperature at bottom of deposit against crud thickness for initial boron concentrations of 300, 600, 1200 and 1800 ppm.....	5-13
Figure 5-17 Amount of LiBO <sub>2</sub> (s) at the bottom of deposit against crud thickness for initial boron concentrations of 300, 600, 1200 and 1800 ppm.....	5-14
Figure 5-18 pH at the bottom of deposit against crud thickness for initial boron concentrations of 300, 600, 1200 and 1800 ppm.....	5-14
Figure 5-19 Concentration of H <sub>2</sub> O <sub>2</sub> at the bottom of deposit against crud thickness for initial boron concentrations of 300, 600, 1200 and 1800 ppm.....	5-15
Figure 5-20 Concentration of H <sub>2</sub> through an approximate 60μm deposit for initial boron concentrations of 300, 600, 1200 and 1800 ppm.....	5-15
Figure 5-21 Concentration of H <sub>2</sub> O <sub>2</sub> at the bottom of deposit against crud thickness for initial H <sub>2</sub> concentrations of 5, 10, 25 and 50 cm <sup>3</sup> kg <sup>-1</sup> (STP).....	5-17
Figure 5-22 Temperature at the bottom of deposit against crud thickness for initial heat fluxes (HF) of 0.1, 0.5, 0.75 and 1MWm <sup>-2</sup> .....	5-17
Figure 5-23 Amount of LiBO <sub>2</sub> (s) at the bottom of deposit against crud thickness for initial heat fluxes (HF) of 0.1, 0.5, 0.75 and 1MWm <sup>-2</sup> .....	5-18
Figure 5-24 Concentration of soluble boron at the bottom of deposit against crud thickness for initial heat fluxes (HF) of 0.1, 0.5, 0.75 and 1MWm <sup>-2</sup> .....	5-18
Figure 5-25 Concentration of H <sub>2</sub> O <sub>2</sub> at the bottom of deposit against crud thickness for initial heat fluxes (HF) of 0.1, 0.5, 0.75 and 1MWm <sup>-2</sup> .....	5-19
Figure 5-26 Concentration of H <sub>2</sub> O <sub>2</sub> against depth for a 35μm deposit. Calculations for two neutron fluxes (NF) 3.6x10 <sup>14</sup> and 7.2x10 <sup>14</sup> cm <sup>-2</sup> s <sup>-1</sup> .....	5-20
Figure 5-27 Concentration of H <sub>2</sub> O <sub>2</sub> against depth for a 59μm deposit. Calculations for two neutron fluxes (NF) 3.6x10 <sup>14</sup> and 7.2x10 <sup>14</sup> cm <sup>-2</sup> s <sup>-1</sup> .....	5-20
Figure 5-28 Vogtle 2 Cycle 9 plot of pH, Li <sup>+</sup> , Boric acid concentration and amount of LiBO <sub>2</sub> (s) against depth for a 59μm thick deposit. Calculation with 2ppm Li, 1200ppm B and 25cm <sup>3</sup> kg <sup>-1</sup> (STP) H <sub>2</sub> .....	5-22
Figure 5-29 Vogtle 2 Cycle 9 plot of pH and crud temperature against deposit depth for a 35μm thick deposit. Calculation with 2ppm Li, 1200ppm B and 25cm <sup>3</sup> kg <sup>-1</sup> (STP) H <sub>2</sub> .....	5-22
Figure 5-30 Vogtle 2 Cycle 9 plot of H <sub>2</sub> , H <sub>2</sub> O <sub>2</sub> and OH against depth for a 59μm thick deposit. Calculation with 2ppm Li, 1200ppm B and 25cm <sup>3</sup> kg <sup>-1</sup> (STP) H <sub>2</sub> .....	5-23

Figure 5-31 V C Summer Cycle 12 plot of pH, Li<sup>+</sup>, Boric acid concentration and amount of LiBO<sub>2</sub>(s) against depth for a 59μm thick deposit. Calculation with 2ppm Li, 1200ppm B and 25cm<sup>3</sup> kg<sup>-1</sup> (STP) H<sub>2</sub>.....5-23

Figure 5-32 V C Summer Cycle 12 plot of pH and crud temperature against deposit depth for a 35μm thick deposit. Calculation with 2ppm Li, 1200ppm B and 25cm<sup>3</sup> kg<sup>-1</sup> (STP) H<sub>2</sub>.....5-24

Figure 5-33 V C Summer Cycle 12 plot of H<sub>2</sub>, H<sub>2</sub>O<sub>2</sub> and OH against depth for a 59μm thick deposit. Calculation with 2ppm Li, 1200ppm B and 25cm<sup>3</sup> kg<sup>-1</sup> (STP) H<sub>2</sub>.....5-24

Figure 5-34 Diablo Canyon Unit 1 Cycle 11 plot of pH, Li<sup>+</sup>, Boric acid concentration and amount of LiBO<sub>2</sub>(s) against depth for a 59μm thick deposit. Calculation with 2ppm Li, 1200ppm B and 25cm<sup>3</sup> kg<sup>-1</sup> (STP) H<sub>2</sub>.....5-25

Figure 5-35 Diablo Canyon Unit 1 Cycle 11 plot of pH and crud temperature against deposit depth for a 35μm thick deposit. Calculation with 2ppm Li, 1200ppm B and 25cm<sup>3</sup> kg<sup>-1</sup> (STP) H<sub>2</sub> .....5-25

Figure 5-36 Diablo Canyon Unit 1 Cycle 11 plot of pH and crud temperature against deposit depth for a 35μm thick deposit. Calculation with 2ppm Li, 1200ppm B and 25cm<sup>3</sup> kg<sup>-1</sup> (STP) H<sub>2</sub> .....5-26

Figure B-1 Vogtle Unit 2 Cycle 9 Heat Flux ..... B-12

Figure B-2 V. C. Summer Cycle 12 Heat Flux ..... B-12

Figure B-3 Diablo Canyon Unit 1 Cycle 11 Heat Flux..... B-13



## LIST OF TABLES

---

Table 2-1 Temperatures and pH values for each plant component.....	2-1
Table 2-2 Plant parameters used for the CDM model. ....	2-2
Table 3-1 Plant data measured coolant on soluble and insoluble material.....	3-2
Table 4-1 Molar volumes of dissolved species. ....	4-13
Table 5-1 Standard input conditions for the CCM model.....	5-1
Table 5-2 Input conditions for plant calculations.....	5-21
Table 6-1 Sensitivity coefficients for plant operating parameters. ....	6-2
Table A-1 Thermodynamic coefficients for determining the enthalpy and entropy of formation. ....	A-2
Table A-2 Thermodynamic parameters for determining the enthalpy and entropy of water. ....	A-2
Table A-3 Model rate constants. ....	A-5
Table B-1 Data for Vogtle 2 Cycle 9 .....	B-6
Table B-2 Data for V. C. Summer Cycle 12.....	B-8
Table B-3 Data for Diablo Canyon Unit 1 Cycle 11.....	B-10
Table C-1 Comparison between the analytical and numerical solutions to the thermal hydraulic equations. ....	C-8
Table D-1 Error tolerances, run times and model sizes used for various deposit thicknesses .....	D-3
Table E-1 Q value for $^{10}\text{B}(n, \alpha)^7\text{Li}$ reaction .....	E-2
Table E-2 Particle ranges .....	E-2



# 1

## INTRODUCTION

---

The axial offset (AO) of a PWR plant is the integrated power output in the top half of the core minus the integrated power over the bottom of the core, all divided by the total power output. When a PWR is operational this parameter is measured and compared with predictions from a computer code. For most plants these comparisons are good but in recent years, for some plants operating at high power, this has not been the case. This AO anomaly (AOA) results from a shift in power output towards the bottom of the core as a result of a fall in the neutron flux in the upper core regions. This can have safety implications which could lead to a down rating of the plant and subsequent economic losses. At least 18 plants in the U.S. have suffered from AOA along with units in France, Korea and Belgium.

It has been reported that the cause of AOA is due to crud build-up on the fuel in the top half of the core as a result of increased sub-cooled nucleate boiling in this region. The take-up of boron in this deposit gives increased local boron concentrations that lead to the observed drop in the neutron flux. While it is now fairly clear that this is the mechanism for AOA, many details are not clear. Questions about the relative importance of plant operational parameters, such as boron, lithium and hydrogen concentration still remain, as are questions about the nature of the boron within the deposit and by how much it is concentrated. The temperature, pH and oxidizing conditions within the crud are also unclear and these may have consequences for fuel performance. In order to suggest the best mitigation strategy it is important to understand AOA further and have answers to all of these questions.

This report discusses both aspects of the phenomena; the crud deposition process and the chemistry that takes place within this crud once it is formed. A simple model for crud deposition has been created and the effect of plant operational parameters on the extent of crud build-up was studied using this model. A relatively sophisticated model describing the chemistry and physical conditions within the crud has also been developed and used to investigate crud chemistry. Both these models are described here, along with the results of calculations using the models. Chapter 2 describes the crud deposition model (CDM) and Chapter 3 presents the results of using this model. Chapter 4 describes the crud chemistry model (CCM) and Chapter 5 gives the results from using this model. Chapter 6 is a general discussion of the modeling results and Chapter 7 presents the conclusions. Finally, Chapter 8 reviews suggestions for future work to enhance the models.



# 2

## CRUD DEPOSITION MODEL (CDM)

This section describes a very simple model for simulating crud build-up on a fuel pin. This crud deposition model (CDM) is a simple “box” model in which each compartment (box) represents a particular component of the plant. Within each compartment the properties of the water and material in the water are assumed to be the same through out. In Figure 2-1 the particular components of the plant that are modeled are shown and consist of a cold leg, two core sections, two fuel sections and the hot leg. The two fuel sections correspond to boiling and non-boiling zones and the corresponding core sections are simply those parts of the core adjacent to these parts of the fuel. The temperatures in each of the boxes are shown in Figure 2-1 and are tabulated in Table 2-1 which also contains the calculated pH in each region at various boron and lithium concentrations. Table 2-2 shows the plant parameters that are used in the model, these parameters are based on Sizewell B information [1] and data for Kraftwerk Union (KWU) designed plants [2].

**Table 2-1**  
**Temperatures and pH values for each plant component**

Temperature/°C		280	300	320	345
[B]/ppm	[Li]/ppm	pH			
1200	2	6.80	6.90	7.2	7.54
1200	1	6.52	6.69	6.90	7.24
1200	0.1	5.64	5.79	5.97	6.29
600	2	7.11	7.26	7.47	7.80
600	1	6.81	6.97	7.17	7.50
600	0.5	6.52	6.67	6.87	7.20
300	1	7.05	7.19	7.39	7.71

Crud Deposition Model (CDM)

**Table 2-2**  
Plant parameters used for the CDM model.

Parameter	Value
Crud Density ( $\text{kg m}^{-3}$ )	1000
Volume Flow Rate ( $\text{m}^3 \text{s}^{-1}$ )	25.9
Length of Core (m)	3.7
Fuel Surface Area ( $\text{m}^2$ )	9905
Flow Velocity ( $\text{m s}^{-1}$ )	1.8
Effective Core Diameter (m)	2.15
Core Volume ( $\text{m}^3$ )	13.2
Percentage of Fuel Area Boiling	5%

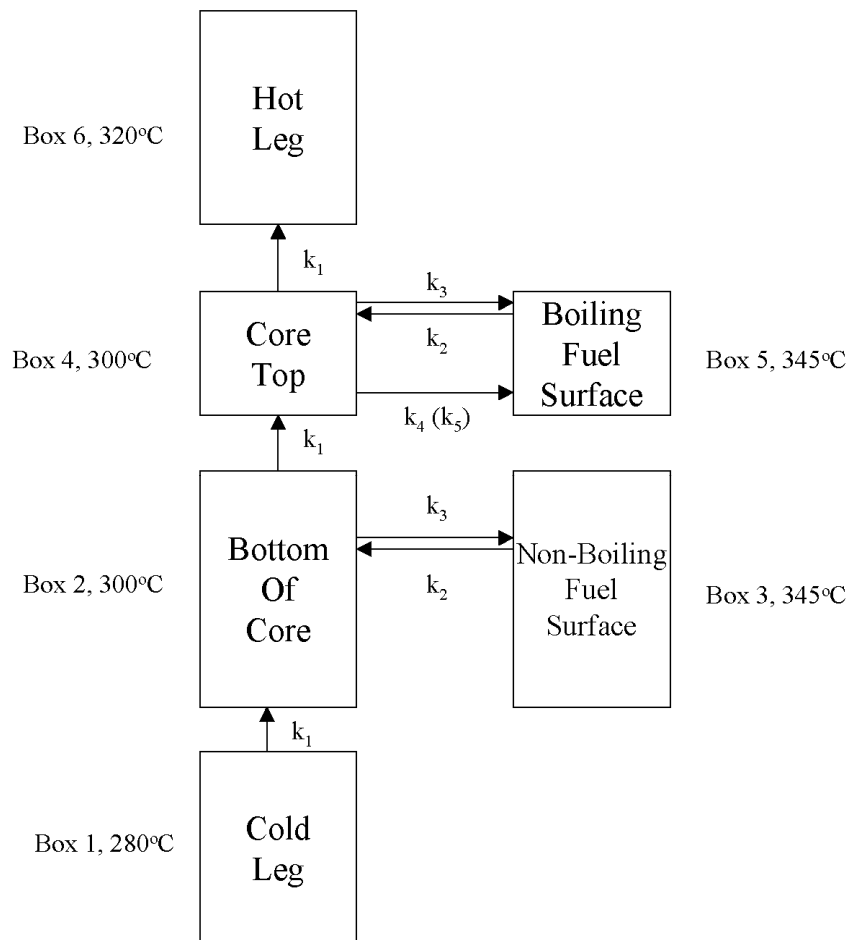


**Figure 2-1**  
Schematic diagram of modelled loop components along with soluble species transport constants

## 2.1 Soluble Species Equations

For the cold leg (box 1) soluble species are generated from the chemistry (dissolution of  $\text{NiFe}_2\text{O}_4$ ) and lost to the first part of the core region (box 2). In the bottom part of the core species either transport (turbulent mass transport) to the surface of the fuel (box 3) or flow to the top of the core (box 4). It is assumed that soluble species transported to the fuel surface precipitate out and deposit on the fuel. There is no mechanism in the model for re-suspension and so the model will give an upper limit on the thickness of the crud deposit. Soluble species transported to the top of the core can either deposit on the fuel (box 5) by simple mass transport and as a result of boiling, or can leave the core and enter the hot leg (box 6). It is assumed that some standing concentration of soluble species exists in the boundary layer adjacent to the fuel, and the concentration difference between this and the bulk generates the net mass flux of material to the surfaces. For soluble species the following equations representing this behavior are solved to obtain the species concentrations in each box (the subscript for each soluble species has been left out to simplify the notation).

$$\frac{dc_1^l}{dt} = \left( \frac{dc_1^l}{dt} \right)_R - k_1 c_1^l \quad (1)$$

$$\frac{dc_2^l}{dt} = \left( \frac{dc_2^l}{dt} \right)_R + k_1 (c_1^l - c_2^l) - k_2 (c_2^l - c_3^l) \quad (2)$$

$$\frac{dc_3^l}{dt} = \left( \frac{dc_3^l}{dt} \right)_R + k_3 (c_2^l - c_3^l) \quad (3)$$

$$\frac{dc_4^l}{dt} = \left( \frac{dc_4^l}{dt} \right)_R + k_1 (c_2^l - c_4^l) - k_2 (c_4^l - c_5^l) - k_4 c_4^l \quad (4)$$

$$\frac{dc_5^l}{dt} = \left( \frac{dc_5^l}{dt} \right)_R + k_3 (c_4^l - c_5^l) + k_5 c_4^l \quad (5)$$

$$\frac{dc_6^l}{dt} = \left( \frac{dc_6^l}{dt} \right)_R + k_1 c_4^l \quad (6)$$

Here  $c^l$  is a soluble species concentration (there are 13 such species and therefore 13 sets of such equations) and the subscript denotes which box the species is in. The  $k_1$  term represents bulk transport between the boxes,  $k_2$  and  $k_3$  are associated with turbulent mass transport to the fuel surface, and  $k_4$ ,  $k_5$  simulate transport of material due to boiling. The appropriate decay constants are discussed further in Appendix A. The term  $\left( \frac{dc}{dt} \right)_R$  represents the net rate of production or loss of the species due to chemical reaction within the box and is also discussed below.

*Crud Deposition Model (CDM)***2.2 Insoluble Species Equations**

The water in the vessel will contain a small amount of suspended solid material. This colloidal material can be transported to the fuel surface by the same mechanisms as soluble material, where it may deposit. It is assumed that no particulate material exists in the boundary layer adjacent to the fuel and therefore no loss of particulate to the bulk from this layer is modeled. In order to describe this process the following equations are solved.

$$\frac{dc_1^p}{dt} = 0 \quad (7)$$

$$\frac{dc_2^p}{dt} = k_1(c_1^p - c_2^p) - k_6c_2^p \quad (8)$$

$$\frac{dc_3^p}{dt} = k_7c_2^p \quad (9)$$

$$\frac{dc_4^p}{dt} = k_1(c_3^p - c_4^p) - k_6c_4^p - k_4c_4^p \quad (10)$$

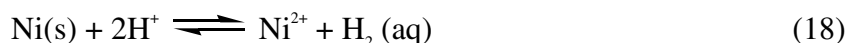
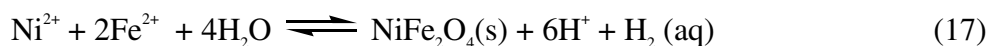
$$\frac{dc_5^p}{dt} = k_7c_4^p + k_5c_4^p \quad (11)$$

$$\frac{dc_6^p}{dt} = k_1(c_4^p - c_6^p) \quad (12)$$

Where  $c^p$  is the number density of particulate material which is assumed to have a radius of 10nm and density of  $2000\text{kg m}^{-3}$ . The first of these equations keeps the concentration of particles constant in the first box so there is a constant source, while the remaining equations transport particles between the boxes due to flow, turbulent mass transport and boiling.

## 2.3 Chemistry used in CDM

In each box the following chemistry is considered



For each of these chemical equations a corresponding chemical rate equation is formulated, for example for reaction (14) above and for the species  $\text{Fe}^{2+}$  this would be

$$\frac{d[\text{Fe}^{2+}]}{dt} = -k_f[\text{Fe}^{2+}] + k_r[\text{FeOH}^+][\text{H}^+] \quad (23)$$

where [ ] denotes species concentrations and  $k_f$  and  $k_r$  are the forward and reverse rate constants for the reactions. In the model  $k_r$  is chosen such that

$$\frac{k_f}{k_r} = K = \frac{[\text{FeOH}^+][\text{H}^+]}{[\text{Fe}^{2+}]} \quad (24)$$

where  $K$  is the equilibrium constant for the reaction and the forward rate is made large so steady state is achieved rapidly. Calculations are performed with the solid Nickel Ferrite,  $\text{NiFe}_2\text{O}_3$  present in all boxes and so in general species concentrations in each box are simply determined from the thermodynamics in that compartment. The thermodynamics for this system along with how the various rate constants are calculated is discussed in Appendix A.

All the above equations have been implemented into a FACSIMILE model [3] and this was then used to carry out calculations for typical plant conditions. The results of these calculations are discussed in the following section.



# 3

## CRUD DEPOSITION MODEL (CDM) RESULTS

---

Table 3-1 shows some measured data for soluble and insoluble material measured at various PWR plants [4]. Although there is much debate about the accuracy of the measurement techniques, what Table 3-1 implies is that the amount of soluble material is larger than insoluble. The average amount of soluble material from Table 3-1 is 2029ng/kg, while the average insoluble amount is 264ng/kg. It is likely therefore that the main depositing material forming the crud will be soluble and so for the initial calculations outlined below insoluble material is not included. The crud thicknesses that are plotted below are for a 12 month cycle, unless otherwise stated.

Figure 3-1 is a plot of the calculated crud thickness against applied heat flux for the top part of the fuel. The conditions for these calculations are typical plant conditions of 1200ppm B, 2ppm Li and 25 cc kg<sup>-1</sup>(STP) H<sub>2</sub>. When no heat flux is applied the crud thickness is approximately 2.5µm and is the same at the bottom and top of the fuel. For a heat flux of 10<sup>5</sup> Wm<sup>-2</sup> the crud thickness at the top of the fuel is 14 µm which rises to 112 µm for a heat flux of 10<sup>6</sup> Wm<sup>-2</sup>. Calculations of the heat flux for AOA plants indicates typical values between 6x10<sup>5</sup> and 9x10<sup>5</sup> Wm<sup>-2</sup> (see Appendix B), with none AOA plants being lower. The model predicts the thickness is a linear function of the heat flux. Although the model is constructed to over-predict the likely amount of crud being deposited, the crud thickness that is predicted is similar to plant observations. Plants in which the fuel is not boiling typically have a crud thickness of a few microns or less, while plants undergoing boiling have observed crud as thick as 100 µm.

Figure 3-2 is a plot of the calculated crud thickness at the top of the fuel for different H<sub>2</sub> concentrations. The other conditions are [B] = 1200ppm, [Li] = 1 and 2ppm, and heat flux 5x10<sup>5</sup> Wm<sup>-2</sup>. It is clear from the plot that the crud thickness falls with decreasing H<sub>2</sub> concentration. The reason for this can be seen from equations 13 and 17 which show that the two main solids in the system, NiFe<sub>2</sub>O<sub>4</sub> and Fe<sub>3</sub>O<sub>4</sub> undergo reductive dissolution, so lowering the H<sub>2</sub>(aq) lowers the amount of soluble material that can deposit on the fuel.

Figure 3-3 shows how the crud thickness at the top of the fuel varies with increasing Li concentration. The other conditions for these calculations are [B] = 1200ppm, H<sub>2</sub> = 5, 25 cc kg<sup>-1</sup>, and a heat flux of 10<sup>6</sup> W m<sup>-2</sup>. At very low lithium values of 0.1ppm the predicted crud thickness is very large 500 to 800 µm, but this falls to more reasonable values of 90 to 150 µm for more typical lithium concentrations of 1 and 2 ppm. For the calculations at 25 cc kg<sup>-1</sup> H<sub>2</sub> increasing the lithium concentration above 1ppm causes the crud thickness to fall further, but the effect is small, with the predicted thickness falling from 146µm to 114µm after doubling the Li concentration to 2ppm.

*Crud Deposition Model (CDM) Results*

**Table 3-1  
Plant data measured coolant on soluble and insoluble material**

Plant	pH	Soluble Fe (ng kg <sup>-1</sup> )	Insoluble Fe (ng kg <sup>-1</sup> )	Soluble Ni (ng kg <sup>-1</sup> )	Insoluble Ni (ng kg <sup>-1</sup> )
Doel1	7			680	750
Doel2	6.9	1040		390	
Doel4	7.4		10	78	33
Doel4	7.3			560	
Vandellos II	7.2	2150		114	101
Penly 1	7	2320	101	138	56
Ringhals 2	7.21	1710	1010	67	19
Sizewell B	7.25	5961	139	134	48
Sizewell B	7.34	4496		111	
Sizewell B	7.19	6123	322	255	129
Sizewell B	7.39	3313		95	
Sizewell B	7.26	4288	93	416	71
Sizewell B	7.39	202		108	
Sizewell B	6.98	7438	106	1161	64
Neckarwestheim 1	7.3	498		80	
Neckarwestheim 1	7.08	1617		49.6	
Grohnde	7.4	265		38.8	
Trillo	7.42	1465	52	20	22
Phillippsburg	7.3	3207		36.6	31
Brokdorf	7	1460		38.3	
Neckarwestheim 2	7.3	972		14.1	26
Neckarwestheim 2	7.13	2400	950	83	99
Loviisa 1	7.12	2823	226	65	13
Loviisa 1	7.27	365	345	13	29
Loviisa 2	7.15	129	110	57	8.3
Loviisa 2	7.12	195	53	139	6.3
Dukovany 3	7.15	2217	45	85	8
Paks 1	7.28	22	607	34	8.2
Paks 1	7.28	82		16.5	0.05
Paks 2	7.47	26	62	10.9	2.7
Paks 2	7.18	46		9.6	0.05
Average		2029.643	264.4375	164.4323	69.3

Crud Deposition Model (CDM) Results

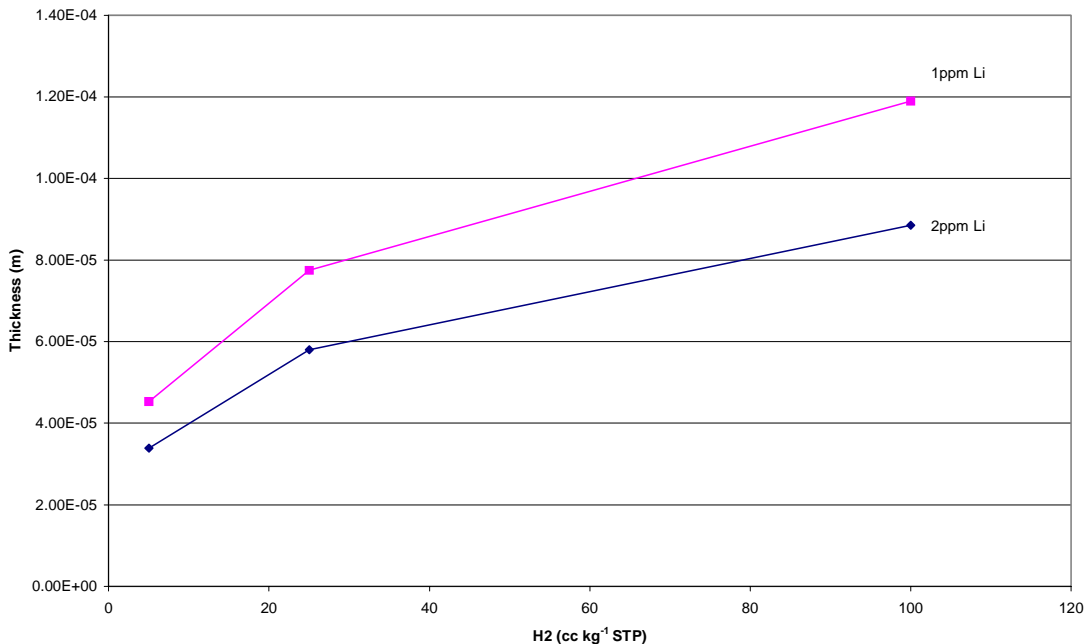


**Figure 3-1**  
 Plot of crud thickness on the boiling fuel surface against applied heat flux. Calculation for 1200ppm B, 2ppm Li and 25 cc kg<sup>-1</sup>(STP) H<sub>2</sub>.

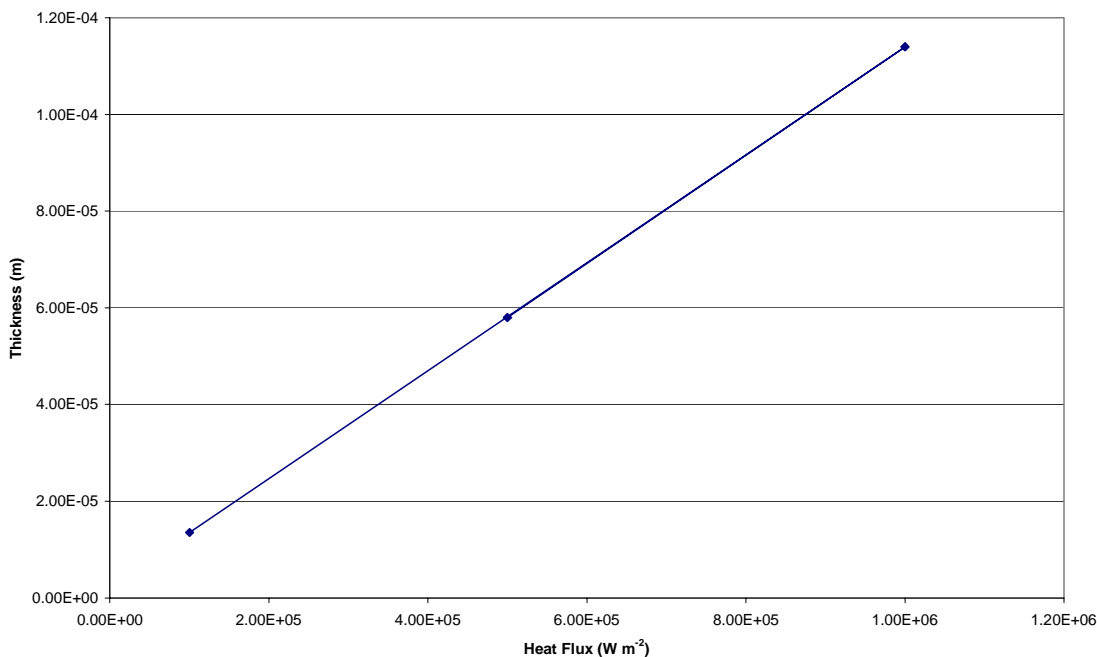


**Figure 3-2**  
 Plot of crud thickness on the boiling fuel surface against bulk hydrogen concentration. Calculation for 1200ppm B and a heat flux of 5x10<sup>5</sup> Wm<sup>-2</sup>.

Crud Deposition Model (CDM) Results

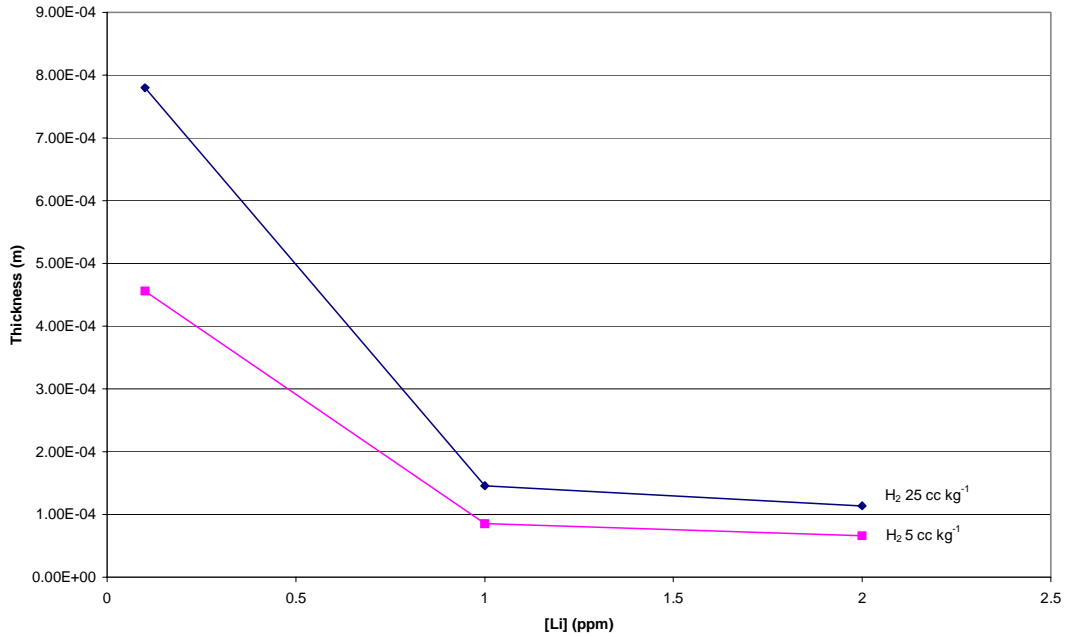


**Figure 3-3**  
**Plot of crud thickness on the boiling fuel surface against bulk lithium concentration.**  
**Calculation for 1200ppm B and a heat flux of  $1 \times 10^6 \text{ W m}^{-2}$ .**

Figure 3-4 shows the effect of changing the boron concentration on the crud thickness. The calculations were carried out for the conditions, [Li] = 1ppm, H<sub>2</sub> = 5, 25 cc kg<sup>-1</sup> and a heat flux of  $10^6 \text{ W m}^{-2}$ . The crud thickness falls with decreasing boron concentration from 146μm at 1200ppm boron to 89μm at 300 ppm B.

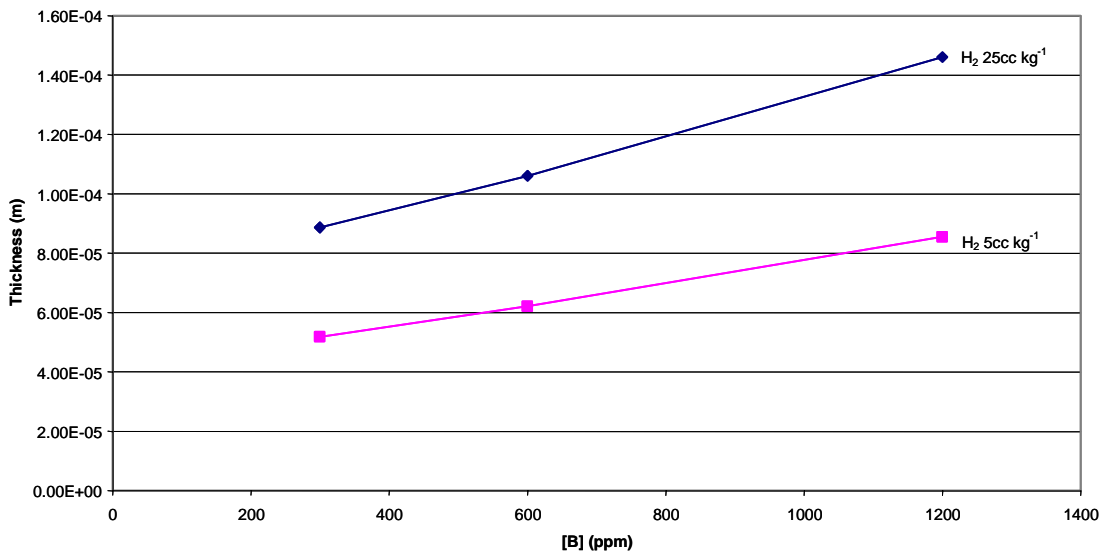


**Figure 3-4**  
**Plot of crud thickness on the boiling fuel surface against bulk boron concentration.**  
**Calculation for [Li] of 1ppm and a heat flux of  $1 \times 10^6 \text{ W m}^{-2}$ .**

Crud Deposition Model (CDM) Results

Calculations were performed with added particulate material present. These calculations were carried out at the typical plant operational conditions of 1200ppm B, 2ppm Li, 25cc kg<sup>-1</sup> H<sub>2</sub> and for a heat flux of 5x10<sup>5</sup> W m<sup>-2</sup>. Three calculations were done using particle number densities of 10<sup>14</sup>, 10<sup>15</sup> and 10<sup>16</sup> particles m<sup>-3</sup>, which correspond to insoluble masses of 1.1ppb, 11ppb and 110ppb. The mass of soluble material in the liquid is 3ppb, so the first calculation for 1.1ppb solid corresponds to a situation where the soluble material is larger than the insoluble (typical plant condition), while in the two other calculations the amount of insoluble is greater than the soluble material. Figure 3-5 shows how the crud thickness on the bottom and top of the fuel vary as a function of solid content in the water. The addition of 1ppb of insoluble material to the water causes the crud thickness at the bottom of the fuel to increase from 2.6 to 3.3µm while the thickness at the top of the fuel increases from 58µm to 74µm. The percentage increase is approximately the same in both cases (27%) despite the fact that the amount of particulate material in solution is lower in the top half of the core compared to the bottom (having deposited on the bottom half) by about 20 to 30%. The greater mass transport rates due to boiling in the top half of the core compensate for the fall in the concentration of insoluble material.

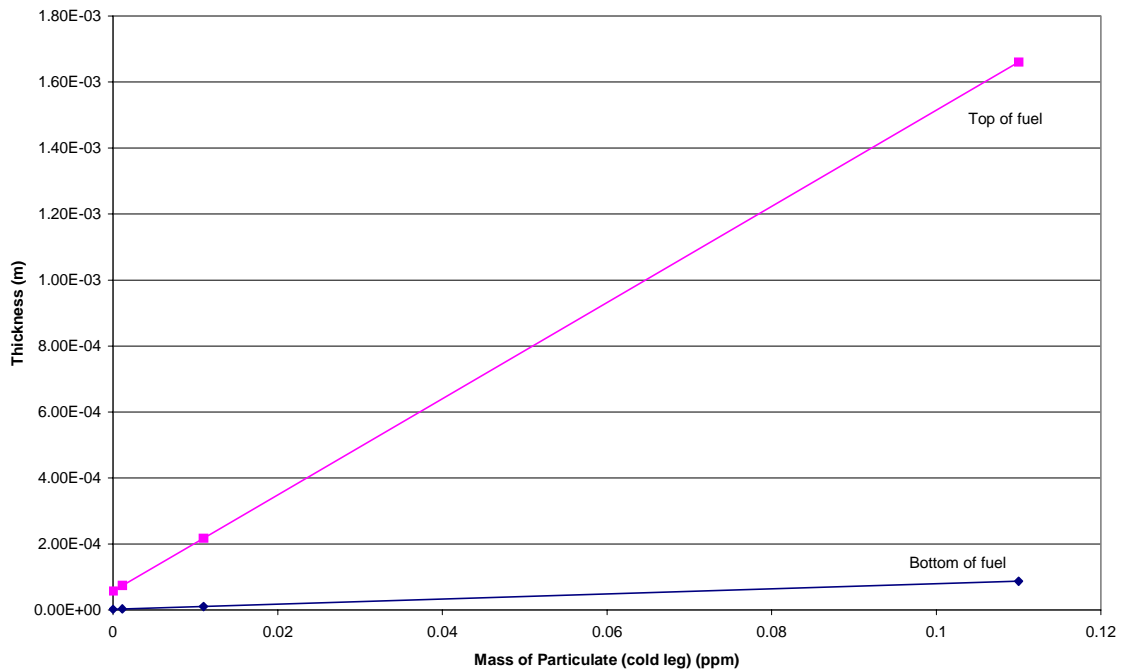


**Figure 3-5**  
**Plot of crud thickness on the boiling and non-boiling fuel surface against bulk particulate concentration. Calculation for [B] = 1200ppm, [Li] 2ppm, H<sub>2</sub> 25cc kg<sup>-1</sup>(STP) and a heat flux of 1x10<sup>6</sup> Wm<sup>-2</sup>.**



# 4

## CRUD CHEMISTRY MODEL (CCM)

---

This Chapter describes a chemistry model of fuel crud deposits in a PWR reactor, the model treats the heat transfer, fluid flow and chemical reactions taking place in porous deposits on the fuel pins of the reactor. The model builds on a previous version [5] by implementing a more realistic thermal hydraulics model together with a more rigorous treatment of the thermodynamics of the high temperature aqueous solution. The new model includes the following features

- a Wick boiling model;
- radiolysis chemistry of water, taking into account the alpha dose from the  $^{10}\text{B}(n, \alpha)^7\text{Li}$  reaction;
- magnetite dissolution and iron hydrolysis reactions;
- Ni-Fe Ferrite dissolution and nickel hydrolysis reactions;
- Ni metal and Ni oxide formation;
- boric acid chemistry and the precipitation of lithium borate;
- non-ideal solution thermodynamics;
- the effect of solute concentration on the saturation temperature and vaporization enthalpy of water.

Section 4.1 describes the physical basis of the model while Section 4.2 summarizes the chemistry included in it. The numerical solution of the model equations is described in Appendix C. Section 4.3 discusses various thermodynamic problems that must be taken into account and Section 4.4 summarizes the equations used to calculate the physical properties of high temperature water.

The model, as in the case of the crud deposition model, has been implemented in FACSIMILE. The FACSIMILE program of the model is briefly described in Appendix D.

Crud Chemistry Model (CCM)

**4.1 Physical basis of CCM**

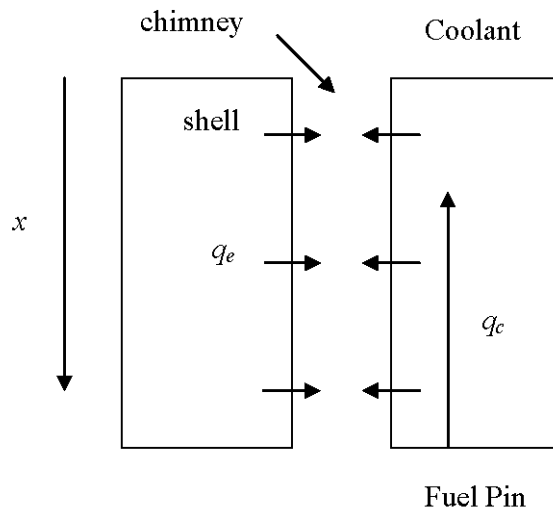
The model treats the heat flux, fluid flow and chemical reactions in a deposit unit cell, consisting of one steam chimney and its surrounding porous shell. The model is one dimensional through the depth of the deposit from the bulk solution to the surface of the metal and consists of the following components.

- A thermal hydraulics model of heat transfer within and fluid flow of water and steam through the porous deposit.
- Transport of chemical species in solution through the porous shell.
- Partitioning of volatile species into the steam phase.
- Chemical reactions in and precipitation of solids from solution.

These components are described in more detail below.

**4.1.1 Thermal hydraulics**

The thermal hydraulics model is based on Cohen’s one dimensional Wick boiling model [6]. This is derived by considering the heat transfer in a deposit unit cell, consisting of one steam chimney and its surrounding porous shell. Heat transfer is assumed to take place by conduction across the porous shell from the fuel pin towards the bulk coolant and by evaporation of steam at the surface of the chimney, as shown schematically in the diagram below.



The steady state heat balance between these two processes is represented by

$$\int_{shell} q_c dA + \int_{chimney} q_e dA = 0 \tag{25}$$

where  $q_c$  is the conductive heat flux in the porous shell, taken to be in a direction parallel to the chimney and  $q_e$  is the evaporative heat flux on the surface of the chimney. Transforming the first integral over the shell surface into an integral over the shell volume using the divergence theorem gives

$$\int_{shell} \frac{dq_c}{dx} dV + \int_{chimney} q_e dA = 0 \quad (26)$$

where the  $x$  coordinate measures the distance through the deposit from the bulk coolant. Substituting  $dV = f dx / N_c$  and  $dA = 2\pi r_c dx$ , where  $f$  is the fractional area of the porous shell,  $N_c$  is the area density of chimneys and  $r_c$  is the chimney radius, gives

$$\frac{dq_c}{dx} + \frac{2\pi r_c N_c}{f} q_e = 0 \quad (27)$$

The final equation for the temperature distribution,  $T(x)$ , in the deposit is obtained by substituting  $q_c = -k_c dT/dx$  and  $q_e = h_e(T - T_s)$  to give

$$\frac{d^2 T}{dx^2} - \frac{2\pi r_c N_c h_e}{f k_c} (T - T_s) = 0 \quad (28)$$

where  $k_c$  is the thermal conductivity of the porous shell,  $h_e$  is the evaporative heat transfer coefficient and  $T_s$  is the saturation temperature. This equation is solved subject to the boundary conditions,

$$T = T_b \quad \text{at } x = 0 \quad (29a)$$

$$k_c \left( \frac{\partial T}{\partial x} \right)_{x=d} = \frac{q_0}{f} \quad \text{at } x = d \quad (29b)$$

where  $T_b$  is the bulk coolant temperature,  $q_0$  is the heat flux at the surface of the fuel pin and  $d$  is the thickness of the deposit.

Liquid flows through the porous shell from the bulk coolant while steam is expelled through the chimney. Steady state mass conservation of water in the solution in the porous shell is represented by

$$\int_{shell} \rho_w u_l dA + \int_{chimney} j_e dA = 0 \quad (30)$$

where  $\rho_w$  is the density of water,  $u_l$  is the liquid velocity in the  $x$  direction and  $j_e$  is the evaporative mass flux at the surface of the chimney. Transforming the integrals in this equation in the same way that was done for the integrals in equation (25) leads to the following differential equation for the velocity

*Crud Chemistry Model (CCM)*

$$\frac{d(\rho_w u_l)}{dx} + \frac{2\pi r_c N_c}{f} j_e = 0 \quad (31)$$

The evaporative mass flux is given by  $j_e = h_e(T - T_s)/H_v$ , where  $H_v$  is the vaporization enthalpy of water. Substituting this into (31) gives

$$\frac{d(\rho_w u_l)}{dx} + \frac{2\pi r_c N_c}{f} \frac{h_e}{H_v} (T - T_s) = 0 \quad (32)$$

This equation is solved subject to the boundary condition that  $u_l = 0$  at  $x = d$ .

Steady state mass conservation of steam in the chimney is represented by

$$\int_{\text{chimney}} \rho_s u_v dA - \int_{\text{chimney}} j_e dA = 0 \quad (33)$$

where  $\rho_s$  is the density of steam and  $u_v$  is the velocity of the vapor in the chimney. Transforming the integrals in the same way that was done for those in equation (25) leads to the following differential equation for the steam velocity

$$\frac{d(\rho_s u_v)}{dx} - \frac{2}{r_c} j_e = 0 \quad (34)$$

Eliminating  $j_e$  using equation (31) gives

$$\frac{d(\rho_s u_v)}{dx} + \frac{f}{\pi r_c^2 N_c} \frac{d(\rho_w u_l)}{dx} = 0 \quad (35)$$

This equation may be integrated to give the following relation between the vapor and liquid velocities

$$u_v = -\frac{f}{\pi r_c^2 N_c} \frac{\rho_w}{\rho_s} u_l \quad (36)$$

Although it is straightforward to derive an equation and solve it for the steam temperature, this has not been done in this work. Instead, the steam temperature is simply set equal to the temperature of the porous shell. In the virtual absence of heat transfer between the steam in the chimney and the porous shell, this is a poor approximation. However, its consequences are not thought to be very important for the treatment of liquid to vapor partitioning and evaporative heat transfer. This could be investigated by removing the approximation in a future development of the model.

### 4.1.2 Transport in The Porous Shell

The coolant of a PWR contains dissolved boric acid, lithium hydroxide and hydrogen plus trace amounts of other species arising from the radiolysis of water and the corrosion of metal. These species become concentrated within the porous shell where they react amongst themselves and with the oxides of the deposit. Dissolved species are transported through the porous shell by flow, by diffusion in their concentration gradient and, if they are charged, by drift in the electric potential gradient. For each species, the superficial molecular flux  $J_i$  is given by

$$J_i = -D_i \frac{\partial C_i}{\partial x} - \frac{zFD_i}{RT} \phi' + u_i C_i \quad (37)$$

where  $C_i$  is the concentration in the liquid,  $D_i$  is the diffusion coefficient,  $z$  is the charge number,  $F$  is the Faraday unit of charge, and  $\phi'$  is the potential gradient. To simplify the notation, subscripts will not be appended to  $J_i$ ,  $C_i$ ,  $D_i$  and  $z$  to differentiate the species. The diffusion coefficient  $D_i$  in the porous shell is related to the diffusion coefficient in liquid water  $D_w$  by the following empirical equation

$$D_i = \frac{\varepsilon D_w}{\tau} \quad (38)$$

where  $\tau$  is the tortuosity factor and  $\varepsilon$  is the porosity of the shell. Within the shell, each species obeys a conservation equation for its concentration in the liquid  $C_i$ , given by

$$\frac{\partial}{\partial t} \int_{shell} C_i dV = \int_{shell} \left( \frac{\partial C_i}{\partial t} \right)_R dV - \frac{1}{\varepsilon} \int_{shell} J dA \quad (39)$$

The first term on the right-hand side of this equation is the rate of change of  $C_i$  due to chemical reaction, which in the model is expressed via rate equations for the chemical reactions involving the species. Equation (39) leads directly to the following partial differential equation for  $C_i$

$$\frac{\partial C_i}{\partial t} = \left( \frac{\partial C_i}{\partial t} \right)_R - \frac{1}{\varepsilon} \frac{\partial J}{\partial x} \quad (40)$$

This equation is solved subject to the boundary condition that  $C_i = C_b$  at  $x = 0$ , where  $C_b$  is the concentration in the bulk coolant.

The potential gradient is obtained from a generalised Ohm's law equation, derived by multiplying equation (37) by  $z$  and summing over all charged species to give

$$\sigma \phi' = -j_D, \quad (41)$$

where  $j_D$  is the diffusion current density and  $\sigma$  is the conductivity. They are given by the following equations, in which the summations are over all charged species,

Crud Chemistry Model (CCM)

$$j_D = F \sum z D_l \frac{\partial C_l}{\partial x}, \quad (42)$$

$$\sigma = \frac{F^2}{RT} \sum z^2 D_l C_l. \quad (43)$$

The derivation of equation (41) uses the fact that since there is no conduction current flowing in the shell,  $F \sum zJ = 0$ .

### 4.1.3 Partitioning and transport of volatile species

The model treats the partitioning of three volatile species, boric acid, hydrogen and radiolytically produced oxygen, from the liquid phase in the porous shell into the vapor phase in the chimney. Partitioning of a volatile species from the liquid to the vapor phase is described by adding a term to equation (39) so that the conservation of its concentration  $C_l$  in the liquid phase is now given by

$$\frac{\partial}{\partial t} \int_{shell} C_l dV = \int_{shell} \left( \frac{\partial C_l}{\partial t} \right)_R dV - \frac{1}{\varepsilon_{shell}} \int J_l dA - \frac{1}{\varepsilon_{shell}} \int J_m dA \quad (44)$$

where  $J_m$  is the mass flux from the liquid to the vapor phase. This leads to the following partial differential equation for the concentration

$$\frac{\partial C_l}{\partial t} = \left( \frac{\partial C_l}{\partial t} \right)_R - \frac{1}{\varepsilon} \frac{\partial J_l}{\partial x} - \frac{2\pi r_c N_c}{\varepsilon f} J_m \quad (45)$$

The mass flux  $J_m$  is determined by a rate equation for the partitioning of a volatile species from the liquid into the vapor phase,

$$J_m = k_m (C_v^e - C_v) \quad (46)$$

where  $k_m$  is the mass transfer coefficient in units of velocity,  $C_v$  is the concentration of the volatile species in the vapor phase and  $C_v^e$  is its equilibrium concentration. The latter quantity is determined by the partition equilibrium, represented by

$$K_{lv} = \frac{C_v^e}{C_l} \quad (47)$$

where  $K_{lv}$  is the equilibrium constant. Combining (46) and (47) gives the following equation for the mass flux

$$J_m = k_m (K_{lv} C_l - C_v) \quad (48)$$

It is convenient to rewrite equation (45) in the form

$$\frac{\partial C_l}{\partial t} = \left( \frac{\partial C_l}{\partial t} \right)_R + \left( \frac{\partial C_l}{\partial t} \right)_P - \frac{1}{\varepsilon} \frac{\partial J_l}{\partial x} \quad (49)$$

where the second term on the right hand side of the equation represents the rate of change of  $C_l$  due to partitioning from the liquid into the vapor phase and is given by

$$\left( \frac{\partial C_l}{\partial t} \right)_P = -\frac{2\pi r_c N_c}{\varepsilon f} k_m (C_v^e - C_v) \quad (50)$$

Equation (49) is written in a form which shows that homogeneous reactions in the liquid phase and partitioning into the vapor phase both affect the rate of change of  $C_l$  via rate equations.

Volatile species are transported in the vapor phase in the chimney by diffusion and flow. For each species, the molecular flux  $J_v$  is given by

$$J_v = -D_v \frac{\partial C_v}{\partial x} + u_v C_v \quad (51)$$

where  $C_v$  is the concentration in the vapor,  $D_v$  is the diffusion coefficient and  $u_v$  is the previously defined vapor velocity. Within the chimney, each species obeys a conservation equation for its concentration, given by

$$\frac{\partial}{\partial t} \int_{chimney} C_v dV = \int_{chimney} \left( \frac{\partial C_v}{\partial t} \right)_P dV - \int_{chimney} J_v dA \quad (52)$$

where the first term on the right hand side represents the rate of change of  $C_v$  due to partitioning from the liquid phase, given by

$$\left( \frac{\partial C_v}{\partial t} \right)_P = \frac{2k_m}{r_c} (C_v^e - C_v) \quad (53)$$

Using similar methods to those employed previously, equation (52) is transformed into the following differential equation for the concentration,

$$\frac{\partial C_v}{\partial t} = \left( \frac{\partial C_v}{\partial t} \right)_P - \frac{\partial J_v}{\partial x} \quad (54)$$

This expression could also have been written down by analogy with equation (49), describing the rate of change of species concentration in the porous shell. Equation (54) is solved assuming that the vapor concentration is zero in the bulk coolant, that is  $C_v = 0$  at  $x = 0$ .

*Crud Chemistry Model (CCM)*

**4.1.4 Analytical solution**

There is a simple analytical solution of the thermal hydraulic equations under the condition that the properties of water, density, thermal conductivity, evaporative heat transfer coefficient, and saturation temperature, are independent of temperature. In practice, this condition is never realized particularly in the thick deposits of interest to AOA. The analytical solution was first given by Cohen [6] and has been used historically to predict the concentration of boron in fuel crud deposits. It was only used in this work to test the numerical algorithm for the thermal hydraulic equations.

The solution to equation (28) for the temperature profile through the deposit together with its boundary conditions in equation (29) is given by

$$T = T_s + \frac{q_0}{fk_c a} \frac{\sinh(ax)}{\cosh(ad)} \quad (55)$$

where the constant  $a$  is given by

$$a^2 = \frac{2\pi r_c N_c h_e}{fk_c} \quad (56)$$

The solution to equation (32) for the liquid velocity in the porous shell is then given by

$$u_l = \frac{q_0}{\rho_w H_v f} \left( 1 - \frac{\cosh(ax)}{\cosh(ad)} \right) \quad (57)$$

The steady state concentration for the transport of a non-reactive neutral species is obtained from equations (37) and (40) as

$$D_l \frac{d^2 C_l}{dx^2} - \frac{d(u_l C_l)}{dx} = 0 \quad (58)$$

Its solution, obtained using equation (57), is given by

$$C_l = C_b \exp \left( \frac{q_0}{f \rho_w H_v D_l} \left[ x - \frac{\sinh(ax)}{a \cosh(ad)} \right] \right) \quad (59)$$

In practice, this equation greatly overestimates the increase in concentration at the bottom of thick deposit. This is because this approach does not account for the decrease in vaporization enthalpy with the temperature. A result of this decrease is that evaporation ceases towards the bottom of a relatively thick deposit, halting the concentrating effect of the boiling in this region. This behavior is discussed in more detail later in the report.

## 4.2 Chemistry used in CCM

Chemical reactions are included in CCM in the same way as in CDM, that is reactions are included in the form of rate equations, which express the rate of change of species concentrations as equal to the product of a rate constant and the concentrations of the reactant concentrations. For example, for the reaction



the rate of change of the concentration of A would be given by

$$\frac{d[A]}{dt} = -k_f[A][B] \quad (61)$$

where the terms in square brackets are concentrations and  $k_f$  is the rate constant for the reaction. The right hand side of this equation also describes the rate of change of [B] and, with a change of sign, the rate of change of [C] and [D]. Many of the reactions included in the model are treated as equilibria with rate equations used to express both the forward and reverse reactions. If that were the case in the example of reaction (60), the equation describing the rate of change of [A] would be modified to give

$$\frac{d[A]}{dt} = -k_f[A][B] + k_r[C][D] \quad (62)$$

where  $k_r$  is the rate constant for the reverse reaction. The equilibrium constant for the reaction is equal to the ratio of the rate constants for the forward and reverse reactions and this has been used to determine an unknown from a known rate constant. Where neither rate constant is known, a suitably fast one is chosen for the reverse reaction to ensure that the overall reaction remains in equilibrium. The complications that arise from the different concentration units used for rate constants and equilibrium constants and the non-ideal parameters that enter equilibrium expressions will be discussed in Section 4.3.

The different types of chemical reactions included in the model are summarized below together with some examples of each and the sources for the rate and equilibrium data.

### (1) The ionization of water



The equilibrium constant for this reaction is calculated using the correlation of Marshall and Franck [7], taken from the chapter by Lindsay in the ASME Handbook on Water technology [8].

### (2) Metal ion hydrolysis reactions

These are identical to those used in CDM discussed in Section 2.3.

Crud Chemistry Model (CCM)

(3) Boric acid equilibria



Equilibrium constants for these reactions are taken from the MULTEQ [9] manual, based on an experimental study of Weres [10].

(4) Precipitation and dissolution reactions

For the metal ions the precipitation chemistry is identical to that used in CDM the only additional precipitation process is



The equilibrium constants for this reaction are taken from the experimental study of Byers, Lindsay and Kunig [11] for the dissolution of lithium borate. Precipitation reactions are included in the model in a special way as shown by the following example. The rate of the simple precipitation reaction from species  $A$  in solution to solid  $A_s$  is taken to be

$$\frac{d[A]}{dt} = f([A_s]) - \frac{[A]}{K_{sl}} \quad (69)$$

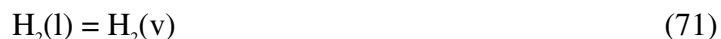
where  $K_{sl}$  is the equilibrium constant for the dissolution reaction and the function  $f$  is given by the following expression

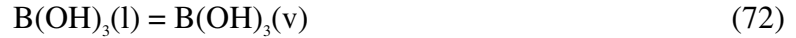
$$f = \exp\left(\frac{-1 \times 10^{10}}{[A_s] + 1 \times 10^{-13}}\right) \quad (70)$$

This function increases from essentially zero up to unity for values of  $[A_s]$  between  $10^{-11}$  and  $10^{-8}$  mol dm<sup>-3</sup>. The steady state solution of rate equation (69) is  $[A] = K_{sl}f$ , and the dependence of  $f$  on  $[A_s]$  shows that the steady state concentration of  $[A]$  will increase up to its saturation value of  $K_{sl}$  for values of  $[A_s]$  greater than  $10^{-8}$  mol dm<sup>-3</sup>. Moreover, only very small concentrations of precipitate will be present for concentrations of  $A$  below saturation. This method effectively smoothes out the precipitation reaction and enables it to be represented by a differential equation.

(5) Liquid to vapor partitioning reactions

Reactions for the partitioning of H<sub>2</sub>, O<sub>2</sub> and B(OH)<sub>3</sub> are included in the model, for example





Distribution coefficients for these reactions are defined by

$$D_{lv} = \frac{P}{C_l} \quad (73)$$

where  $P$  (bar) is the equilibrium partial pressure of the species in the vapor phase and  $C_l$  is its concentration in the liquid phase. Expressions for the distribution coefficients are obtained from thermodynamic data given in the chapter by Cobble and Lin in the ASME Handbook on Water technology [12]. Equilibrium constants for these reactions, defined by equation (47), are calculated from the distribution coefficients according to

$$K_{lv} = 100 \times \frac{D_{lv}}{RT} \quad (74)$$

This gives the equilibrium constant in units of mol dm<sup>-3</sup>/mol kg<sup>-1</sup>. Its conversion to units of mol dm<sup>-3</sup>/mol dm<sup>-3</sup> will be described in Section 4.3. Calculations show that the mass transfer rate should be governed by diffusion within the vapor and that the rate constant may be approximated simply by

$$k_m = D_v/r_c \quad (75)$$

#### (6) Radiolysis chemistry of water

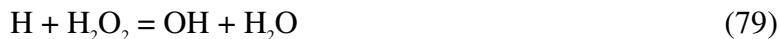
Neutron, gamma and alpha radiation interacts with water causing it to decompose to the radical products e<sup>-</sup>, H<sup>+</sup>, H, and OH and the molecular products H<sub>2</sub> and H<sub>2</sub>O<sub>2</sub>. Gamma radiation gives largely radical species, while alpha and neutron radiation give largely molecular species. The yields for the different species are expressed through the G-values, which determine the number of molecules produced per 100 eV of radiation energy absorbed. The G-values for gamma and neutron radiation are taken from the report by Henshaw and Tuson [13], while the G-values for alpha radiation come from the discussion in Appendix E. The source of alpha radiation is the <sup>10</sup>B(n, α)<sup>7</sup>Li reaction. This reaction and the parameters that govern its rate are discussed in Appendix E. The dose rate from both the alpha particles and <sup>7</sup>Li nuclei are taken into account in the model with the combined rate given by

$$D_\alpha^r = 5.647 \times 10^{-12} \frac{\phi[B]}{\rho_w} \text{ Mrad h}^{-1} \quad (76)$$

where  $\phi$  (cm<sup>-2</sup> s<sup>-1</sup>) is the neutron flux,  $[B]$  (mol dm<sup>-3</sup>) is the total boron concentration and  $\rho_w$  (g cm<sup>-3</sup>) is the density of water. This expression is obtained using the parameters given in Appendix E, assuming negligible neutron flux attenuation and all the energy from the alpha particles and <sup>7</sup>Li nuclei is absorbed locally. The alpha dose can become very large at the bottom of the deposit where the boron concentration can increase to more than ten times its value in the bulk coolant.

### Crud Chemistry Model (CCM)

The primary radiolytic species undergo a series of chemical reactions, including



In total there are between thirty and forty radiolysis reactions in the model. The rate constants for use in high temperature water come from the report by Elliot [14].

## 4.3 Thermodynamic Problems

This section discusses four thermodynamic problems that must be taken into account by the model: the different concentration units used for rate constants and equilibrium constants and the non-ideal parameters that enter equilibrium expressions; the calculation of non-ideal parameters; the effect of solute concentration on the saturation temperature; and the effect of temperature on the vaporization enthalpy of water.

### 4.3.1 Equilibrium expressions

The units of concentration used for aqueous solution species in the model are moles per unit volume of solution, whereas those used for thermodynamic equilibrium constants involving these species are moles per unit mass of water. The practical units are  $\text{mol dm}^{-3}$  and  $\text{mol kg}^{-1}$ , also known as molar and molal units respectively. It is necessary to be able to convert between these two units, which in the model is done in the following way.

Consider 1 kg of water containing dissolved solutes whose molal concentrations are  $m_s$ . The volume of the solution  $V$  may be expressed approximately by the following equation,

$$V = \sum V_s^m m_s + 1 / \rho_w \quad (82)$$

where  $V_s^m$  is the molar volume of the  $s^{\text{th}}$  solute,  $\rho_w$  is the density of water in  $\text{kg dm}^{-3}$  and the sum is over all dissolved species. The concentrations  $c_s$  are equal to  $m_s/V$ , which, using equation (82), may be written in the form,

$$c_s = \frac{m_s}{\sum V_s^m m_s + 1 / \rho_w} \quad (83)$$

Multiplying both sides by  $V_s^m$ , summing over  $s$  and solving for the molal concentration sum gives

$$\sum m_s V_s^m = \frac{1}{\rho_w} \frac{\sum c_s V_s^m}{1 - \sum c_s V_s^m} \quad (84)$$

Using equations (83) and (84), the molal concentration may be expressed in the following form,

$$m_s = \frac{c_s}{\rho_w \zeta} \quad (85)$$

where  $\zeta$  is given by

$$\zeta = 1 - \sum m_s V_s^m \quad (86)$$

Equations (85) and (86) provide the method used in the model to convert between molal and molar units. Table 4-1 lists the molar volumes of the species included in the summation in equation (86). Other species present are omitted because their concentrations are too small to be important.

**Table 4-1**  
**Molar volumes of dissolved species.**

Species	Molar Volume (dm <sup>3</sup> )
B(OH) <sub>3</sub>	0.03
B(OH) <sub>4</sub> <sup>-</sup>	0.03
B <sub>2</sub> O(OH) <sub>5</sub> <sup>-</sup>	0.06
B <sub>3</sub> O <sub>3</sub> (OH) <sub>4</sub> <sup>-</sup>	0.09
B <sub>3</sub> O <sub>3</sub> (OH) <sub>3</sub>	0.09
Li <sup>+</sup>	0.0025
H <sub>2</sub>	0.006

Equilibrium expressions for reactions in solution involve products of molal concentrations with activity coefficients, which correct for the non-ideality of the solution. Consider for example a hypothetical reaction,



In the model the rate of change of the concentration of A would be described by the following rate equation,

$$\frac{dc_A}{dt} = -k_f c_A c_B + k_r c_C \quad (88)$$

*Crud Chemistry Model (CCM)*

where the  $c$  are molar concentrations, and  $k_f$  and  $k_r$  are the rate constants for the forward and reverse reactions. At equilibrium in the steady state,  $dc_A/dt = 0$  and the ratio of the forward and reverse rate constants is given by

$$\frac{k_f}{k_r} = \frac{c_C}{c_A c_B} \quad (89)$$

where the  $c$  are now equilibrium molar concentrations. The thermodynamic equilibrium expression for this reaction is given by

$$K = \frac{m_C}{m_A m_B} \frac{\gamma_C}{\gamma_A \gamma_B} \quad (90)$$

where the  $m$  are molal concentrations and the  $\gamma$  are activity coefficients. Converting the molal concentrations in equation (90) to molar concentrations using equation (85) and combining with equation (89) leads to the following expression for the ratio of the forward and reverse rate constants,

$$\frac{k_f}{k_r} = \frac{K}{\zeta \rho_w} \frac{\gamma_A \gamma_B}{\gamma_C} \quad (91)$$

This would be the relation used by the model to express an unknown rate constant in terms of a known one and the equilibrium constant. Of the parameters on the right hand side of this equation,  $K$  and  $\rho_w$  are functions of temperature,  $\zeta$  is a function of concentration, and the  $\gamma$ 's are functions of both temperature and concentration.

Another non-ideal parameter that enters into equilibrium expressions for reactions involving  $H_2O$  is the activity of water. Consider for example the ionization of water,



The equilibrium expression for this reaction is given by

$$K_w = \frac{m_{H^+} m_{OH^-}}{a_w} \gamma_1^2 \quad (93)$$

where  $K_w$  is the equilibrium constant,  $m$  are the molal concentrations,  $a_w$  is the activity of water and  $\gamma_1$  is the activity coefficient for univalent ions. The rate equation used in the model leads to the following expression for the ratio of the forward and reverse rate constants,

$$\frac{k_f}{k_r} = \frac{c_{H^+} c_{OH^-}}{a_w} \quad (94)$$

Converting the molal concentrations in equation (93) to molar concentrations using equation (85) and combining with equation (94) leads to the following expression for the ratio of the forward and reverse rate constants,

$$\frac{k_f}{k_r} = K_w \left( \frac{\zeta \rho_w}{\gamma_1} \right)^2 \quad (95)$$

In the model, equation (95) is used to calculate  $k_f$  from  $k_r$  and  $K_w$ , while the activity of water is included in the rate equation. Thus the rate of change of  $H^+$  concentration is given by

$$\frac{dc_{H^+}}{dt} = k_f a_w - k_r c_{H^+} c_{OH^-} \quad (96)$$

In the limit of infinite dilution, the parameter  $\zeta$ , the activity coefficients of the solutes and the activity of water are all equal to unity. The equilibrium constants obtained from the Elliot report for water radiolysis apply to this regime, although the concentrations have been expressed in molar units. Hence, in deriving expressions analogous to equations (91) and (95), the density of water,  $\rho_w$ , must be omitted since it has already been included.

#### 4.3.2 Calculation of Non-ideal parameters

The aqueous solution within the porous shell is composed of three different types of dissolved species, ions, dissolved gases, and boric acid and its trimer. The activity coefficients of these species are calculated by similar methods to those given in the MULTEQ [9] manual, although it was possible to make some simplifying approximations.

The activity coefficients for ions of absolute charge  $z$ ,  $\gamma_z$ , are calculated from the activity coefficient of univalent ions,  $\gamma_1$ , according to

$$\gamma_z = \gamma_1^{z^2} \quad (97)$$

The activity coefficient  $\gamma_1$  is calculated using the Meissner equations, fitted to NaCl solutions over the temperature range 100-350°C [8]. These equations express  $\gamma_1$  in the following form,

$$\gamma_1 = \left[ 1 + B(1 + 0.1I)^q - B \right] \Gamma^* \quad (98a)$$

$$B = 0.75 - 0.065q \quad (98b)$$

$$\log_{10} \Gamma^* = -\frac{AI^{1/2}}{1 + CI^{1/2}} \quad (98c)$$

*Crud Chemistry Model (CCM)*

$$A = 0.484582 + 0.158173(T_c/100) - 0.214065(T_c/100)^2 + 0.256199(T_c/100)^3 - 0.105332(T_c/100)^4 + 0.0157603(T_c/100)^5 \quad (98d)$$

$$q = 2.95869 - 0.321502(T_c/100) - 0.105332(T_c/100)^2 \quad (98e)$$

In these equations,  $T_c$  is the temperature in °C and  $I$  is the ionic strength, given by

$$I = \frac{1}{2} \sum_{ions} m_i z_i^2 \quad (99)$$

where the sum is over all ionic species of molal concentration  $m_i$  and charge  $z_i$ . The term in the equation for  $\gamma_1$  arising from the interaction between ions and dissolved gasses has been omitted since it is negligible at the concentrations found in the porous shell.

The activity coefficient for dissolved gases,  $\gamma_a$ , is calculated from equations designed to model salting out of carbon dioxide and given by [9]

$$\ln \gamma_a = 1.6118(1 - \exp(-B_a I)) \quad (100a)$$

$$B_a = 10^{-1.9826 + 0.00495 T_c} \quad (100b)$$

where as before  $I$  is the ionic strength and  $T_c$  is the temperature in °C.

The activity coefficients of boric acid and its trimer are calculated by setting them equal to the activity of water. This is the method described in the MULTEQ [9] manual, which was adapted from the thermodynamic study of concentrated sodium borate solutions at high temperature by Weres [10]. The activity of water is derived from the Gibbs-Duhem [15] relation. Consider first a hypothetical solution consisting only of neutral boric acid and its trimer. Setting their activity coefficients,  $\gamma_c$ , equal to the activity of water,  $a_w$ , the Gibbs-Duhem relation,

$$m_w d \ln a_w + \sum_c m_c d \ln(a_w m_c) = 0, \quad (101)$$

leads to the following expression for  $a_w$ ,

$$a_w = \frac{m_w}{m_w + \sum_c m_c} \quad (102)$$

In these last two equations,  $m_w$  is the molal concentration of water, equal to 55.509 mol kg<sup>-1</sup>, the sums are over boric acid and its trimer, and  $m_c$  is their molal concentration.

The assumption,  $\gamma_c = a_w$ , is equivalent to assuming that boric acid and its trimer dissolve in water to give an ideal solution. This may be proved in the following way. In an ideal solution, the chemical potential of each component,  $\mu_i$ , is given by

$$\mu_i = \mu_i^0 + RT \ln x_i \quad (103)$$

where  $x_i$  is the mole fraction of component  $i$  and  $\mu_i^0$  is the chemical potential of  $i$  in its pure liquid state. Applied to water, this equation leads directly to

$$\mu_w = \mu_w^0 + RT \ln a_w \quad (104)$$

with the activity  $a_w$  given by equation (102). Applied to boric acid or its trimer, equation (103) gives

$$\mu_c = \mu_c^0 - RT \ln m_w + RT \ln \left( \frac{m_c}{m_w + \sum m_c} \right) \quad (105)$$

which may be rewritten in the form,

$$\mu_c = \mu_c^{0'} + RT \ln(\gamma_c m_c)$$

where  $\mu_c^{0'} = \mu_c^0 - RT \ln m_w$  is the chemical potential of  $c$  in the infinitely dilute solution and the activity coefficient,  $\gamma_c$ , is given by  $\gamma_c = a_w$ . This completes the proof. That boric acid and its trimer should dissolve in water to give an ideal solution is justified by the similarity between their molecular structure and that of water. All three are neutral molecules with hydroxyl groups that will interact with one another via hydrogen bonding to a similar degree. Equality of interaction between solute-solute, solvent-solvent and solute-solvent molecules is a necessary condition for the formation of an ideal solution.

Equation (102) for the activity of water strictly holds only for solutions of boric acid and its trimer. It is possible to derive a more complicated expression from the Gibbs-Duhem relation that is applicable to a solution containing all three different types of dissolved species, ions, dissolved gases, and boric acid and its trimer. In practice, it is found that the values obtained from this more complicated expression are little different from those obtained using the simple expression in equation (102). This is not too surprising since the concentrations of boric acid and its trimer are much greater than those of ions and dissolved gasses. An even better approximation is obtained by extending the sum in equation (102) to all species present in solution,

$$a_w = \frac{m_w}{m_w + \sum_{all} m_i} \quad (106)$$

This equation gives values that differ from those obtained using the complete expression by no more than  $2 \times 10^{-4}$  and it is the one implemented in the model.

### Crud Chemistry Model (CCM)

Another useful approximation implemented in the model, is to restrict the summations over species concentrations in equations (86), (99) and (106) to the following seven species:  $B(OH)_3$ ,  $B(OH)_4^-$ ,  $B_2O(OH)_5^-$ ,  $B_3O_3(OH)_4^-$ ,  $B_3O_3(OH)_3$ ,  $Li^+$ ,  $H_2$ . In practice, this approximation is a very good one since the concentrations of the omitted species are negligible in comparison with those that have been included. This approximation is much more useful than merely saving a few additions. It greatly reduces the size of the Jacobian and Newton matrices, used by the stiff differential equation solver in FACSIMILE, by eliminating unimportant interdependencies amongst the species concentrations and therefore speeding up the calculations considerably.

The activity of water determined by equation (106) is referenced to the saturation pressure of pure water,  $P_0$ , at the local temperature,  $T$ , within the porous deposit. Since this pressure is higher than the system pressure,  $P_{sys}$ , equal to the saturation pressure of the bulk solution, it is necessary to apply a correction. This is obtained using the thermodynamic relation

$$RT \left( \frac{\partial \ln a_w}{\partial P} \right)_T = \frac{\bar{V}_w^l}{RT} \quad (107)$$

to give

$$\ln(a_w(P_{sys})/a_w(P_0)) = \frac{1}{RT} \int_{P_0}^{P_{sys}} \bar{V}_w^l dP \quad (108)$$

where  $\bar{V}_w^l$  is the partial molar volume of water in the solution. The method used for the evaluation of the integral in equation (108) is described in Section 4.4. A similar correction should also be applied to the activity coefficients of ions and dissolved gases, but this has been omitted from the model since the different species molar volumes would destroy the simplicity of only two different activity coefficients,  $\gamma_0$  and  $\gamma_1$ . This omission is justified by the smallness of the correction factor.

#### 4.3.3 Saturation temperature

The increase in solute concentrations in the solution within the porous shell gives rise to an increase in the saturation temperature of water. This must be taken into account for a realistic treatment of heat transfer and fluid flow within the deposit. An expression from which the saturation temperature may be derived is obtained by considering the equilibrium between water vapor and water in the solution. The condition for equilibrium at temperature  $T$  is given by

$$\mu_w^0(P_0) + RT \ln a_w(P) = \mu_v(P) \quad (109)$$

where  $\mu_w^0(P_0)$  is the chemical potential of pure water,  $a_w$  is the activity of water in solution,  $\mu_v$  is the chemical potential of water vapor,  $P_0$  is the vapor pressure of pure water and  $P$  is the vapor pressure of the solution. The condition for equilibrium between pure water and its vapor is

$$\mu_w^0(P_0) = \mu_v(P_0) \quad (110)$$

Subtracting equation (110) from (109), gives

$$-RT \ln a_w(P) = \mu_v(P_0) - \mu_v(P) = \int_P^{P_0} \bar{V}_w^v dP \quad (111)$$

where the last equality follows from the thermodynamic relation  $\partial\mu/\partial P = \bar{V}$  and  $\bar{V}_w^v$  is the molar volume of water vapor or steam. The solution in the porous shell boils when its vapor pressure,  $P$ , becomes equal to the system pressure,  $P_{sys}$ . Making this substitution in equation (111) and using equation (108) to replace  $a_w(P_{sys})$  by  $a_w(P_0)$  gives

$$\ln a_w(P_0) + \frac{1}{RT} \int_{P_{sys}}^{P_0} (\bar{V}_w^v - \bar{V}_w^l) dP = 0 \quad (112)$$

The activity of water appearing in this equation is the value obtained from equation (106) before the pressure correction of equation (108) has been applied. The left hand side of this equation is a non-linear function of temperature whose zero gives the saturation temperature  $T_s$ . The equation was solved using Brent's method [16] in a standalone computer program that was used to generate a series of values of  $T_s$  versus  $a_w$ . These were fitted to a polynomial equation for  $T_s$ , which was incorporated into the model. The methods used for the evaluation of the integral in equation (112) and the polynomial equation for  $T_s$  will be given in Section 4.4.

#### 4.3.4 Vaporization enthalpy of water

The vaporization enthalpy of water,  $H_v$ , is an important parameter in the thermal hydraulic equations. It occurs directly in the equation for the liquid velocity and indirectly in the equation for the deposit temperature via the dependence of the coefficient of evaporative heat transfer on its value. An expression for the vaporization enthalpy of water in the solution within the porous shell is obtained starting from equation (109) above with  $P$  replaced by  $P_{sys}$ . This is converted into an equation for  $H_v$  using the thermodynamic relation,

$$\frac{\partial(\mu/T)}{\partial T} = -\frac{\bar{H}}{T^2} \quad (113)$$

where  $\mu$  is the chemical potential and  $\bar{H}$  is the partial molar enthalpy. After using equation (108) to replace  $a_w(P_{sys})$  by  $a_w(P_0)$ , the following expression for  $H_v$  is obtained,

$$H_v = H_v^0 - \int_{P_{sys}}^{P_0} (\bar{V}_w^v - \bar{V}_w^l) dP + T \int_{P_{sys}}^{P_0} \frac{\partial}{\partial T} (\bar{V}_w^v - \bar{V}_w^l) dP + RT^2 \frac{\partial \ln a_w}{\partial T} \quad (114)$$

where  $H_v^0$  is the vaporization enthalpy of pure water,  $\bar{V}_w^v$  is the molar volume of steam,  $\bar{V}_w^l$  is the partial molar volume of water in the solution, and  $a_w$  is the activity of water, given here by equation (106) before the pressure correction is applied. Reference to equation (106) shows that

### Crud Chemistry Model (CCM)

$a_w$  is independent of temperature, hence, the last term in equation (114) is zero. Equation (114) was incorporated into a standalone computer program that was used to generate a series of values of  $H_v$  versus  $T$ . These were fitted to a simple function of  $T$  for use in the model. The methods used to evaluate the integrals in equation (114) and the resulting fitted function of  $H_v(T)$  will be described in Section 4.4.

## 4.4 High Temperature Water and Solution Properties

This section summarizes the methods used to calculate various properties of pure water and the solution within the porous shell for use in the FACSIMILE model and its companion computer programs. It will also describe the calculation the thermal conductivity of the deposit and the coefficient of evaporative heat transfer.

### 4.4.1 Pure water properties

Correlations for the vapor pressure of water and the densities of liquid water and steam were taken from Keenan and Keyes [17], the same as those used in MULTEQ [9].

The vapor pressure of water is given by

$$P_0 = 218.167 \times 10^{-g_0} \text{ atm} \quad (115)$$

where for  $T_c > 50^\circ\text{C}$

$$g_0 = \frac{\theta}{T_{kk}} \frac{3.346313 + 0.0414113\theta + 7.515485 \times 10^{-9}\theta^3 + 6.56444 \times 10^{-11}\theta^4}{1 + 0.013794481\theta} \quad (116)$$

and where  $\theta$  and  $T_{kk}$  are related to the absolute temperature  $T$  by

$$\begin{aligned} \theta &= 647.25 - T, \\ T_{kk} &= T + 0.01 \end{aligned} \quad (117)$$

The saturated density of liquid water is given by

$$\rho_w^{sat} = \frac{1 + 0.1342489\theta^{1/3} - 3.946263 \times 10^{-3}\theta}{3.1975 - 0.3151548\theta^{1/3} - 1.203374 \times 10^{-3}\theta + 7.489081 \times 10^{-13}\theta^4} \text{ g cm}^{-3} \quad (118)$$

where  $\theta$  is given by equation (117).

The density of steam is given by

$$\rho_s = \frac{1}{4.5549/\lambda + b_0 + b_0^2 g_1 \lambda + b_0^4 g_2 \lambda^3 - b_0^{13} g_3 \lambda^{12}} \text{ g cm}^{-3} \quad (119)$$

where

$$\tau = 1/T_{kk} \quad (120)$$

$$\lambda = P\tau \quad (121)$$

$$b_0 = 1.89 - 2641.62 \times 10^{80870\tau^2} \tau \quad (122)$$

$$g_1 = 82.54601\tau - 162460\tau^2 \quad (123)$$

$$g_2 = 0.21828 - 126970\tau^2 \quad (124)$$

$$g_3 = 3.635 \times 10^{-4} - 6.768 \times 10^{64} \tau^{24} \quad (125)$$

In these equations  $P$  is the pressure in atmospheres and  $T_{kk}$  is related to the temperature  $T$  by equation (117).

The following equation for the vaporization enthalpy of pure water was obtained by fitting values from steam tables [18],

$$H_v^0 = \frac{12.28917\theta + 1.2084\theta^2 + 0.002445\theta^3 - 1.982787 \times 10^{-6}\theta^4}{1 + 1.730276\theta + 0.03722\theta^2} \text{ kJ mol}^{-1} \quad (126)$$

where  $\theta$  is given by equation (117). This equation gives  $H_v^0$  to an accuracy of 0.1 kJ mol<sup>-1</sup> from 0°C up to the critical temperature at 374.1°C.

The following equation for the thermal conductivity of water was obtained by fitting values [19] for water in equilibrium with steam over the temperature range 100-350°C,

$$k_c^w = 616 + 0.946T_c - 0.00282T_c^2 - 3.61 \times 10^{-6}T_c^3 \text{ mW m}^{-1} \text{ K}^{-1} \quad (127)$$

where  $T_c$  is the temperature in °C.

#### 4.4.2 Solution properties

The density of water,  $\rho_w$ , that occurs in the thermal hydraulic equations should strictly be defined as the density of water in the solution. It was approximated in the model by the saturated density of water,  $\rho_w^{sat}$ , and calculated by equation (118) above. This neglects any direct effect that dissolved solutes may have on the density of water. This is reasonable since boric acid and its trimer, which are the most important solutes by concentration, are assumed to interact with water like water itself. The approximation also neglects the compressibility of water, which is also reasonable because it is indeed very small except at temperatures very close to the critical point

*Crud Chemistry Model (CCM)*

of water. The same approximation enables the partial molar volume of water in solution,  $\bar{V}_w^l$ , to be expressed simply by

$$\bar{V}_w^l = \frac{18.015}{\rho_w^{sat}} \text{cm}^3 \text{mol}^{-1} \quad (128)$$

The integral of  $\bar{V}_w^l$  over pressure, which occurs in the equations for  $a_w$ ,  $T_s$  and  $H_v$ , is then given by

$$\int_{P_0}^{P_{sys}} \bar{V}_w^l dP = \frac{1.8254}{\rho_w^{sat}} (P_{sys} - P_0) \text{ J mol}^{-1} \quad (129)$$

The integral of  $\partial \bar{V}_w^l / \partial T$  over pressure, which occurs in the equation for  $H_v$ , is obtained from equations (128) and (118) to give

$$\begin{aligned} \int_{P_0}^{P_{sys}} \frac{\partial \bar{V}_w^l}{\partial T} dP &= 1.8254 (P_{sys} - P_0) \times \left[ g_4 (4.474963 \times 10^{-2} \theta^{-2/3} - 3.946263 \times 10^{-3}) / g_5^2 \right. \\ &\quad \left. + (0.1050516 \theta^{-2/3} - 2.995632 \times 10^{-12} \theta^3 + 1.203374 \times 10^{-3}) / g_5 \right] \text{ J K}^{-1} \text{ mol}^{-1} \end{aligned} \quad (130)$$

where

$$g_4 = 3.1975 - 0.3151548 \theta^{1/3} - 1.203374 \times 10^{-3} \theta + 7.489081 \times 10^{-13} \theta^4 \quad (131)$$

$$g_5 = 1 + 0.1342489 \theta^{1/3} - 3.946263 \times 10^{-3} \theta \quad (132)$$

The partial molar volume of water in the vapor is determined directly from the density of steam,

$$\bar{V}_w^v = \frac{18.015}{\rho_s} \text{cm}^3 \text{mol}^{-1} \quad (133)$$

The integral of  $\bar{V}_w^v$  over pressure, which occurs in the equations for  $T_s$  and  $H_v$ , is obtained from equations (133) and (119) to give

$$\begin{aligned} \int_{P_{sys}}^{P_0} \bar{V}_w^v dP &= 8.3145 \times T \ln \left( \frac{P_0}{P_{sys}} \right) + 1.8254 \left[ b_0 (P_0 - P_{sys}) + b_0^2 g_1 \tau (P_0^2 - P_{sys}^2) / 2 \right. \\ &\quad \left. + b_0^4 g_2 \tau^3 (P_0^4 - P_{sys}^4) / 4 - b_0^{13} g_3 \tau^{12} (P_0^{13} - P_{sys}^{13}) / 13 \right] \text{ J mol}^{-1} \end{aligned} \quad (134)$$

where  $\tau$ ,  $b_0$ ,  $g_1$ ,  $g_2$  and  $g_3$  are given by equations (120) and (122)-(125).

The integral of  $\partial\bar{V}_w^v/\partial T$  over pressure, which occurs in the equation for  $H_v$ , is obtained from equations (133) and (119) to give

$$\int_{P_{sys}}^{P_0} \frac{\partial\bar{V}_w^v}{\partial T} dP = 8.3145 \times \ln\left(\frac{P_0}{P_{sys}}\right) + 1.8254[b'_0(P_0 - P_{sys}) + a_1(P_0^2 - P_{sys}^2)/2 + a_2(P_0^4 - P_{sys}^4)/4 + a_3(P_0^{13} - P_{sys}^{13})/13] \text{ J K}^{-1} \text{ mol}^{-1} \quad (135)$$

where

$$b'_0 = 2641.62\tau^2 10^{80870\tau^2} (1 + 3.7242 \times 10^5 \tau^2) \quad (136)$$

$$a_1 = 2b_0 b'_0 g_1 \tau + b_0^2 g'_1 \tau - b_0^2 g_1 \tau^2 \quad (137)$$

$$a_2 = 4b_0^3 b'_0 g_2 \tau^3 + b_0^4 g'_2 \tau^3 - 3b_0^4 g_2 \tau^4 \quad (138)$$

$$a_3 = 13b_0^{12} b'_0 g_3 \tau^{12} + b_0^{13} g'_3 \tau^{12} - 12b_0^{13} g_3 \tau^{13} \quad (139)$$

$$g'_1 = -82.54601\tau^2 + 324920\tau^3 \quad (140)$$

$$g'_2 = 253940\tau^3 \quad (141)$$

$$g'_3 = 1.624326 \times 10^{66} \tau^{25} \quad (142)$$

and where  $\tau$ ,  $b_0$ ,  $g_1$ ,  $g_2$  and  $g_3$  are given by equations (120) and (122)-(125). As a useful check on the correctness of equations (130) and (134) for the integrals of  $\partial\bar{V}_w^l/\partial T$  and  $\partial\bar{V}_w^v/\partial T$  over pressure, the values obtained from them were shown to be the same as those obtained by numerical differentiation of the corresponding integrals for the partial molar volumes.

The saturation temperature,  $T_s$ , as a function of the activity of water,  $a_w$ , is given by

$$T_s = 344.94 + 199.01(1 - a_w) - 952.74(1 - a_w)^2 + 26013.91(1 - a_w)^3 - 262916.0(1 - a_w)^4 + 997166.1(1 - a_w)^5 \text{ } ^\circ\text{C} \quad (143)$$

This equation was obtained by fitting a series of values of  $T_s$  versus  $a_w$  for a bulk coolant temperature of 345.4°C and a corresponding system pressure of 153.42 atm. The series of values of ( $a_w$ ,  $T_s$ ), obtained by the method described in Section 4.3.3, covered the range from (0.999, 345.18) to (0.874, 372.56). Figure 4-1 shows a plot of the calculated points and the fitted polynomial curve.

Crud Chemistry Model (CCM)

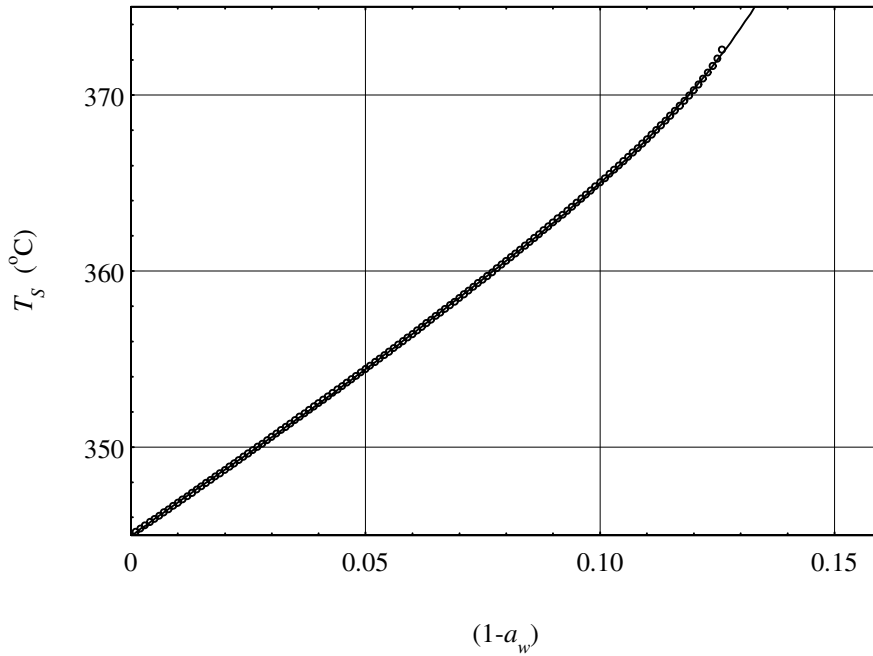


**Figure 4-1**  
**Calculated points and fitted polynomial line for saturation temperature as a function of the activity of water.**

The vaporization enthalpy of water in the solution within the porous shell,  $H_v$ , is given by

$$H_v = \frac{12.582\theta_H + 7.02378\theta_H^2 + 0.0765443\theta_H^3 - 2.11787 \times 10^{-3}\theta_H^4}{1 + 1.36248\theta_H + 0.407087\theta_H^2} \text{ kJ mol}^{-1} \quad (144)$$

where  $\theta_H$  is related to the temperature in °C,  $T_c$ , by

$$\theta_H = 373.09 - T_c \quad (145)$$

Equation (144) was obtained by fitting a series of values of  $H_v$  versus  $T_c$  for a bulk coolant temperature of 345.4°C and a corresponding system pressure of 153.42 atm. The series of values of  $H_v$  versus  $T_c$  were obtained by the method described in Section 4.3.4. Figure 4-2 shows a plot of  $H_v$  versus  $T_c$  and for comparison a plot of  $H_v^0$  versus  $T_c$ . The vaporization enthalpy for pure water decreases to zero at a temperature of 374.1°C. This is the critical temperature of water where the densities of water and steam become equal. The vaporization enthalpy of water in solution also decreases to zero, but at a slightly different temperature of 373.09°C. This is not the critical temperature for the solution since the densities of water and steam are not equal. The density of water in the solution (0.39 g cm<sup>-3</sup>) at 373.09°C is close to the critical density (0.31 g cm<sup>-3</sup>), at 374.1°C. However, the steam density (0.077 g cm<sup>-3</sup>) is less than the critical density (0.21 g cm<sup>-3</sup>) because the system pressure (153.42 atm) is less than the critical pressure (218.17 atm). The calculated vaporization enthalpy of water in solution is subject to error as a result of the

approximation of neglecting the compressibility of water. Rough estimates of the magnitude of this error showed it to be small and negative, and that the true value is a little less than the approximate value.

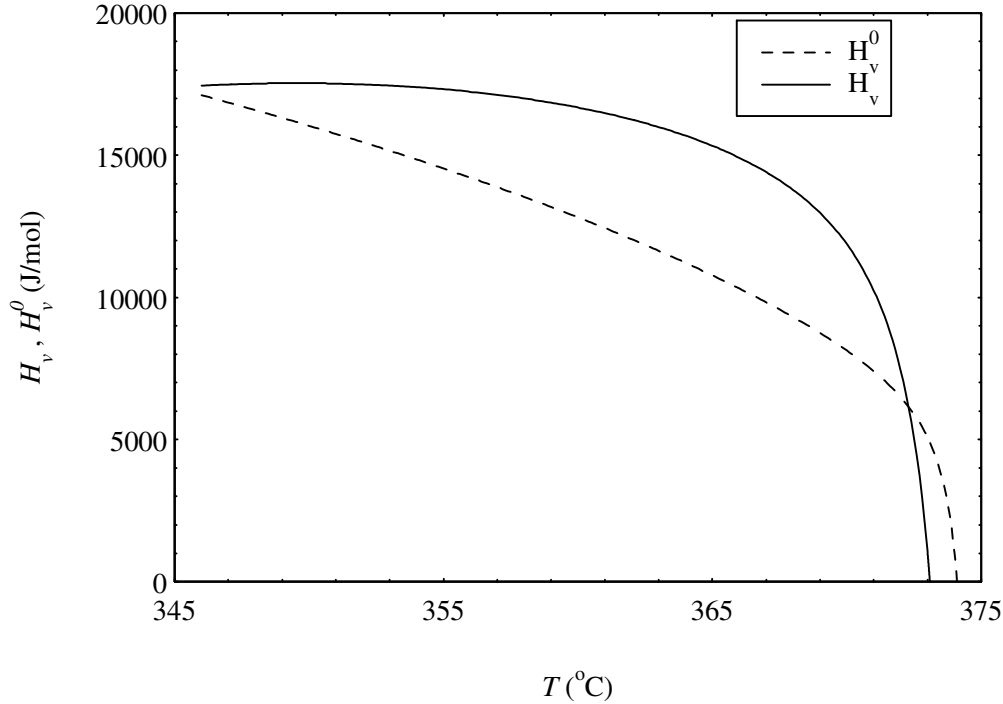


**Figure 4-2**  
**Vaporization enthalpy of water in solution,  $H_v$ , and of pure water,  $H_v^0$  versus temperature.**

#### 4.4.3 Heat Transfer Parameters

This section describes how the thermal conductivity of the deposit and the coefficient of evaporative heat transfer are calculated in the model.

The thermal conductivity of the deposit,  $k_c$ , is calculated from Maxwell's formula[20]

$$k_c = k_c^w \frac{1 - (1 - ak_c^s)(1 - \varepsilon)}{1 + (a - 1)(1 - \varepsilon)} \quad (146)$$

where

$$a = \frac{3k_c^w}{2k_c^w + 2k_c^s} \quad (147)$$

*Crud Chemistry Model (CCM)*

and where  $k_c^w$  is the conductivity of water and  $k_c^s$  is the conductivity of the solid deposit. This equation is valid for values of  $\varepsilon > 0.5$ . The conductivity of water is calculated from equation (127), while the conductivity of the solid is taken to be  $4.5 \text{ W m}^{-1} \text{ K}^{-1}$ , the value quoted by Pan et al. [21] for magnetite.

The coefficient of evaporative heat transfer,  $h_e$ , is calculated from a similar formula to that used by Pan et al. [21],

$$h_e = \left( \frac{2A}{2-A} \right) \left( \frac{M}{2\pi R} \right)^{1/2} \frac{H_v^2}{T^{3/2} (\bar{V}_w^v - \bar{V}_w^l)} \quad (148)$$

where  $A$  is the evaporation or condensation coefficient,  $M$  is the molecular weight of water,  $R$  is the gas constant,  $H_v$  is the vaporization enthalpy,  $T$  is the local deposit temperature,  $\bar{V}_w^v$  is the molar volume of steam and  $\bar{V}_w^l$  is the molar volume of water. The value used for the term  $(2A/(2-A))$  was 0.04, the same as that used by Pan et al. [21]. Equation (148) is derived on the basis of the Schrage [22] model for the evaporative mass flux combined with the Clausius-Clapeyron [15] equation for the rate of change of vapor pressure with respect to temperature. The following approximations are made in its derivation: (1) the evaporation velocity is small compared with a characteristic molecular velocity,  $(2RT/M)^{1/2}$ ; (2) the temperatures of the vapor and liquid and the saturation temperature are approximately equal; (3) the vapor is a perfect gas. The first approximation is certainly valid but the other two are poor: the steam temperature is not in reality equal to the liquid temperature, as noted in Section 4.1.1; and steam at high temperature and pressure is not an ideal gas. It is possible to remove the need for approximations (2) and (3), while preserving the form of equation (148) at the expense of redefining the saturation temperature. Although this has not been investigated further, it is considered unlikely to have a large effect on the results obtained from the model.

# 5

## RESULTS FROM CRUD CHEMISTRY MODEL (CCM)

### 5.1 Standard Operating Conditions

Calculations have been performed using CCM over a wide range of operating conditions, the standard input conditions being those outlined in Table 5-1. Appendix B presents the results of Chapman who has carried out calculations to determine the typical conditions experienced by fuel elements present in AOA plants. In particular Chapman has calculated the heat fluxes, dose rates and neutron fluxes for such plants. Comparison of the conditions defined in Table 5-1 with those determined by Chapman show that the standard conditions given in Table 5-1 are close to those for plants undergoing AOA. The boundary conditions for the calculations are critical to the results of the model and care needs to be taken in choosing these conditions. In particular bulk soluble species concentrations have to be specified in the model, so at the start of the calculation along with the obvious species  $H_2$ ,  $B(OH)_3$ ,  $Li^+$ , concentrations of all other species ( $B(OH)_4^-$ ,  $B_2(OH)_7^-$ ,  $H_2O_2$ ,  $OH$ ,  $Fe^{2+}$ ,  $Fe(OH)^-$ ,  $Ni^{2+}$ , etc., 27 species in total) are specified. The bulk water concentrations are calculated using a PWR radiolysis circuit model [23].

**Table 5-1**  
**Standard input conditions for the CCM model**

Parameter	Value
Coolant temperature/°C	345.4
System pressure/atm	153.42
Chimney density/mm <sup>2</sup>	3000
Chimney radius/μm	2.5
Porosity	0.8
Tortuosity	2.5
Deposit depth/μm	25-60
Heat flux W/m <sup>2</sup>	10 <sup>6</sup>
Li/ppm	2
B/ppm	1200
H <sub>2</sub> /cc (STP) kg <sup>-1</sup>	25.3
γ Dose rate/Mrad h <sup>-1</sup>	1200
n Dose rate/Mrad h <sup>-1</sup>	2400
n Flux/cm <sup>2</sup> s <sup>-1</sup>	3.6x10 <sup>14</sup>

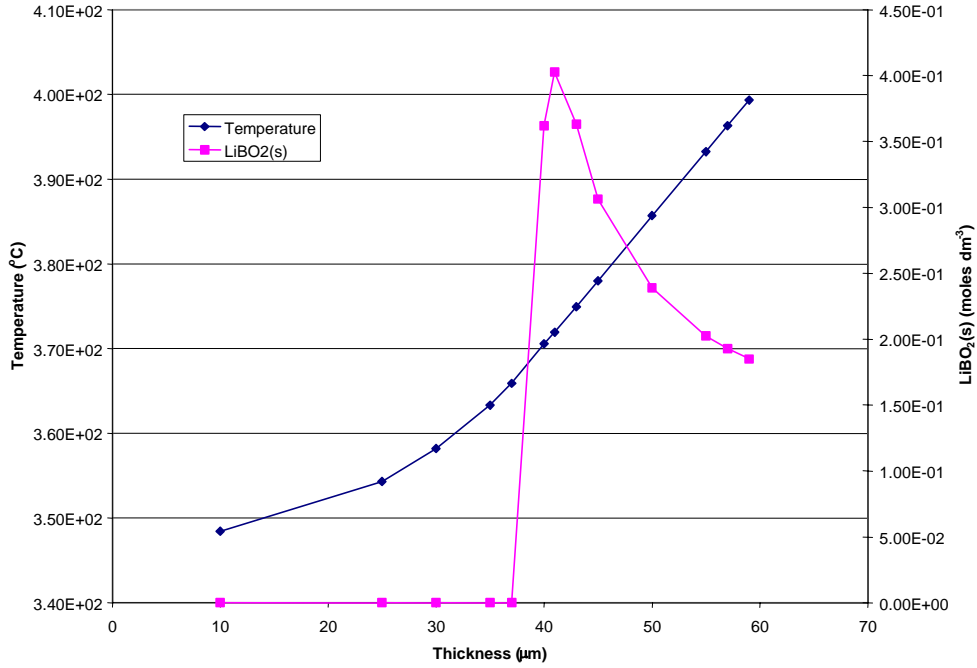
*Results From Crud Chemistry Model (CCM)*

Figure 5-1 shows the calculated deposit temperature and amount of solid  $\text{LiBO}_2(\text{s})$  present at the bottom of the deposit as a function of deposit thickness. Once precipitation is initiated the amount of  $\text{LiBO}_2(\text{s})$  at the bottom of the deposit falls with increasing film thickness, this is because  $\text{LiBO}_2(\text{s})$  precipitates out further up within the deposit. It should also be noted that the amount of  $\text{LiBO}_2(\text{s})$  in  $\text{moles dm}^{-3}$  is the amount produced once the model reaches steady state for the soluble species. This usually takes less than 10 seconds by which time molar quantities of  $\text{LiBO}_2(\text{s})$  have been generated. It is clear then that what will limit the amount of  $\text{LiBO}_2(\text{s})$  is simply the volume capacity of the pores in the deposit. The loss of porosity as a result of  $\text{LiBO}_2(\text{s})$  formation is not considered in the present calculations nor is there an upper limit set on the amount of  $\text{LiBO}_2(\text{s})$  that can precipitate and therefore the absolute amounts of  $\text{LiBO}_2(\text{s})$  reported here should not be used in quantifying the amount of total B within the deposit. From Figure 5-1  $\text{LiBO}_2(\text{s})$  is formed at a deposit thickness of  $37\mu\text{m}$ , while the deposit temperature is approaching the critical point of water ( $373^\circ\text{C}$ ) for a deposit thickness of  $42\mu\text{m}$ . Since the approach to the critical point means a fall in the evaporative heat loss and a consequent fall in evaporative loss of  $\text{H}_2\text{O}$ ,  $\text{H}_2$  and  $\text{H}_3\text{BO}_3$  then clearly a large change in the system behavior is occurring between  $37$  and  $42\mu\text{m}$ . The system chemistry may therefore be different above and below this range and therefore calculations of properties (e.g. pH and species concentrations) through the deposit are presented at  $35\mu\text{m}$  and  $59\mu\text{m}$ , which are below and above this critical region.

Figure 5-2 is a plot of the pH (at temperature) calculated through the deposit for a deposit of  $35\mu\text{m}$  thickness. The pH at the crud-water interface is approximately 7.7 (at  $x=0$  on the plot) and falls to 7.35 near the base of the deposit. This fall is primarily a result of the rise in boric acid concentration towards the bottom of the deposit, as shown in Figure 5-3. The boric acid concentration increases from  $7.5 \times 10^{-2}\text{M}$  to  $2.1\text{M}$ , while the lithium concentration changes from  $2 \times 10^{-4}$  to  $2.3 \times 10^{-2}$ . Although the lithium ion concentration also increases by a larger factor than the boric acid, which would increase the pH, the effect of concentrating the boric acid is more important and is simply a result of the thermodynamics for the Li/B system. The reason for this is explained in reference [5] but it is a consequence of the fact that poly-anions, such as  $\text{B}_2(\text{OH})_7^-$ ,  $\text{B}_3(\text{OH})_{10}^-$  become more important in the chemistry determining the pH, the higher the boric acid concentration.

In the model the deposit consists of  $\text{NiFe}_2\text{O}_4(\text{s})$  and  $\text{NiO}(\text{s})$  and their chemistry is included so it is possible to investigate how the solubility of Ni and Fe vary through the deposit. The other solids which are also allowed to exist in the model are Ni,  $\text{Fe}_3\text{O}_4(\text{s})$ . Figure 5-4 plots the soluble Ni/Fe ratio through the  $35\mu\text{m}$  deposit along with the  $\text{pH}_t$ . Clearly from this figure this ratio simply reflects the behavior of the pH through the deposit, at high pH the ratio is low and at low pH it is high. A higher soluble Ni/Fe ratio near the base of the deposit might imply a solid phase that is preferentially losing Ni compared to Fe in this region. Such interpretations should be viewed with caution at this stage in the model development. There are several factors not considered in this study which will affect the Ni/Fe behavior, such as radiolysis effects on Ni and Fe oxidation states and also the correct boundary conditions that apply at the water interface with regard cation concentrations. These factors will be taken into account in later studies.

Results From Crud Chemistry Model (CCM)



**Figure 5-1**  
 Temperature and amount of LiBO<sub>2</sub>(s) at the bottom of the deposit verses deposit depth.  
 Conditions: Boron 1200 ppm, Lithium 2 ppm, Heat Flux = 1.0  
 MW m<sup>-2</sup>, Bulk H<sub>2</sub> = 25cc(STP) kg<sup>-1</sup>.

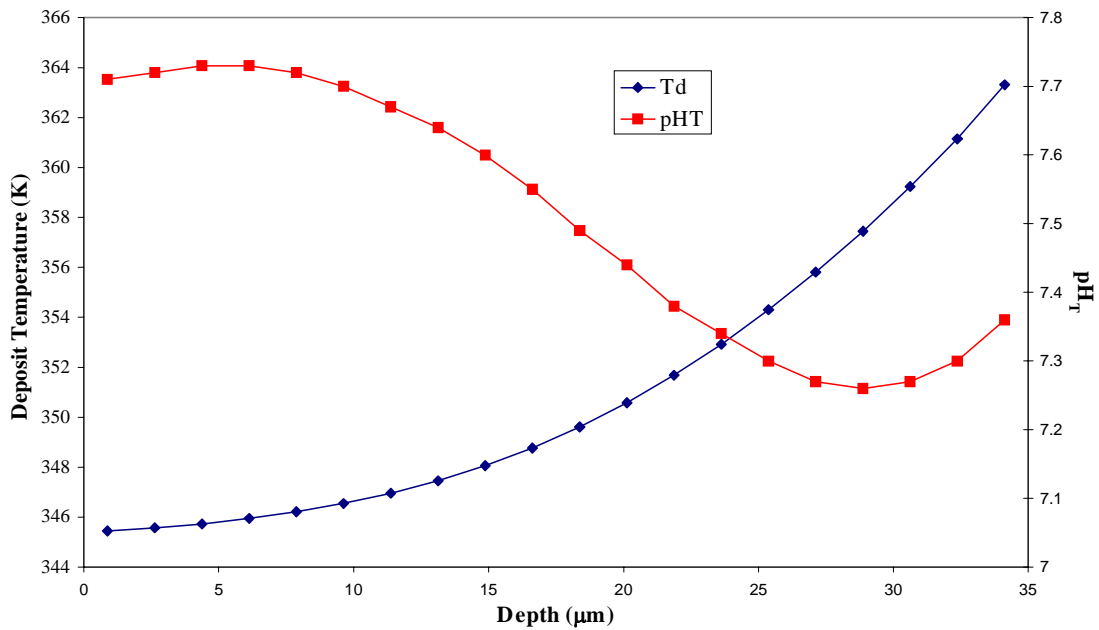


**Figure 5-2**  
 pH and crud temperature against deposit depth for a 35μm thick deposit. Calculation with  
 2ppm Li, 1200ppm B and 25cm<sup>3</sup> kg<sup>-1</sup> (STP) H<sub>2</sub>.

Results From Crud Chemistry Model (CCM)

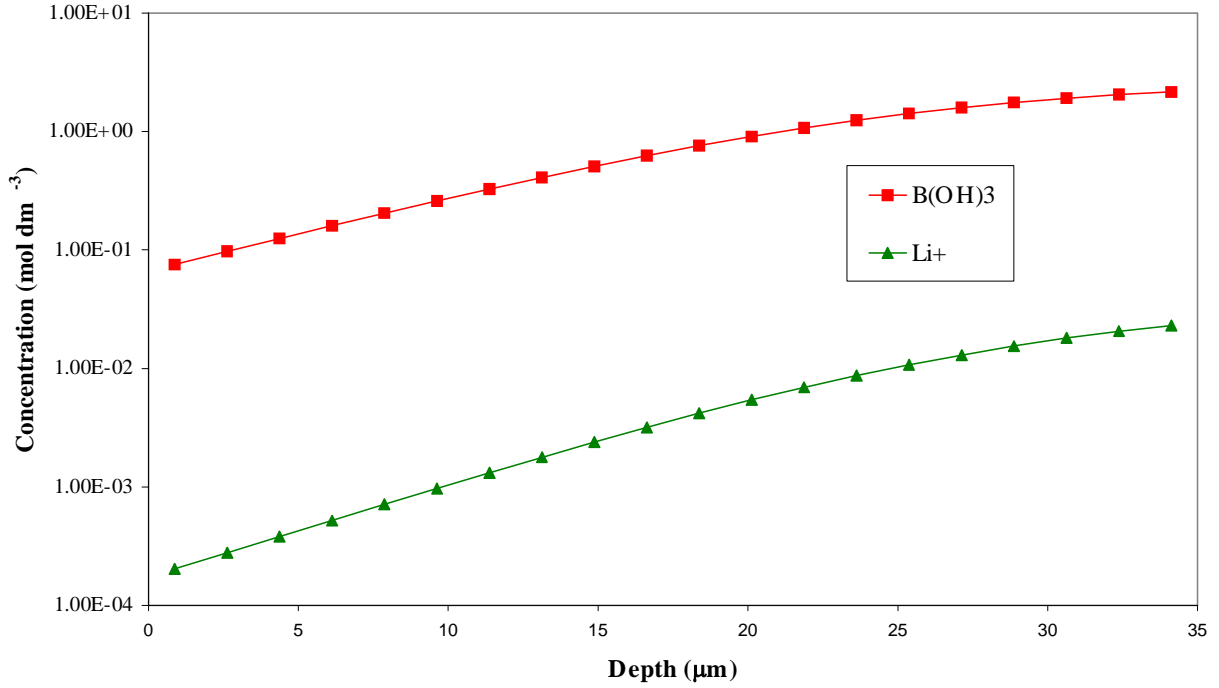


**Figure 5-3**  
 Boric acid and lithium ion concentration against depth for a 35μm thick deposit. Calculation with 2ppm Li, 1200ppm B and 25cm<sup>3</sup> kg<sup>-1</sup> (STP) H<sub>2</sub>.

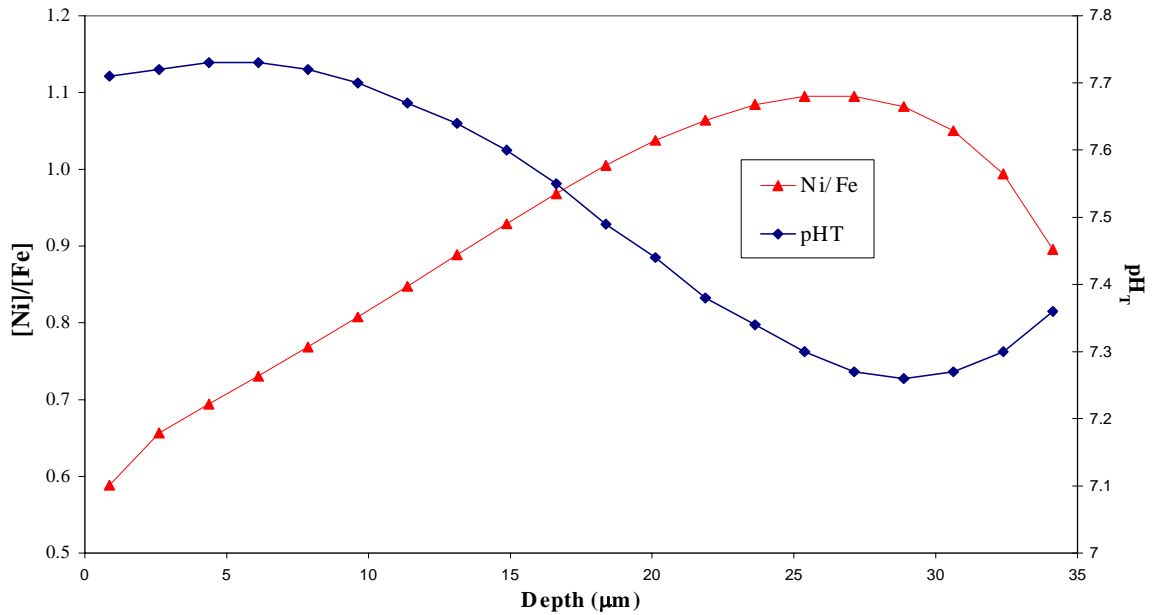


**Figure 5-4**  
 Soluble Ni/Fe ratio against depth for a 35μm thick deposit. Calculation with 2ppm Li, 1200ppm B and 25cm<sup>3</sup> kg<sup>-1</sup> (STP) H<sub>2</sub>.

Figure 5-5 is a plot of  $H_2$ ,  $H_2O_2$  and OH species concentrations through the 35 $\mu$ m deposit. Both  $H_2O_2$  and OH are the result of the radiolysis reactions of water within the deposit. The main oxidant that is produced is  $H_2O_2$  which rises from approximately 1ppb in the bulk water to 6ppb at the base of the deposit. The reason for this rise is the depletion in  $H_2$  as a result of partitioning into the steam phase exiting from the chimney of the deposit.

Figure 5-6 is a plot of the pH,  $[Li^+]$ ,  $[B(OH)_3]$  and the amount of  $LiBO_2(s)$  through the deposit for a deposit of thickness 59 $\mu$ m. Precipitation of  $LiBO_2(s)$  occurs between 35 and 40 $\mu$ m and at this point both the concentration of  $Li^+$  and  $B(OH)_3$  have reached a steady state of approximately  $1 \times 10^{-2}$  and 2M respectively. At a film thickness of 40 $\mu$ m the water temperature has risen to near the critical temperature and therefore evaporation has ceased beyond this point. This means below thick deposit the concentrating of species in solution has ceased, loss of boric acid to the vapor is halted and the concentrations of  $Li^+$  and  $B(OH)_3$  are simply those in equilibrium with  $LiBO_2(s)$ . The pH initially falls with depth but at approximately 30 $\mu$ m the  $Li^+$  concentrating starts to control the pH and it begins to rise. This pH rise with depth would continue until the location in the deposit where the critical temperature of water is obtained, and pH values of the order of 9 can be achieved if precipitation of  $LiBO_2(s)$  is absent from the model. Figure 5-6 indicates the precipitation of the lithium borate pulls the pH down and buffers it in the final third of the deposit at about 7.6.

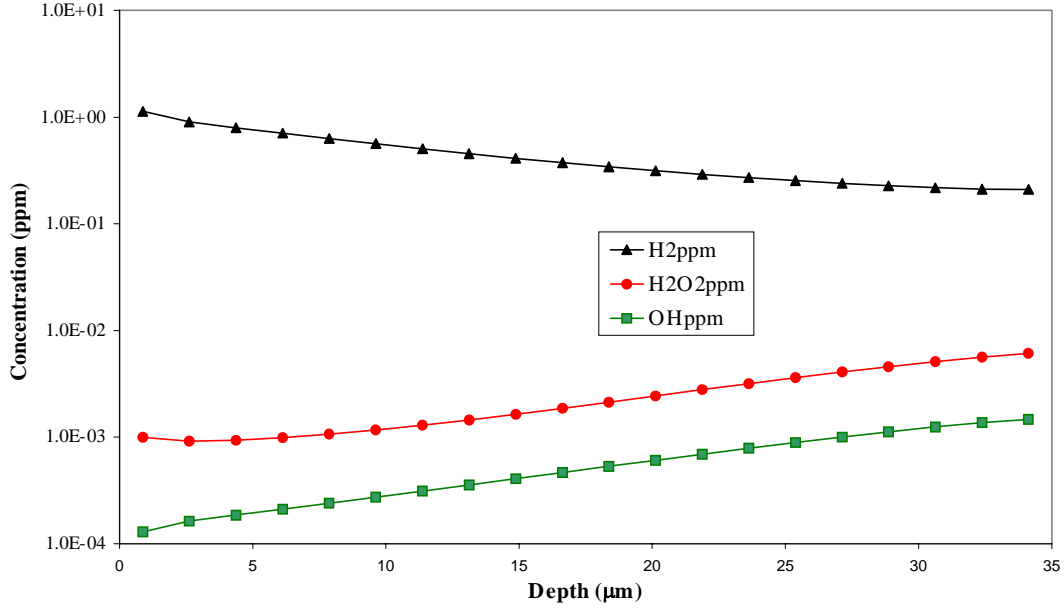
Figure 5-7 shows the temperature variation through the 59 $\mu$ m thick deposit. The critical temperature of water occurs at approximately 40 $\mu$ m and below this evaporative heat loss has ceased so heat is only lost by the less efficient method of conduction. The temperature therefore continues to rise and at the base of the deposit is in the region of 400°C.

Figure 5-8 plots the soluble Ni/Fe ratio through the 59 $\mu$ m thick deposit. The behavior of this ratio is controlled by the pH and up to a 40 $\mu$ m depth it lies above 0.5 (corresponding to congruent dissolution of  $NiFe_2O_4$ ). In the region of the deposit above 40 $\mu$ m where  $LiBO_2(s)$  precipitation has taken place, the pH is relatively constant and the temperature is high, this ratio falls below 0.5. A soluble Ni/Fe ratio below 0.5 may imply a solid phase rich in Nickel (compared to  $NiFe_2O_4$ ) and of course the reverse for a ratio above 0.5. However, as stated previously, such considerations should be left until a later date when the model is fully developed.

Figure 5-9 is a plot of  $H_2$  and the radiolysis species  $H_2O_2$  and OH through the depth of the deposit. The peroxide concentration rises to 17ppb as the  $H_2$  concentration falls from approximately 1ppm to 0.17ppm. In Figure 5-10 the peroxide concentration through the deposit is plotted against the hydrogen concentration through the deposit. Approaching the bottom of the deposit, as the hydrogen falls, the change in peroxide is dramatic, indicating that  $[H_2O_2]$  is very sensitive to  $[H_2]$  in this region.

In the following sections a number of the default operating conditions have been changed and the effect of this on the model predictions investigated.

Results From Crud Chemistry Model (CCM)



**Figure 5-5**  
 $H_2$ ,  $H_2O_2$  and OH against depth for a 35μm thick deposit. Calculation with 2ppm Li, 1200ppm B and 25cm<sup>3</sup> kg<sup>-1</sup> (STP) H<sub>2</sub>.

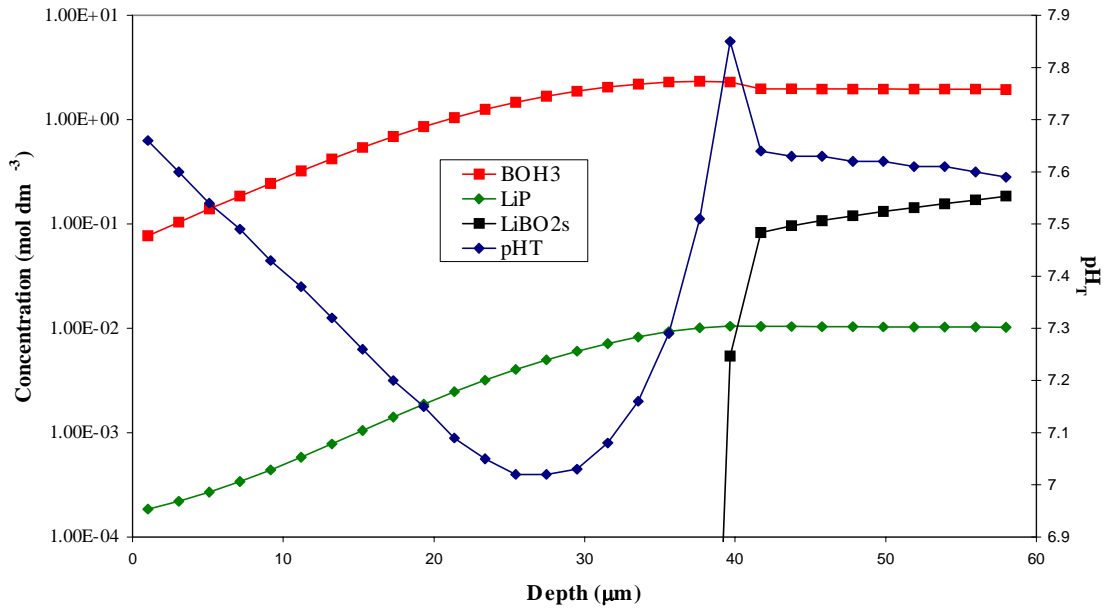


**Figure 5-6**  
 pH, Li<sup>+</sup>, Boric acid concentration and amount of LiBO<sub>2</sub>(s) against depth for a 59μm thick deposit. Calculation with 2ppm Li, 1200ppm B and 25cm<sup>3</sup> kg<sup>-1</sup> (STP) H<sub>2</sub>.

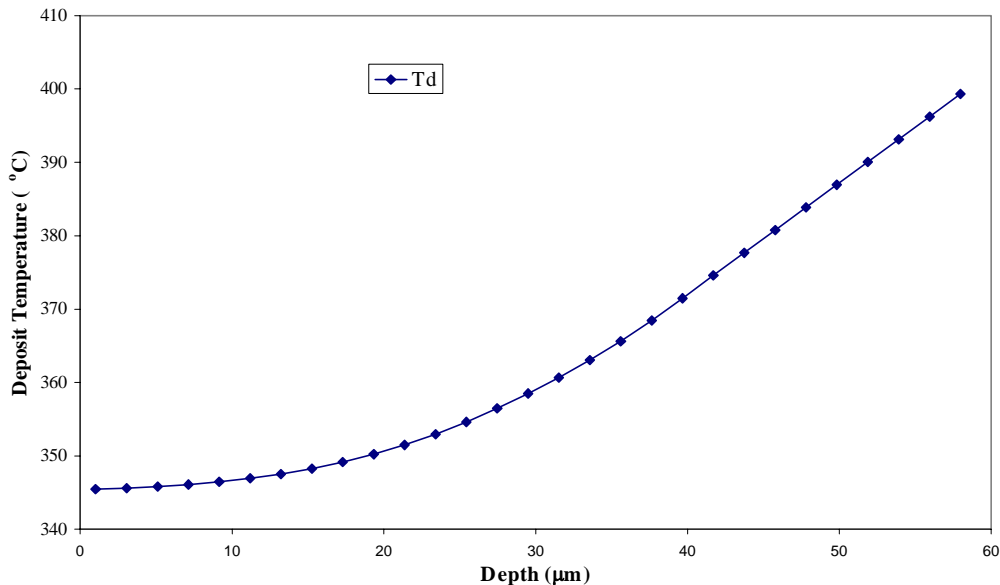


**Figure 5-7**  
 Deposit temperature against depth for a 59µm thick deposit. Calculation with 2ppm Li, 1200ppm B and 25cm<sup>3</sup> kg<sup>-1</sup> (STP) H<sub>2</sub>.

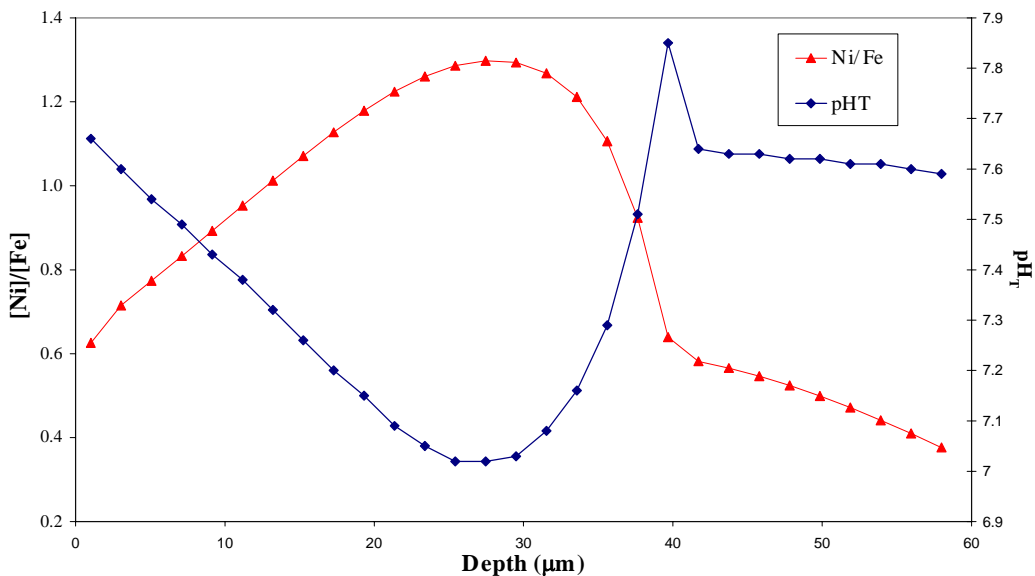


**Figure 5-8**  
 Soluble Ni/Fe ratio against depth for a 35µm thick deposit. Calculation with 2ppm Li, 1200ppm B and 25cm<sup>3</sup> kg<sup>-1</sup> (STP) H<sub>2</sub>.

Results From Crud Chemistry Model (CCM)

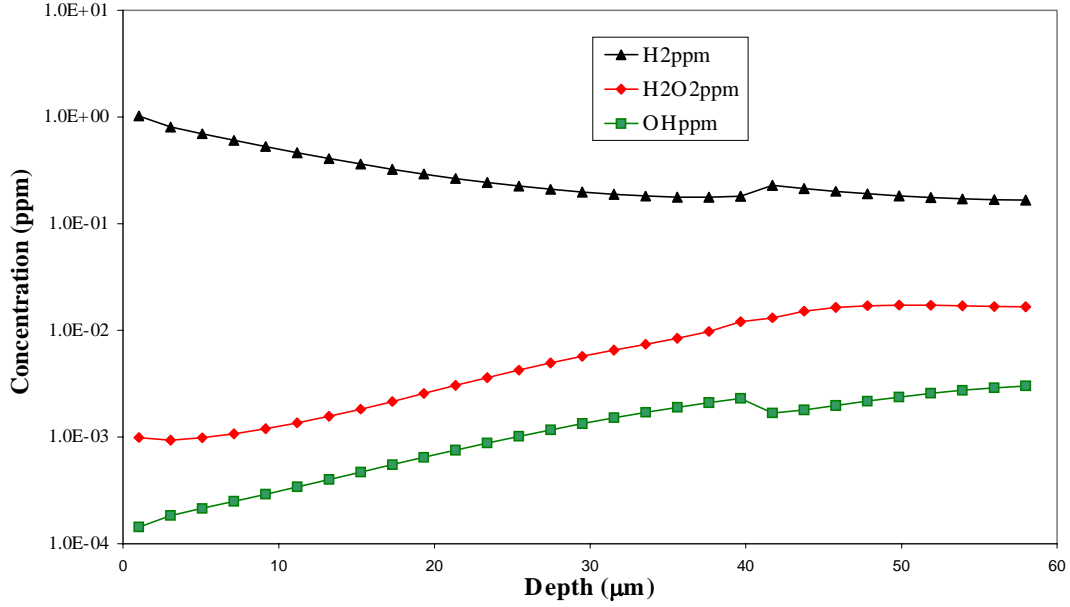


**Figure 5-9**  
 $H_2$ ,  $H_2O_2$  and OH against depth for a 59 μm thick deposit. Calculation with 2ppm Li, 1200ppm B and  $25cm^3 kg^{-1}$  (STP)  $H_2$ .

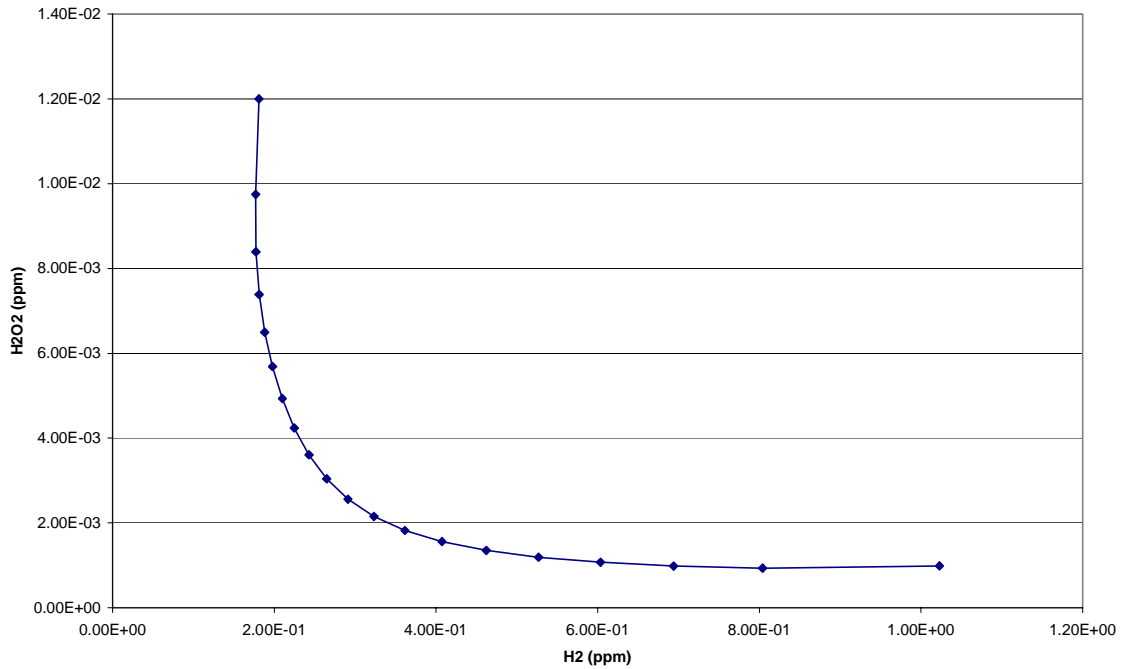


**Figure 5-10**  
 $H_2O_2$  plotted against  $H_2$  through part of the 59 μm thick deposit. Calculation with 2ppm Li, 1200ppm B and  $25cm^3 kg^{-1}$  (STP)  $H_2$ .

## 5.2 Lithium

Calculations were carried out for lithium concentrations of 1, 2 and 3ppm all other parameters being the same as in Table 5-1.

Figure 5-11 is a plot of the temperature at the base of the deposit for different thickness of crud for the three lithium concentrations. Figure 5-11 indicates the bulk lithium concentration has little effect on the deposit temperature.

Figure 5-12 plots the amount of  $\text{LiBO}_2(\text{s})$  at the base of the deposit for different crud thickness for the three lithium concentrations. Precipitation of the solid starts at approximately  $35\mu\text{m}$  for all three lithium concentrations. The amount of precipitate generated during the time of integration changes with lithium, in fact it appears that more precipitate is generated the smaller the amount of bulk lithium. The absolute amounts of the solid at the bottom of the deposit are a function of the integration time for the calculation and how much precipitate has been generated before reaching the crud base. Therefore, the absolute amounts of  $\text{LiBO}_2(\text{s})$ , as stated above, don't provide very useful data.

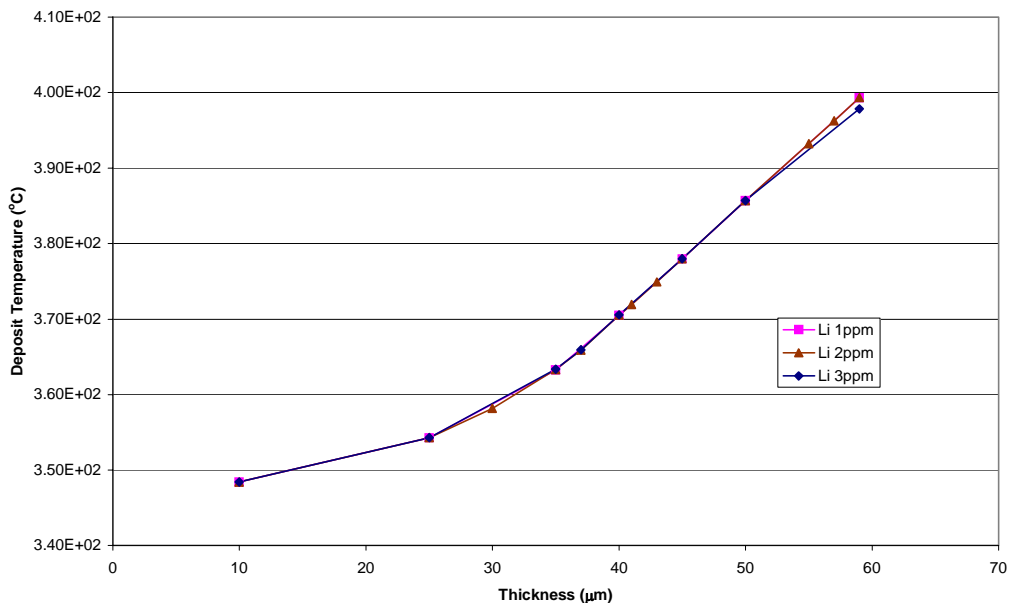
Figure 5-13 is a plot of the pH at the base of deposit against deposit thickness for the three lithium concentrations. For a thin crud film ( $10\mu\text{m}$ ) the pH at the base for 3ppm Li is approximately 7.9, for 2ppm Li it is 7.7 and for 1ppm Li it is 7.5 and this is what would be expected. For a crud of thickness near  $60\mu\text{m}$ , the pH for the 3ppm Li is 7.5, for 2ppm Li it is 7.6 and for 1ppm Li it is 7.75. In other words the order of the pH is the reverse of what it is in the bulk water and for thin deposits. The pH in this system is a complex function of initial boundary conditions, Li and B transport, temperature and the  $\text{LiBO}_2(\text{s})$  equilibrium. This is apparent from the way the pH shifts around for any particular lithium value as the crud thickness changes.

Figure 5-14 plots the total soluble boron at the base of the deposit against deposit thickness for the three lithium concentrations. The boron concentration rises with film thickness up to a crud thickness of 35 to  $40\mu\text{m}$  when it steadies out at approximately 4.3M. The calculated behavior is independent of the bulk lithium concentration. Of the 4.3M boron approximately 2M is boric acid, with 0.7M of the boron tri-mer  $\text{B}_3\text{O}_3(\text{OH})_3$  and the remaining B consisting of the poly-anions. The high concentration of  $\text{B}_3\text{O}_3(\text{OH})_3$  arises from its increased thermodynamic stability with increasing temperature, which is some what contrary to what might be expected intuitively.

Figure 5-15 shows the concentration of the main radiolysis oxidizing species  $\text{H}_2\text{O}_2$  at the base of the deposit against deposit thickness for the three lithium concentrations. Changing the lithium concentration has little effect on the calculated amount of  $\text{H}_2\text{O}_2$ , at approximately  $60\mu\text{m}$  crud thickness between 16 and 17ppb of peroxide is calculated at the base of the deposit for all three lithium concentrations.

In general the effect of bulk lithium concentration on the calculated chemical and physical properties within the crud is negligible.

Results From Crud Chemistry Model (CCM)



**Figure 5-11**  
 Temperature at the bottom of the deposit against crud thickness for initial Li concentrations of 1, 2 and 3ppm.

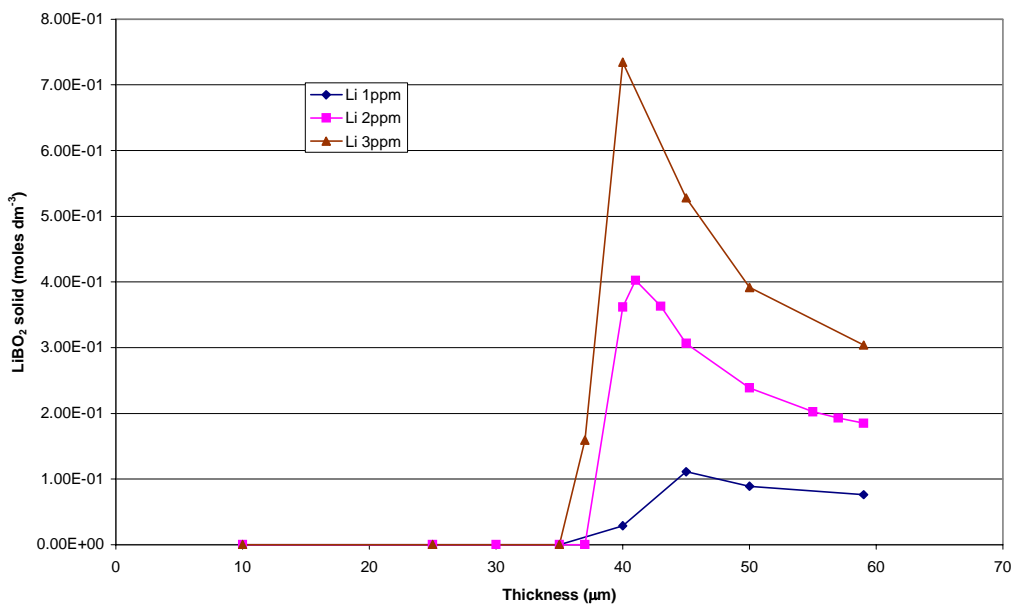


**Figure 5-12**  
 Amount of LiBO<sub>2</sub>(s) at the bottom of the deposit against crud thickness for initial Li concentrations of 1, 2 and 3ppm.

Results From Crud Chemistry Model (CCM)

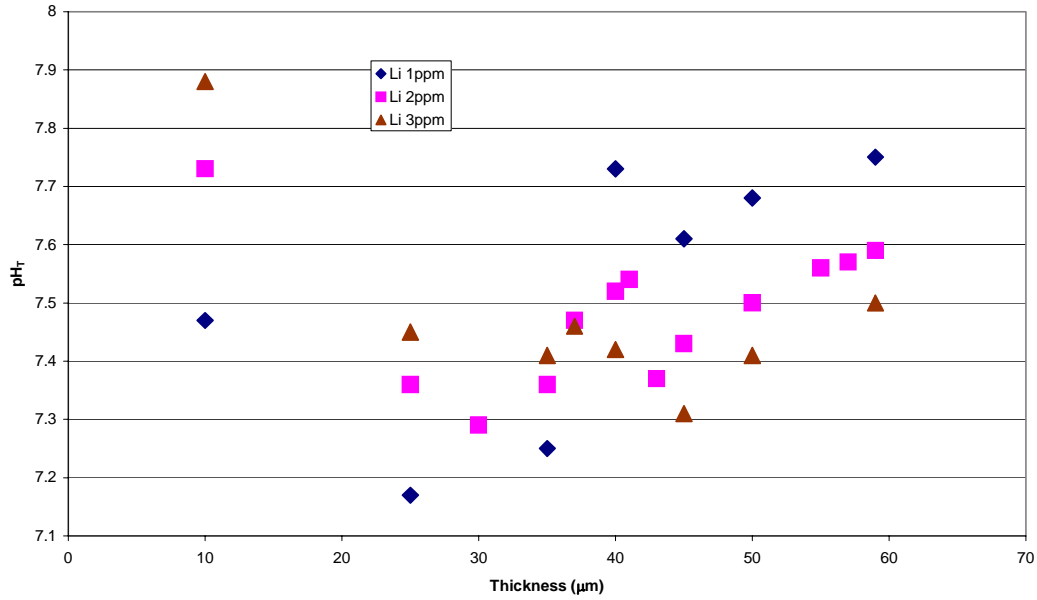


**Figure 5-13**  
pH at the bottom of the deposit against crud thickness for initial Li concentrations of 1, 2 and 3ppm.

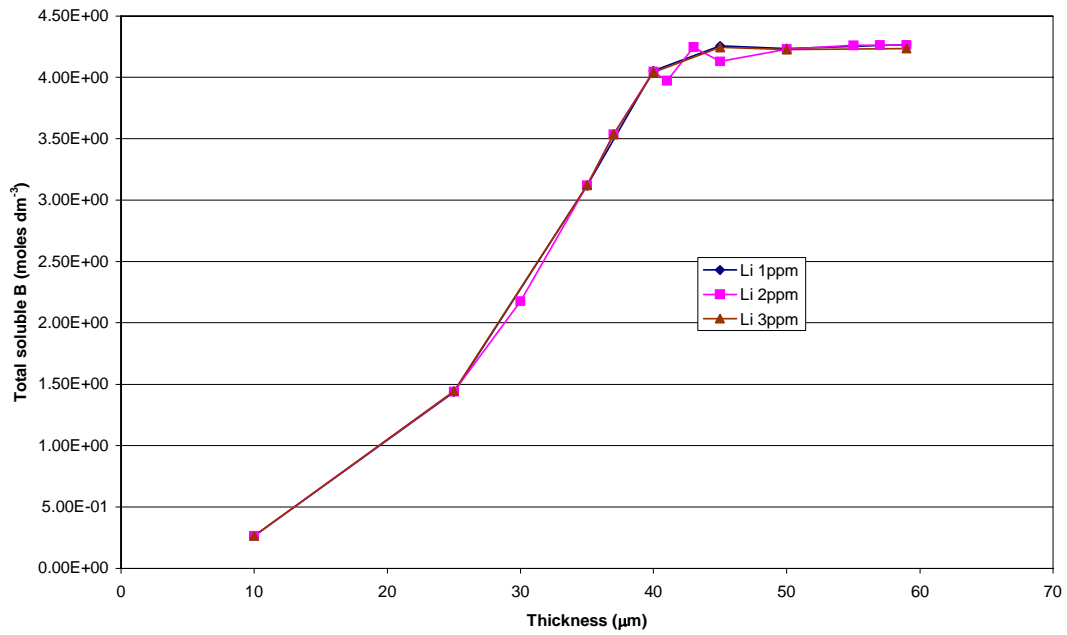


**Figure 5-14**  
Total soluble boron at the bottom of the deposit against crud thickness for initial Li concentrations of 1, 2 and 3ppm.

## Results From Crud Chemistry Model (CCM)

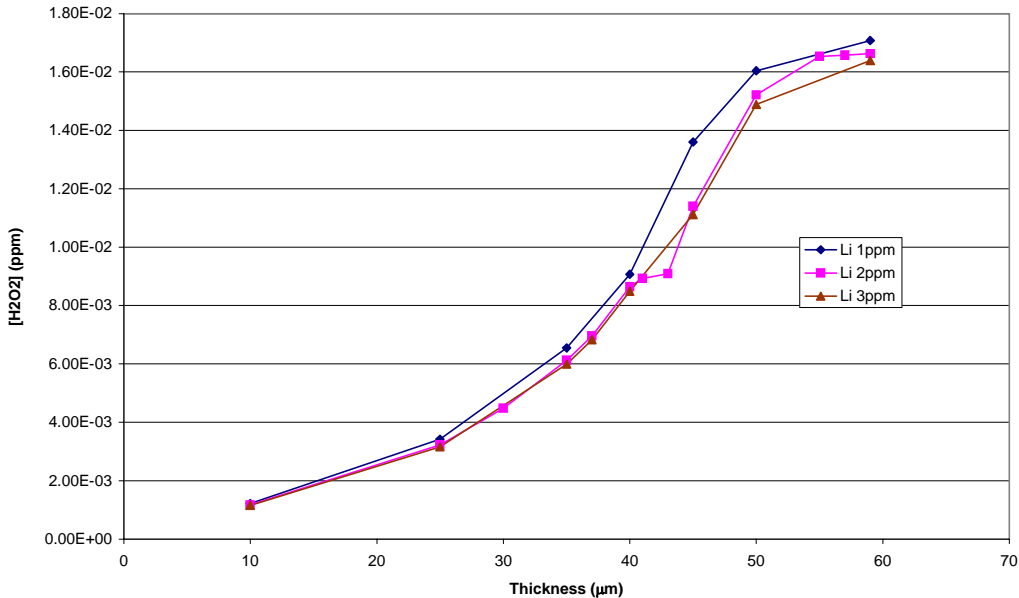


**Figure 5-15**  
**H<sub>2</sub>O<sub>2</sub> concentration at the bottom of the deposit against crud thickness for initial Li concentrations of 1, 2 and 3ppm.**

### 5.3 Boron

Calculations have been carried out for four bulk water boron concentrations of 300, 600, 1200 and 1800ppm. The results of these calculations are presented here.

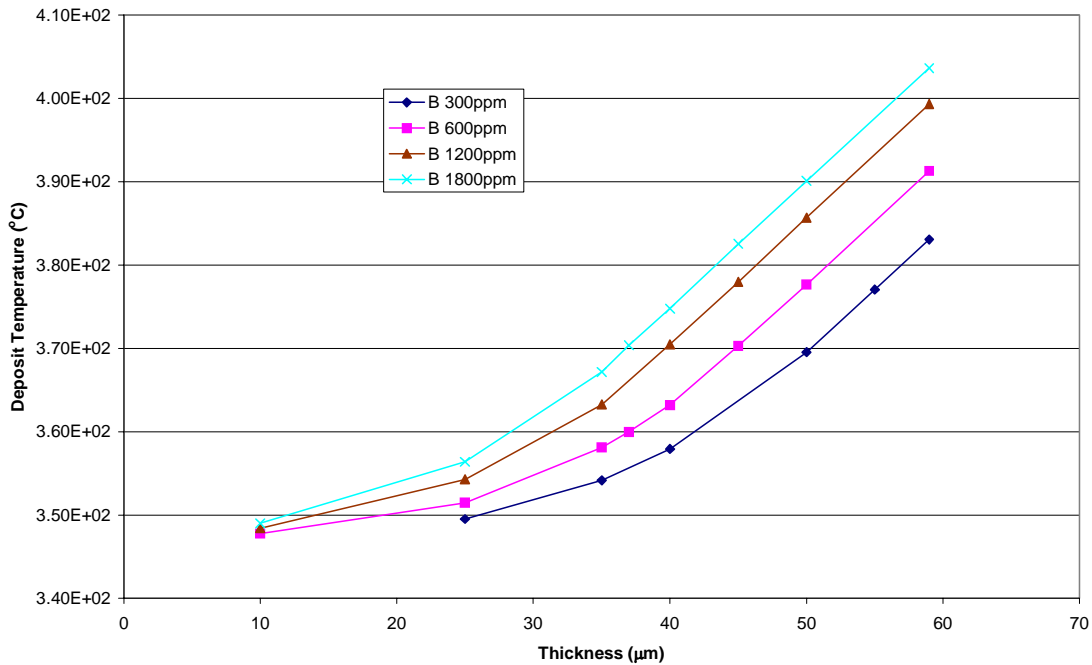
Figure 5-16 is a plot of deposit temperature at the base of the crud as a function of crud thickness. The lower the boron concentration the lower the temperature of the deposit, so at approximately 60μm crud thickness, the temperatures are 404 (1800ppm B), 399 (1200ppm B), 391 (600ppm B) and 383 °C (300ppm B). This is simply due to the fact that the lower boron concentration in the bulk water, the lower the concentration within the deposit for a given crud thickness and therefore the lower the boiling point elevation. This will mean at low boron concentrations evaporative heat loss will take place over a greater fraction of the crud depth.

Figure 5-17 shows the amount of LiBO<sub>2</sub>(s) against crud thickness. For all four boron concentrations considered this solid precipitates out at between 35 and 40μm.

Figure 5-18 is a plot of pH at the base of the deposit against crud thickness. For thin cruds the behavior of the pH is as expected, the solution being more acidic with increasing boron concentration. For thick crud the situation is not so obvious, with the 300 ppm B solution having a lower pH at the base of the deposit than the 1800ppm B solution (although the variation is small, less than 0.2 pH units).

Figure 5-19 plots the concentration of peroxide at the base of the deposit against crud thickness. The concentration of boron used in the calculation has quite a dramatic effect on the amount of

peroxide calculated. At 1200 and 1800ppm B the peroxide concentration at the base of the 60 $\mu$ m deposit is approximately 16 to 17ppb. Decreasing the boron to 600ppm causes the peroxide to rise rapidly to 350ppb and decreasing the boron further to 300ppm causes the peroxide to fall to approximately 100ppb. The reason for this behavior can be understood by appreciating what controls the peroxide concentration in the model. Increasing the boron concentration increases the alpha particle dose rate in the model and since alpha particles give high yields of molecular products such as H<sub>2</sub>O<sub>2</sub> it would be expected that this would increase the peroxide concentration. However, it is clear from Figure 5-10, discussed earlier, that the peroxide concentration is very sensitive to the hydrogen concentration in thick deposits. In the case of a 300ppm B solution, for thick deposit, less of the crud will be above the critical temperature of water than for say the 1800ppm B solution. What this means is that evaporative heat loss will be taking place into the wick chimney over a longer region for the 300ppm B than for the 1800ppm B case. Therefore partitioning of H<sub>2</sub> into the steam phase will occur more in the 300ppm case compared to higher boron concentrations. Generally speaking then there will be less hydrogen in the liquid phase in the crud the lower the boron concentration. This is shown to be the case in Figure 5-20 which plots the H<sub>2</sub> concentration through the 60 $\mu$ m deposit for each of the four boron concentrations. Therefore we have two opposing effects of decreasing boron; On the one hand it lowers the alpha dose and therefore decreases the peroxide yield, but on the other hand it lowers the hydrogen concentrations within the deposit, increasing the peroxide concentration. Which of these processes dominate determines whether significant peroxide is produced.



**Figure 5-16**  
**Temperature at bottom of deposit against crud thickness for initial boron concentrations of 300, 600, 1200 and 1800 ppm.**

Results From Crud Chemistry Model (CCM)

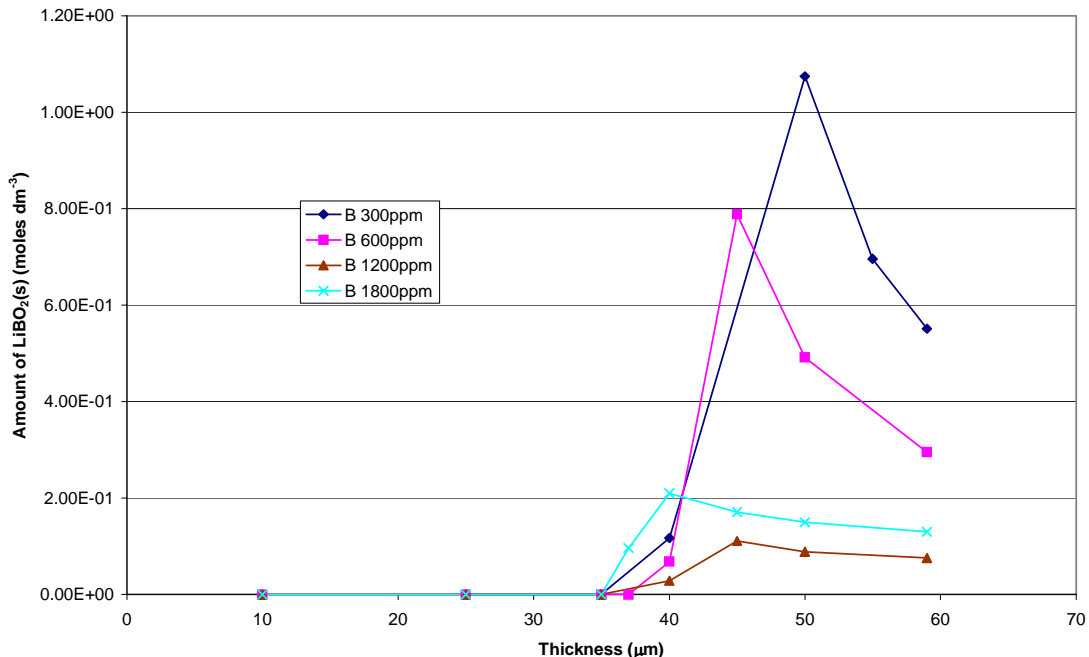


**Figure 5-17**  
Amount of  $\text{LiBO}_2(\text{s})$  at the bottom of deposit against crud thickness for initial boron concentrations of 300, 600, 1200 and 1800 ppm.

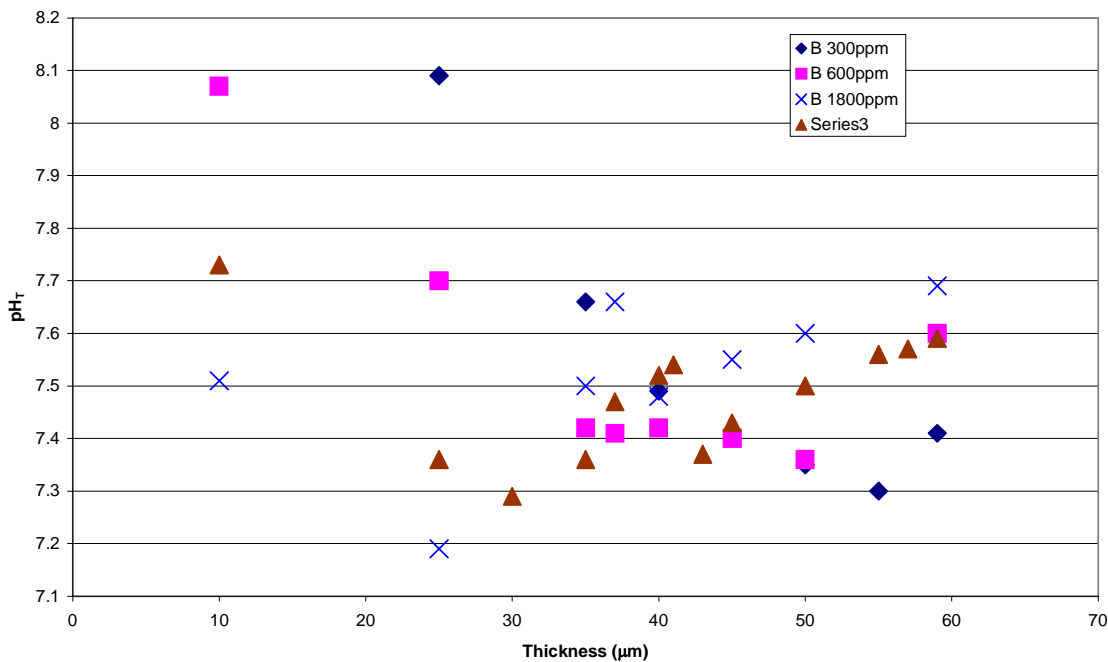


**Figure 5-18**  
pH at the bottom of deposit against crud thickness for initial boron concentrations of 300, 600, 1200 and 1800 ppm.

Results From Crud Chemistry Model (CCM)

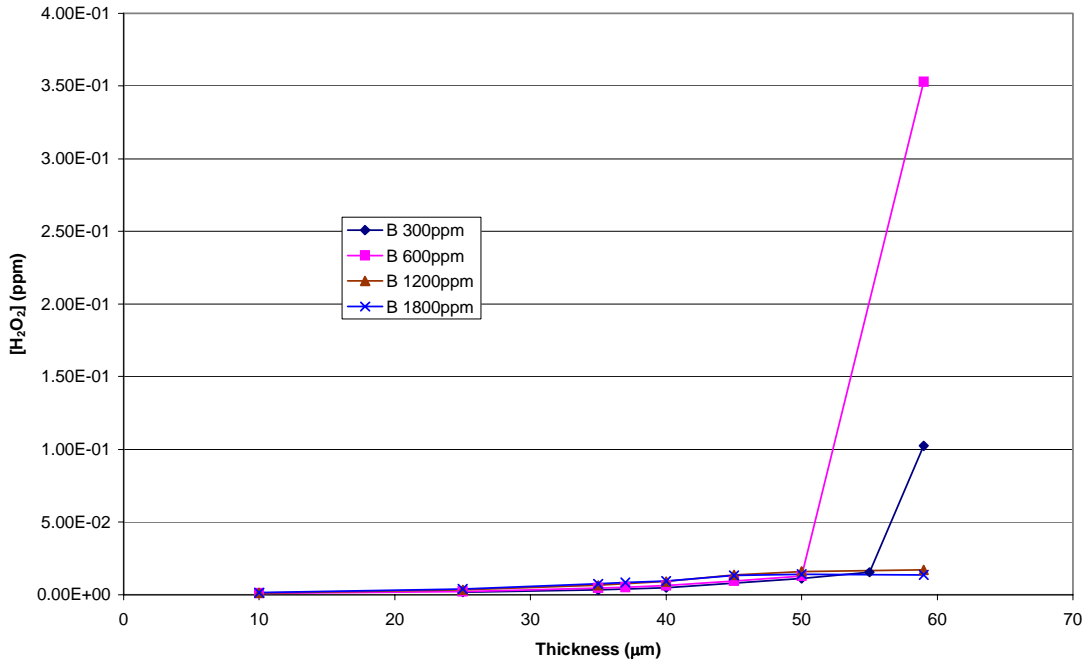


**Figure 5-19**  
 Concentration of H<sub>2</sub>O<sub>2</sub> at the bottom of deposit against crud thickness for initial boron concentrations of 300, 600, 1200 and 1800 ppm.

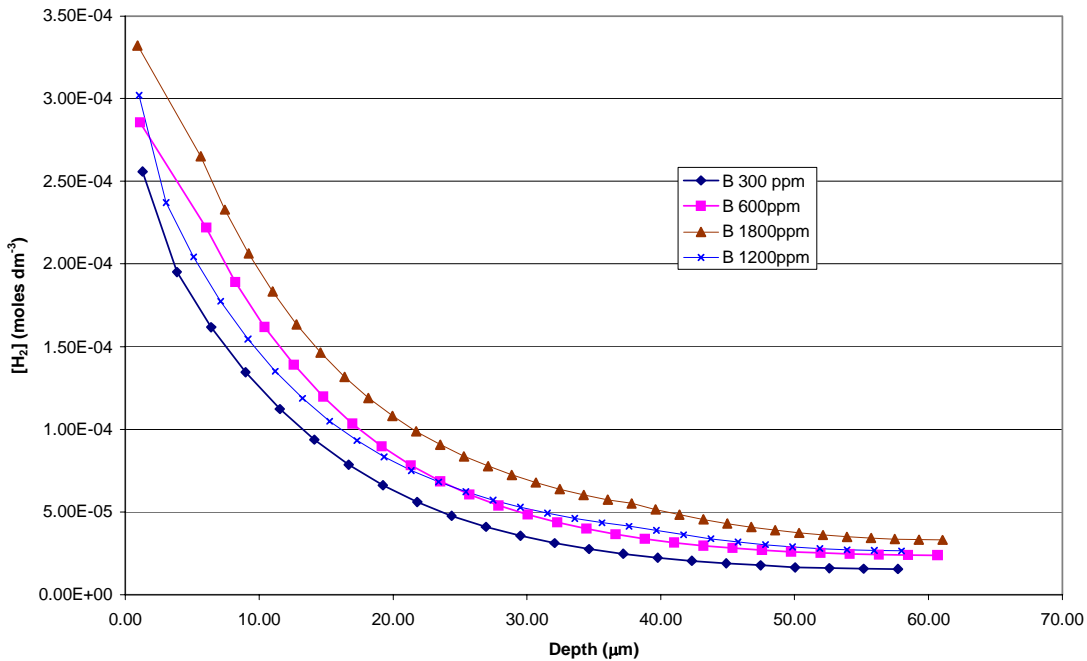


**Figure 5-20**  
 Concentration of H<sub>2</sub> through an approximate 60μm deposit for initial boron concentrations of 300, 600, 1200 and 1800 ppm.

## Results From Crud Chemistry Model (CCM)

### 5.4 Hydrogen

The only parameter in the model that will be affected by changes in hydrogen concentration will be the levels of peroxide with the deposit. Figure 5-21 is a plot of peroxide concentration at the bottom of the deposit as a function of crud thickness for bulk water hydrogen concentrations of 5, 10, 25 and 50  $\text{cm}^3 \text{kg}^{-1}$  (STP). For deposits up to 35  $\mu\text{m}$  thickness the level of hydrogen in the system has little effect on the peroxide levels in the crud. However, as the crud thickness increases the hydrogen level becomes more important and at 60  $\mu\text{m}$  it can have a dramatic effect, changing the peroxide concentration from 16ppb at 25  $\text{cm}^3 \text{kg}^{-1}$  (STP) to almost 850ppb at 5  $\text{cm}^3 \text{kg}^{-1}$  (STP). This level of peroxide is similar to what would be expected for the core of a BWR reactor running with no added hydrogen. However the solution here is probably more corrosive than in a BWR because the system is at a much higher temperature (400°C compared to 290°C).

### 5.5 Heat Flux

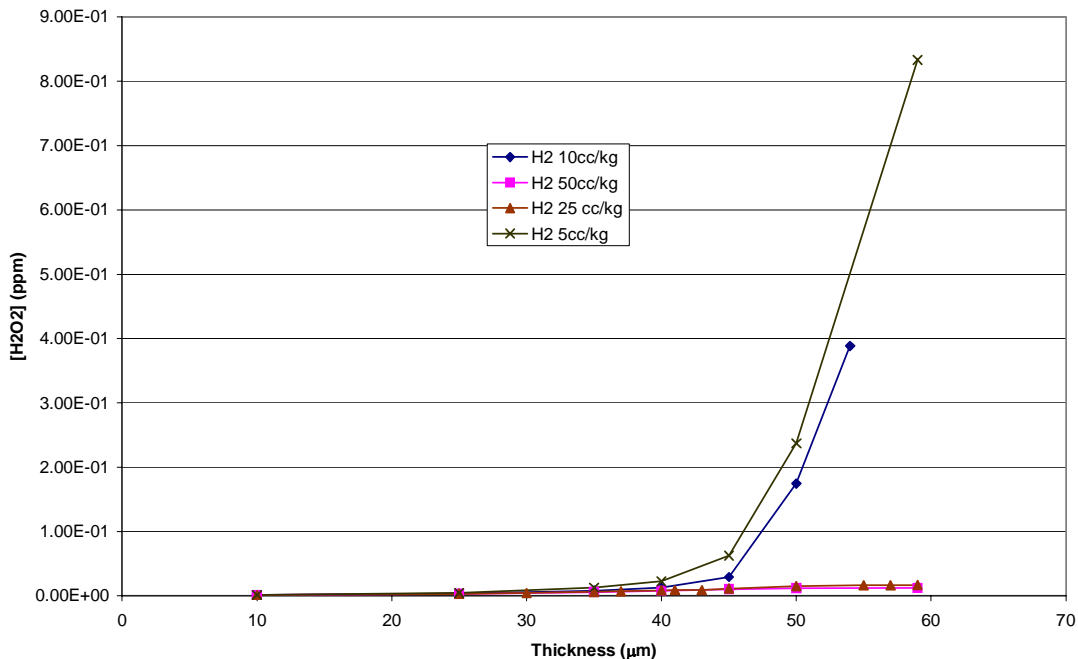
Calculations have been carried for the standard input conditions using heat fluxes of 0.1, 0.5, 0.75 and  $1\text{MWm}^{-2}$ . Figure 5-22 plots the deposit temperature at the base of the deposit against crud thickness for the four different heat fluxes. At a heat flux of  $0.1\text{MWm}^{-2}$  the temperature at the base of the deposit is relatively constant with increasing crud thickness. This is not the case at the higher heat fluxes with the temperature at the bottom of the deposit rising above the critical temperature of water for a crud thickness of approximately 80  $\mu\text{m}$  at  $0.5\text{Wm}^{-2}$ , 55  $\mu\text{m}$  at  $0.75\text{Wm}^{-2}$  and 40  $\mu\text{m}$  at  $1\text{MWm}^{-2}$ .

Figure 5-23 is a plot of the amount of  $\text{LiBO}_2(\text{s})$  against crud thickness for the four different heat fluxes. At a heat flux of  $0.1\text{MWm}^{-2}$  the solid phase does not precipitate out, at  $0.5\text{MWm}^{-2}$  it precipitates out at 70  $\mu\text{m}$ , at  $0.75\text{MWm}^{-2}$  it precipitates at 50  $\mu\text{m}$  and at  $1\text{MWm}^{-2}$  it is 40  $\mu\text{m}$ . The relative importance of the heat flux on the deposit temperature and the point of precipitation are not surprising. Consideration of the analytic solution to this problem discussed in Section 4.1.4 indicates that the concentration factors are an exponential function of heat flux, and the degree of concentration is fundamental in raising the temperature of the system and determining the point of precipitation.

Figure 5-24 shows how the concentration of soluble boron at the base of the deposit changes with increasing crud thickness. For all cases the maximum concentration achieved for soluble boron is in the region of 4.3M, however this is achieved for a crud thickness of 40  $\mu\text{m}$  for the  $1\text{MWm}^{-2}$  heat flux, at 60  $\mu\text{m}$  (heat flux  $0.75\text{MWm}^{-2}$ ), 80  $\mu\text{m}$  (heat flux  $0.5\text{MWm}^{-2}$ ) and is never achieved for a heat flux of  $0.1\text{MWm}^{-2}$ .

The effect of heat flux on the concentration of peroxide in the base of the deposit is shown in Figure 5-25. Typical maximum values achieved are in the range 14 to 20ppb, with less than 2pb been generated for a heat flux of  $0.1\text{MWm}^{-2}$ . At what crud thickness this concentration of peroxide is achieved is determined by the heat flux, decreasing with increasing heat flux.

Results From Crud Chemistry Model (CCM)



**Figure 5-21**  
 Concentration of H<sub>2</sub>O<sub>2</sub> at the bottom of deposit against crud thickness for initial H<sub>2</sub> concentrations of 5, 10, 25 and 50 cm<sup>3</sup>kg<sup>-1</sup>(STP).

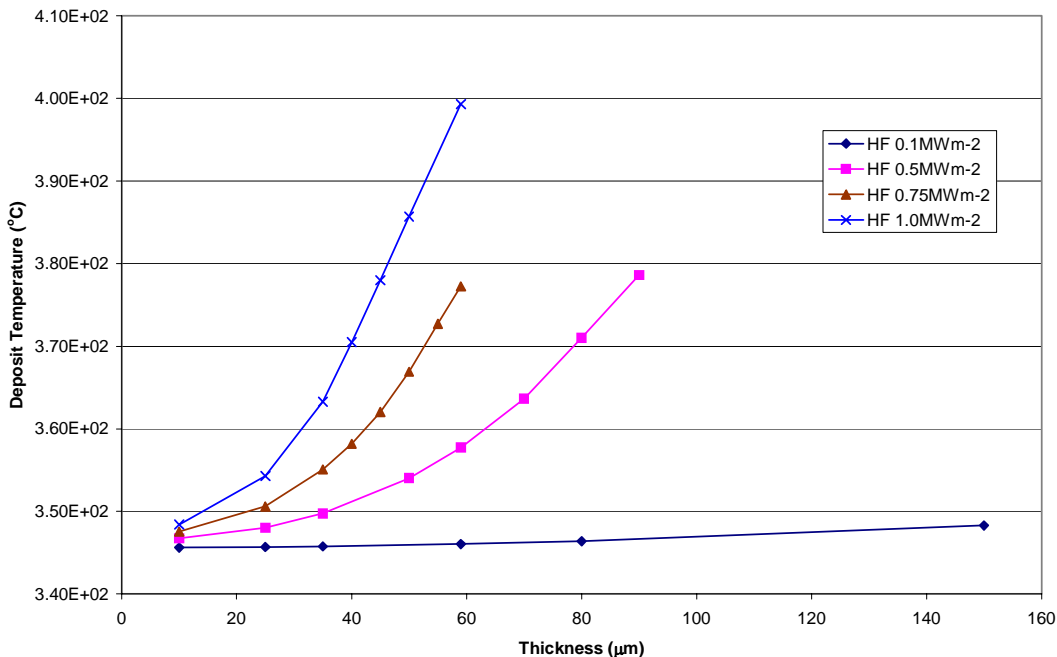


**Figure 5-22**  
 Temperature at the bottom of deposit against crud thickness for initial heat fluxes (HF) of 0.1, 0.5, 0.75 and 1MWm<sup>-2</sup>.

Results From Crud Chemistry Model (CCM)

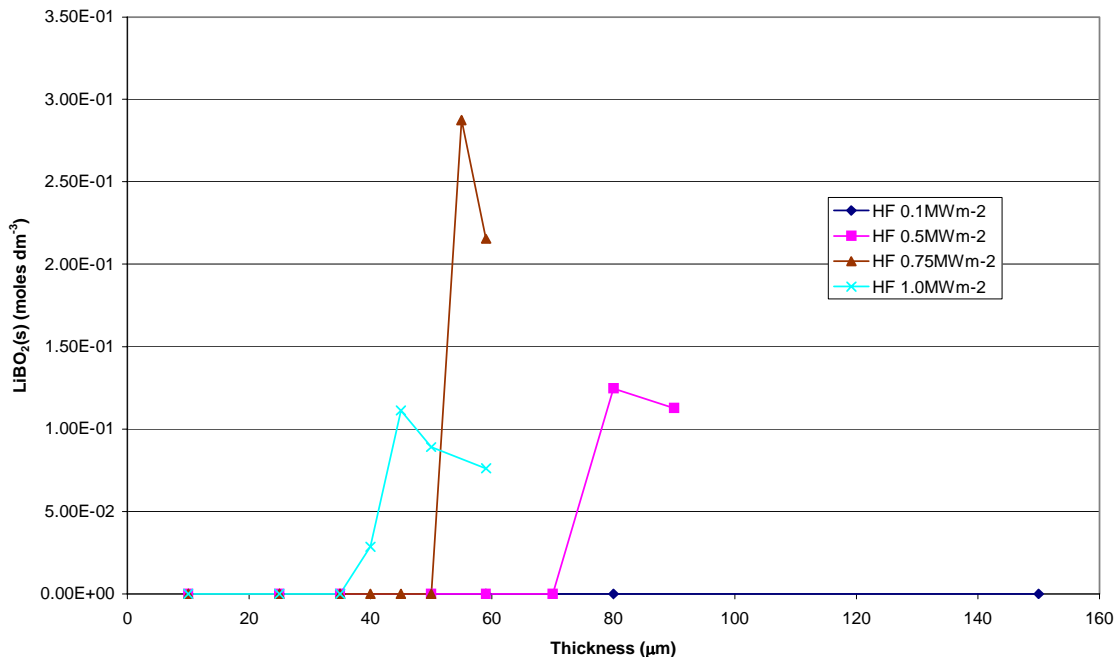


**Figure 5-23**  
Amount of  $\text{LiBO}_2(\text{s})$  at the bottom of deposit against crud thickness for initial heat fluxes (HF) of 0.1, 0.5, 0.75 and  $1\text{MWm}^{-2}$ .

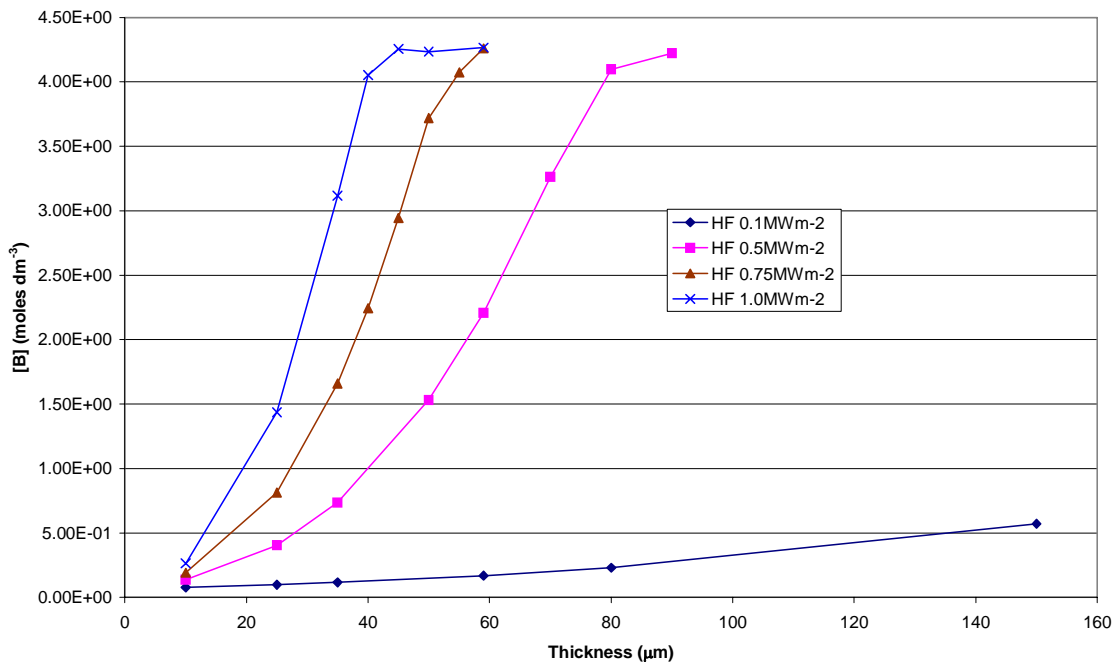


**Figure 5-24**  
Concentration of soluble boron at the bottom of deposit against crud thickness for initial heat fluxes (HF) of 0.1, 0.5, 0.75 and  $1\text{MWm}^{-2}$ .

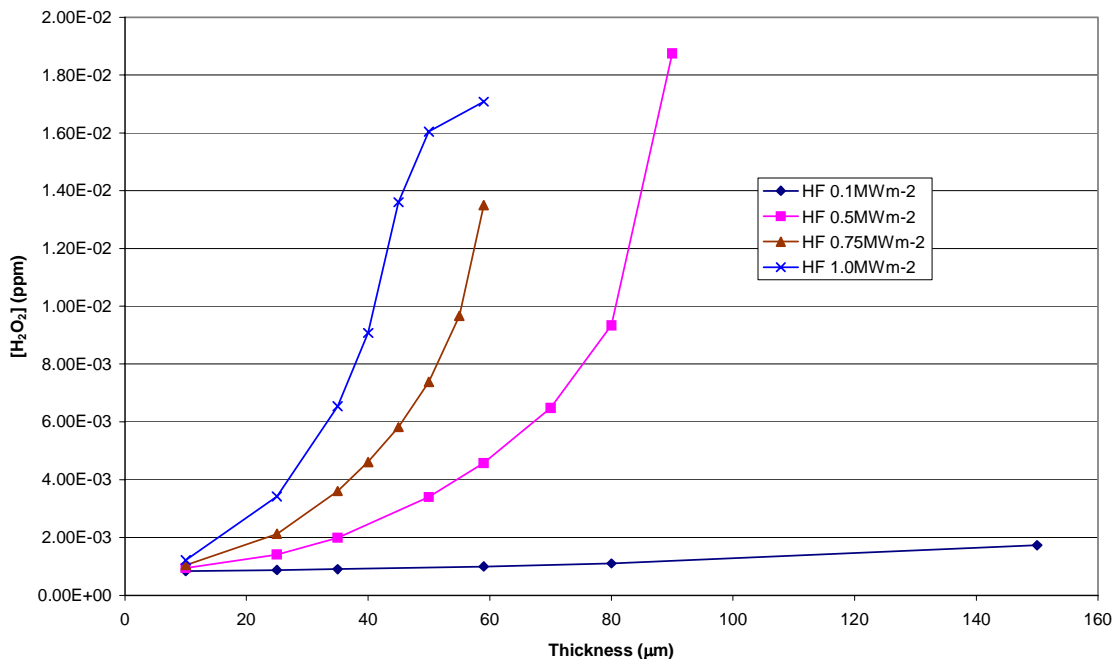


**Figure 5-25**  
**Concentration of H<sub>2</sub>O<sub>2</sub> at the bottom of deposit against crud thickness for initial heat fluxes (HF) of 0.1, 0.5, 0.75 and 1 MWm<sup>-2</sup>.**

## 5.6 Neutron Flux

The neutron flux used for all the calculations presented so far is  $3.6 \times 10^{14} \text{ cm}^{-2} \text{ s}^{-1}$ , which is an average value for the core region. This value is close to values calculated by Chapman for typical AOA plants, discussed in Appendix B. Close to the fuel surface and for highly rated pins it is likely that the flux will be larger than this value. To examine the sensitivity of the model results to this parameter calculations have been carried out for a flux of  $7.2 \times 10^{14} \text{ cm}^{-2} \text{ s}^{-1}$ . Increasing the neutron flux will increase the alpha dose rate and therefore the level of peroxide in the system. Figure 5-26 is a plot of H<sub>2</sub> and H<sub>2</sub>O<sub>2</sub> through a 35 μm deposit for both neutron fluxes (the calculation uses standard conditions, Table 2-1). Although there is an increase in peroxide concentration at the higher flux the effect is small. Figure 5-27 is the equivalent plot for a crud of thickness near 60 μm, the increase in peroxide calculated here is dramatic. Towards the base of the deposit using a neutron flux of  $3.6 \times 10^{14} \text{ cm}^{-2} \text{ s}^{-1}$  the model predicted a peroxide concentration of the order of 15 to 20 ppb. At the higher flux of  $7.2 \times 10^{14} \text{ cm}^{-2} \text{ s}^{-1}$  the calculated peroxide concentration in this region is 4 ppm. Clearly the hydrogen concentration at the base of the crud that was adequate to suppress radiolysis at the lower neutron flux is not adequate at the higher flux. Decomposition of peroxide on surfaces and oxidation of Fe<sup>2+</sup> will mean such large concentrations could not be achieved in practice, but what this calculation indicates is that the system may go extremely oxidizing at sufficiently high neutron fluxes.

Results From Crud Chemistry Model (CCM)

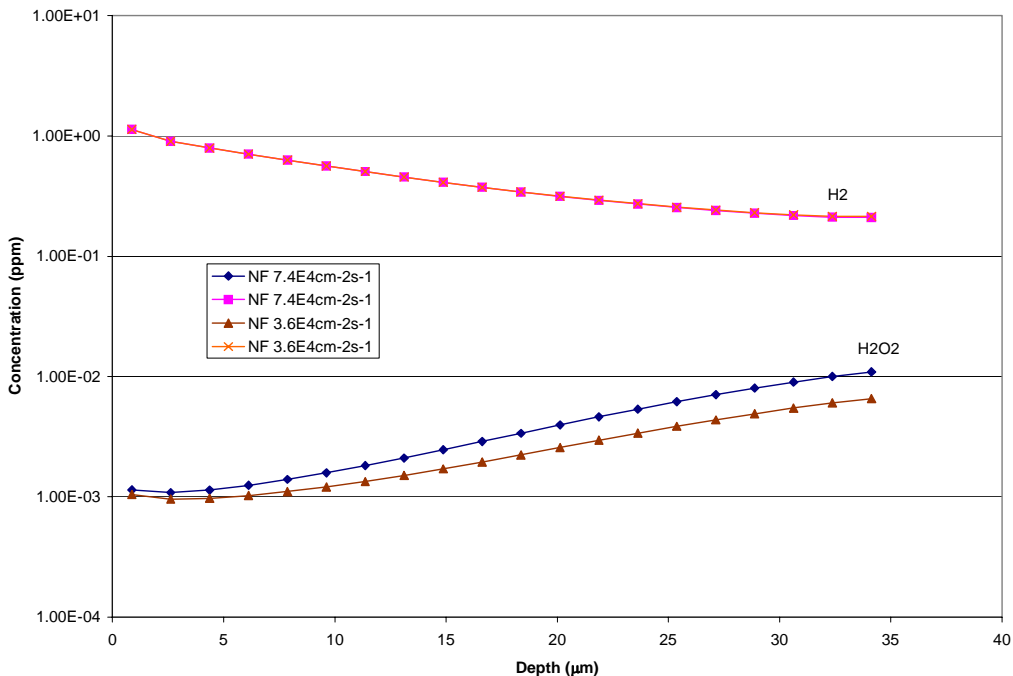


**Figure 5-26**  
 Concentration of H<sub>2</sub>O<sub>2</sub> against depth for a 35µm deposit. Calculations for two neutron fluxes (NF)  $3.6 \times 10^{14}$  and  $7.2 \times 10^{14} \text{ cm}^{-2} \text{ s}^{-1}$ .

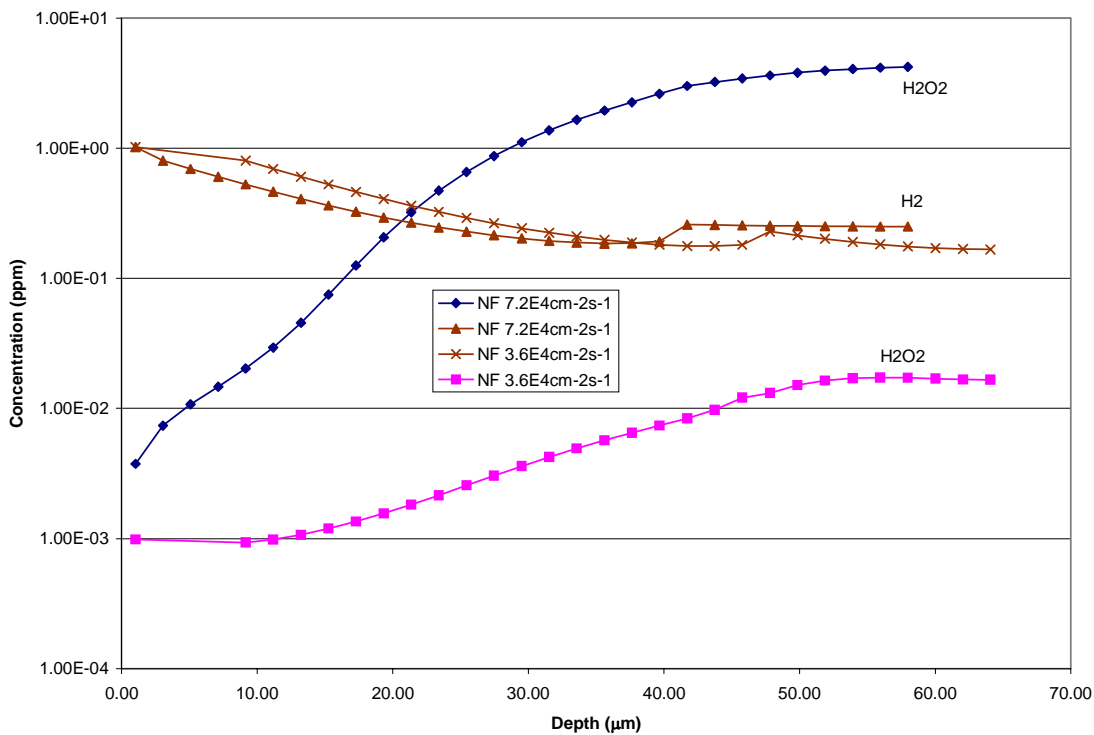


**Figure 5-27**  
 Concentration of H<sub>2</sub>O<sub>2</sub> against depth for a 59µm deposit. Calculations for two neutron fluxes (NF)  $3.6 \times 10^{14}$  and  $7.2 \times 10^{14} \text{ cm}^{-2} \text{ s}^{-1}$ .

## 5.7 Calculations under plant conditions

Westinghouse provided typical plant operating conditions for three plants; Diablo Canyon Unit 1 Cycle 11, V C Summer Cycle 12 and Vogtle 2 Cycle 9. The report discussing these conditions is given in Appendix B and the initial conditions used to model these plants are given in Table 5-2.

**Table 5-2**  
**Input conditions for plant calculations**

	Vogtle 2 Cycle 9	V C Summer Cycle 12	Diablo Canyon Unit 1 Cycle 11
Parameter	Value	Value	Value
Coolant temperature/°C	345.4	345.4	345.4
System pressure/atm	153.42	153.42	153.42
Chimney density/mm <sup>2</sup>	3000	3000	3000
Chimney radius/μm	2.5	2.5	2.5
Porosity	0.8	0.8	0.8
Tortuosity	2.5	2.5	2.5
Deposit depth/μm	25-60	25-60	25-60
Heat flux W/m <sup>2</sup>	8.2x10 <sup>5</sup>	8.7x10 <sup>5</sup>	8.1x10 <sup>5</sup>
Li/ppm	2	2	2
B/ppm	1200	1200	1200
H <sub>2</sub> /cc (STP) kg <sup>-1</sup>	25.3	25.3	25.3
γ Dose rate/Mrad h <sup>-1</sup>	580	785	650
n Dose rate/Mrad h <sup>-1</sup>	4500	5400	4600
n Flux/cm <sup>2</sup> s <sup>-1</sup>	4.0x10 <sup>14</sup>	4.1x10 <sup>14</sup>	3.8x10 <sup>14</sup>

Figures 5-28, 5-29 and 5-30 present the results of the calculations for Vogtle 2. Figure 5-28 is a plot of boric acid concentration, Li<sup>+</sup> concentration, pH and amount of LiBO<sub>2</sub>(s) against depth for a 59μm deposit. Figure 5-29 is a plot of deposit temperature and Figure 5-30 a plot of radiolysis species concentrations, both for a 59μm deposit thickness. All these plots look similar to those generated for the Standard operating conditions discussed earlier. The temperature at the bottom of the crud is lower than for the standard conditions, 385°C compared to 403°C and the point at which LiBO<sub>2</sub>(s) precipitation occurs is larger 45 – 50μm, compared to 35 to 40μm. Both these results are what is expected given the lower heat flux of 0.82MWm<sup>-2</sup> used for the Vogtle 2 calculations. Figures 5-31, 5-32 and 5-33 present the equivalent results for V C Summer and Figures 5-34, 5-35 and 5-36 are the plots for Diablo Canyon Unit 1. Both the VC Summer plots and Diablo Canyon results are very similar to Vogtle 2, the slightly lower depth of crud required to precipitate LiBO<sub>2</sub>(s) in the case of VC Summer being due to the slightly higher heat flux of 0.87MWm<sup>-2</sup>.

Results From Crud Chemistry Model (CCM)

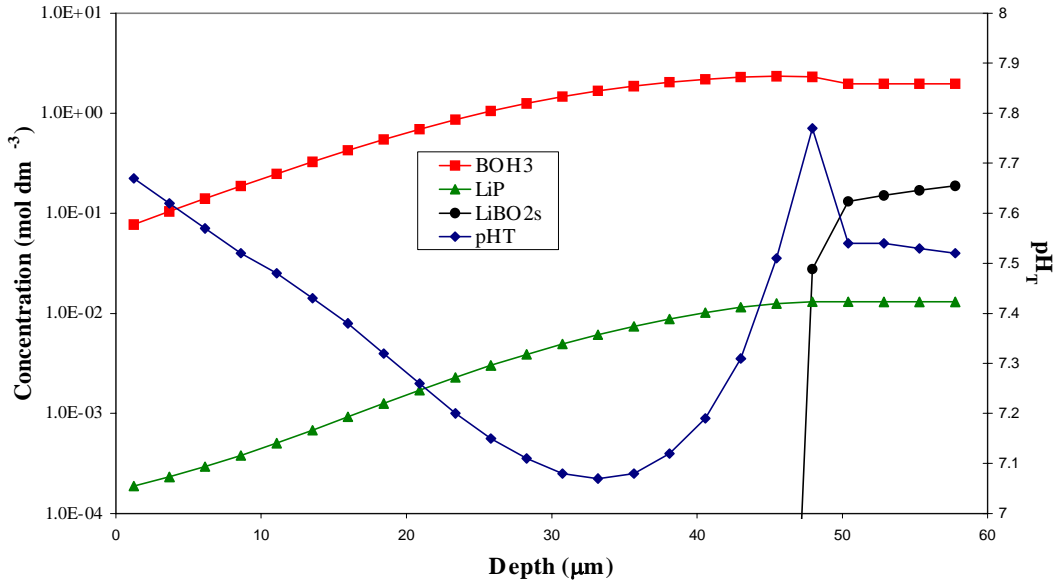


**Figure 5-28**  
 Vogtle 2 Cycle 9 plot of pH, Li<sup>+</sup>, Boric acid concentration and amount of LiBO<sub>2</sub>(s) against depth for a 59µm thick deposit. Calculation with 2ppm Li, 1200ppm B and 25cm<sup>3</sup> kg<sup>-1</sup> (STP) H<sub>2</sub>.

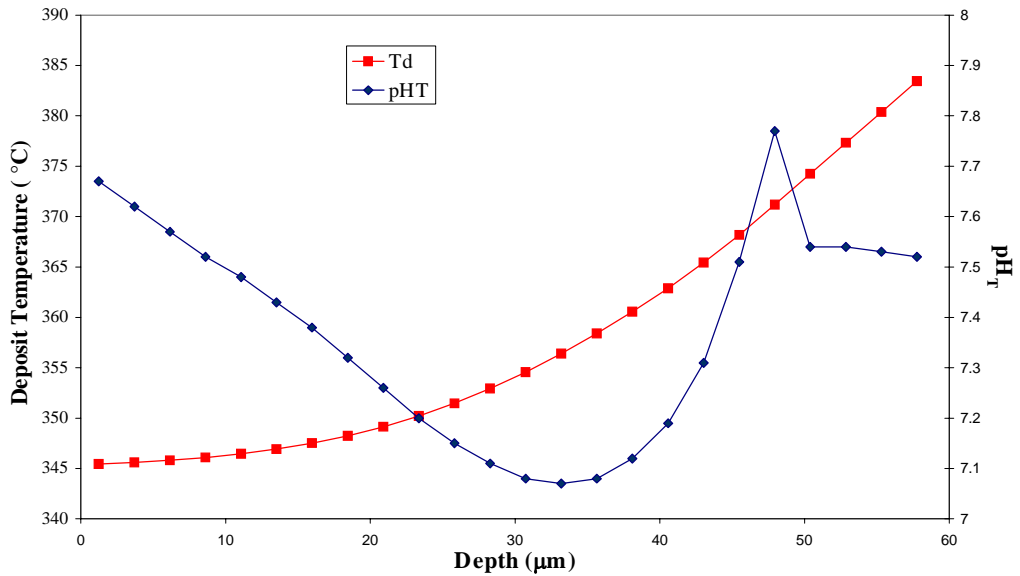


**Figure 5-29**  
 Vogtle 2 Cycle 9 plot of pH and crud temperature against deposit depth for a 35µm thick deposit. Calculation with 2ppm Li, 1200ppm B and 25cm<sup>3</sup> kg<sup>-1</sup> (STP) H<sub>2</sub>.

Results From Crud Chemistry Model (CCM)

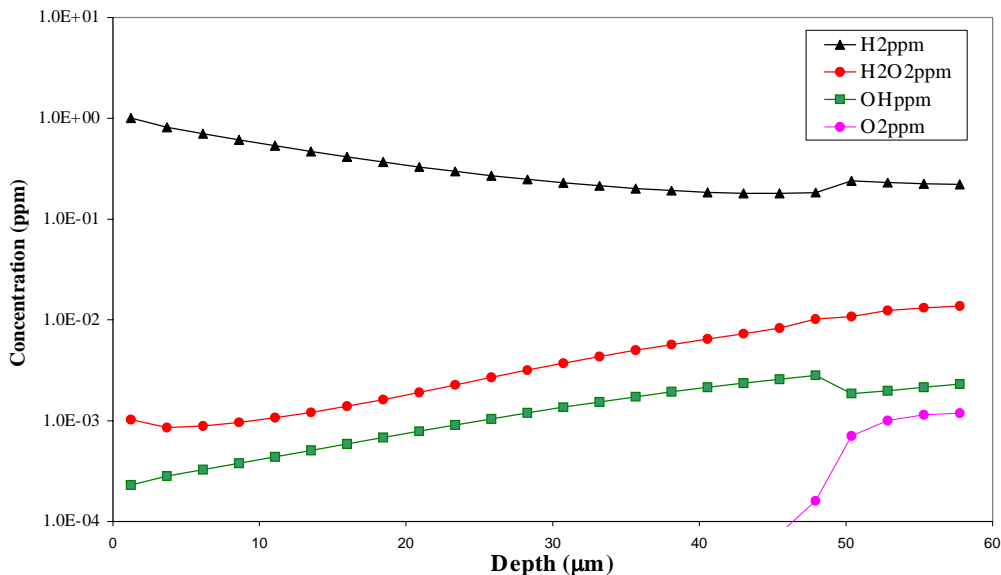


**Figure 5-30**  
 Vogtle 2 Cycle 9 plot of  $H_2$ ,  $H_2O_2$  and OH against depth for a  $59\mu m$  thick deposit.  
 Calculation with 2ppm Li, 1200ppm B and  $25cm^3 kg^{-1}$  (STP)  $H_2$ .

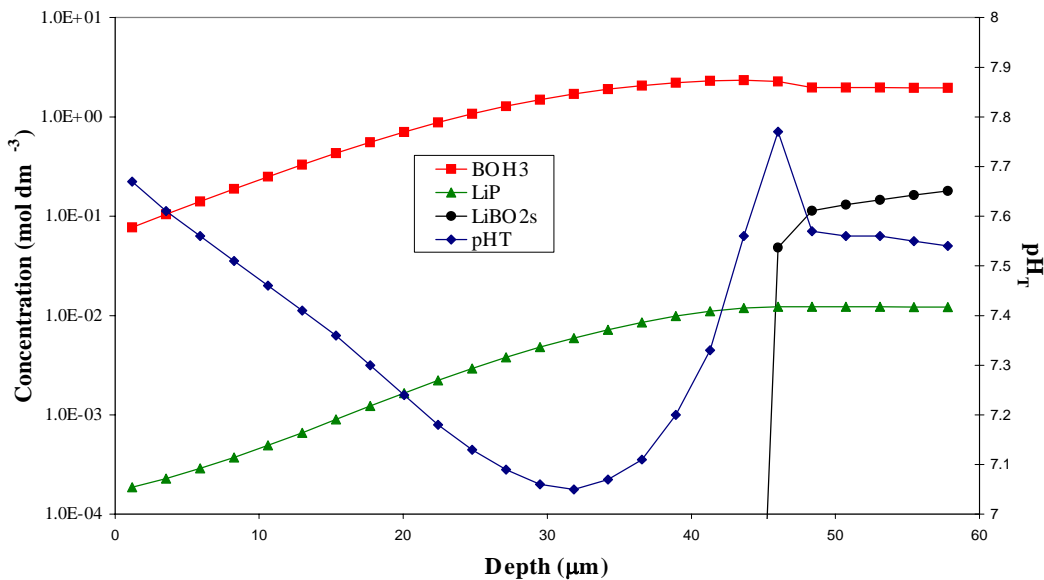


**Figure 5-31**  
 V C Summer Cycle 12 plot of pH,  $Li^+$ , Boric acid concentration and amount of  $LiBO_2(s)$   
 against depth for a  $59\mu m$  thick deposit. Calculation with 2ppm Li, 1200ppm B and  $25cm^3 kg^{-1}$  (STP)  $H_2$ .

Results From Crud Chemistry Model (CCM)

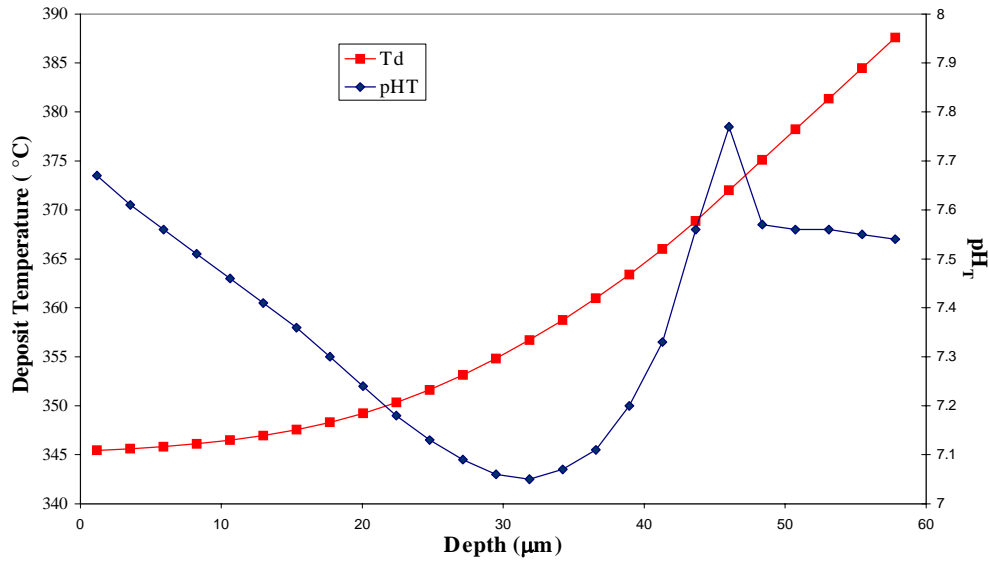


**Figure 5-32**  
 V C Summer Cycle 12 plot of pH and crud temperature against deposit depth for a 35 $\mu\text{m}$  thick deposit. Calculation with 2ppm Li, 1200ppm B and 25cm<sup>3</sup> kg<sup>-1</sup> (STP) H<sub>2</sub>.

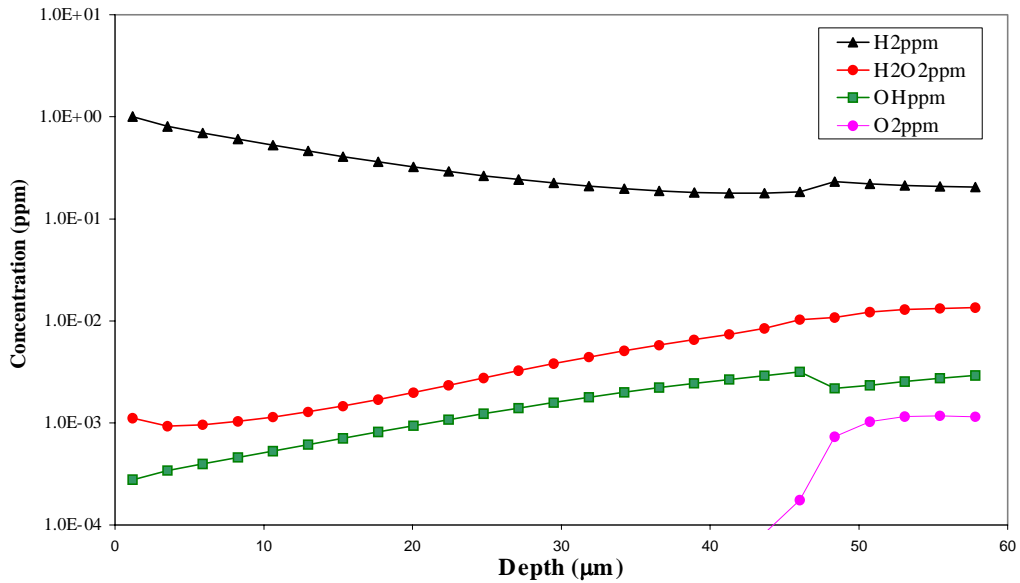


**Figure 5-33**  
 V C Summer Cycle 12 plot of H<sub>2</sub>, H<sub>2</sub>O<sub>2</sub> and OH against depth for a 59 $\mu\text{m}$  thick deposit. Calculation with 2ppm Li, 1200ppm B and 25cm<sup>3</sup> kg<sup>-1</sup> (STP) H<sub>2</sub>.

Results From Crud Chemistry Model (CCM)

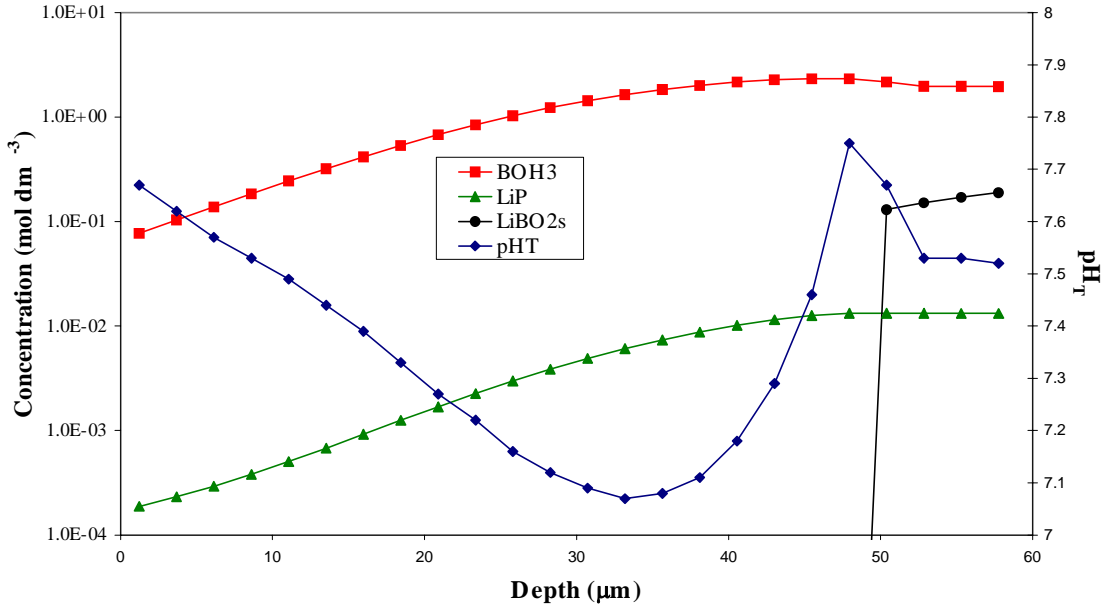


**Figure 5-34**  
 Diablo Canyon Unit 1 Cycle 11 plot of pH, Li<sup>+</sup>, Boric acid concentration and amount of LiBO<sub>2</sub>(s) against depth for a 59μm thick deposit. Calculation with 2ppm Li, 1200ppm B and 25cm<sup>3</sup> kg<sup>-1</sup> (STP) H<sub>2</sub>.

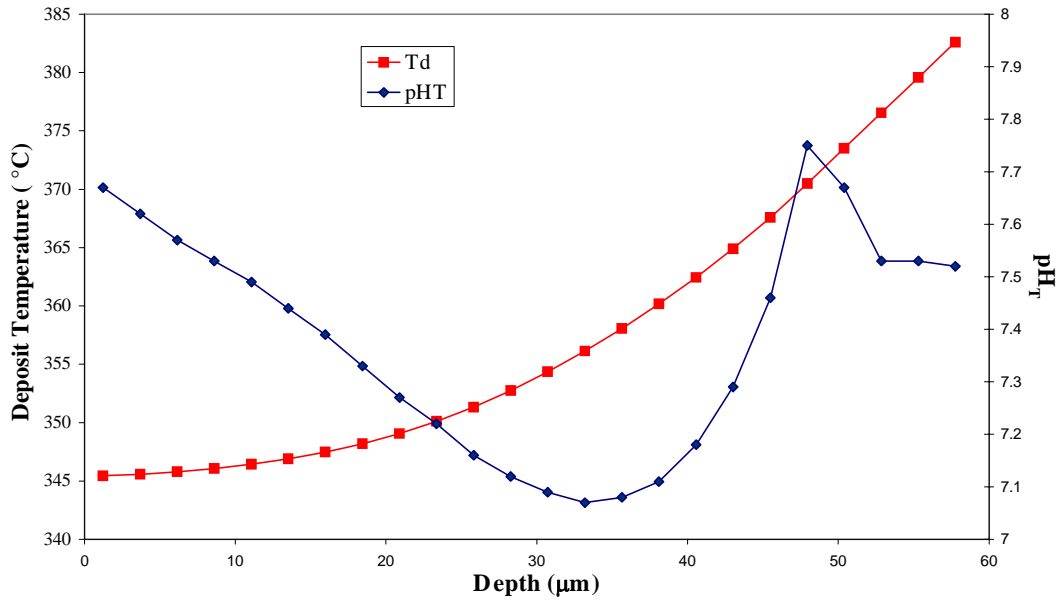


**Figure 5-35**  
 Diablo Canyon Unit 1 Cycle 11 plot of pH and crud temperature against deposit depth for a 35μm thick deposit. Calculation with 2ppm Li, 1200ppm B and 25cm<sup>3</sup> kg<sup>-1</sup> (STP) H<sub>2</sub>.

Results From Crud Chemistry Model (CCM)

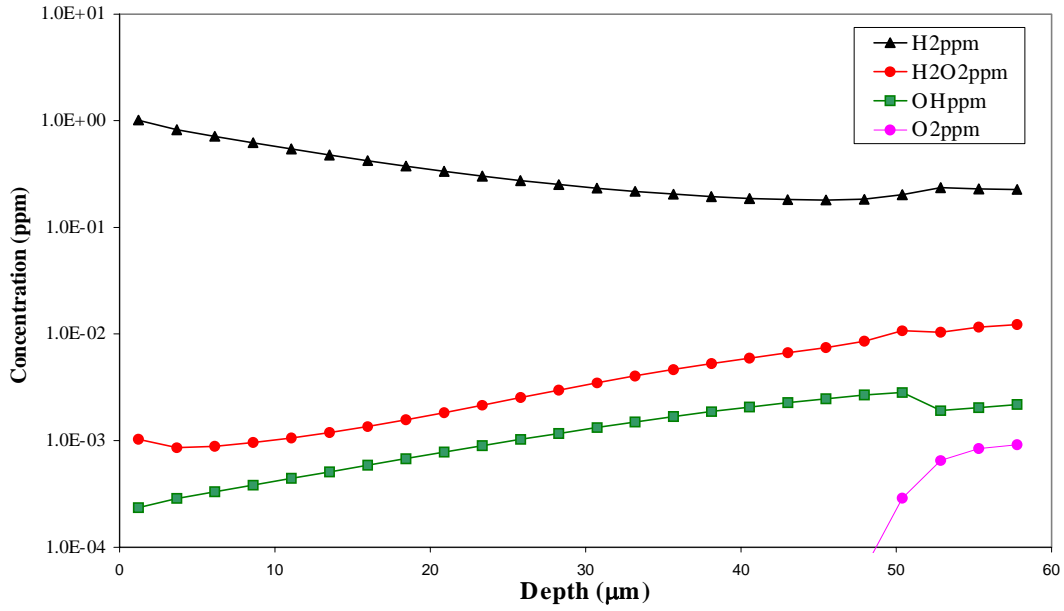


**Figure 5-36**  
 Diablo Canyon Unit 1 Cycle 11 plot of pH and crud temperature against deposit depth for a 35μm thick deposit. Calculation with 2ppm Li, 1200ppm B and 25cm<sup>3</sup> kg<sup>-1</sup> (STP) H<sub>2</sub>.

# 6

## DISCUSSION

---

This report discusses two models for studying crud deposition and growth and AOA; CDM and CCM. CDM is a model that simulates the transport of soluble and insoluble material from the bulk coolant water to the fuel surface in a PWR plant. The model is relatively simple and accounts for transport due to turbulent mass transport and boiling at the fuel surface. The plant is represented by 6 sections corresponding to the cold leg, bottom of the core, bottom of the fuel, top of the core, top of the fuel and hot leg. Soluble species concentrations in each of these sections are calculated using thermodynamics and assuming that the main solid phase present is  $\text{NiFe}_2\text{O}_4(\text{s})$ . The box associated with the fuel surface represents the boundary layer of water adjacent to the fuel and it is assumed that any soluble or insoluble species passing into this layer from the bulk deposits on the fuel and cannot then escape. The model therefore will probably over predict the crud thickness for a given set of plant parameters. In general the crud thicknesses that are calculated by the model are in line with plant observations, being of the order of 1 or 2  $\mu\text{m}$  for non-boiling conditions and 10 to several 100 $\mu\text{m}$  for boiling conditions.

CDM has been used to examine the effect of plant operating parameters on crud thickness calculated over a 12 month cycle. The predictions of the model are relatively obvious in that if you raise the pH by increasing the Li concentration and/or lowering the boric acid concentration, then the thickness of the crud deposit will fall. This is simply because the chemistry predicts less material dissolved in solution. The model indicates that increasing the Li concentration from 1 to 2ppm results in a fall in the crud thickness of approximately 40%. Less soluble material can also be achieved by lowering the hydrogen concentration, since the dissolution of the Ni-Ferrite is reductive, with  $\text{Fe}^{3+}$  becoming  $\text{Fe}^{2+}$  upon dissolving. This requires  $\text{H}_2(\text{aq})$  so that lowering the  $\text{H}_2$  concentration will also lower the thickness of the crud deposit. Since several arguments have been presented to suggest that the amount of hydrogen used in the primary circuit to suppress radiolysis is excessive, then lowering the  $\text{H}_2$  to 5 or 10cc  $\text{kg}^{-1}(\text{STP})$  might be reasonable [23]. The addition of solid particulate to the solution leads, as expected, to a thicker crud deposit. A 30% increase in the amount of material in the water due to particulate gives an approximate 30% increase in the crud thickness.

It is interesting to compare the relative importance of the various plant parameters in determining crud thickness and this can be done by calculating the following sensitivity parameter, S, defined by

$$S = \frac{\text{Fractional Change in crud thickness}}{\text{Fractional Change in parameter}}$$

## Discussion

where the parameter is either the boron concentration, the lithium concentration, the hydrogen concentration or the heat flux. For the calculations that have been carried out this parameter is tabulated in Table 6-1. From Table 6-1 it is clear the most important parameter by a factor of almost 2 is the heat flux. The boron concentration and hydrogen level are the next most important parameters while the lithium concentration is the least important. In other words if the plant is operating with say 1200ppm B, 1ppm Li, 30 cckg<sup>-1</sup>(STP) H<sub>2</sub> at a heat flux of 1MW m<sup>-2</sup>, in order to reduce crud deposit it would be most effective to first drop the heat flux by half, then to drop the B and H<sub>2</sub> by half and finally to increase the Li by a factor of 2.

**Table 6-1**  
**Sensitivity coefficients for plant operating parameters.**

Parameter	Sensitivity Coefficient
[B]	0.55
[Li]	0.22
[H <sub>2</sub> ]	0.52
Heat Flux	0.94

CCM is a relatively sophisticated 1-dimensional approach to modeling the chemistry taking place in fuel crud. The model simulates wick boiling involving heat transport by conduction and evaporation through the crud. Solution of the relevant thermal hydraulics equations enables the calculation of the fluid flow velocity which then allows the solution of the relevant species transport equations. Solving the species transport equations, coupled to the species chemistry equations allows the calculation of species concentrations through the deposit. In the current model this chemistry includes: boron species, Ni species, Fe species and the radiolysis products of water. The chemistry also includes precipitation of Ni metal, NiO, NiFe<sub>2</sub>O<sub>4</sub> and LiBO<sub>2</sub>, as well as partitioning of H<sub>2</sub>, O<sub>2</sub> and H<sub>3</sub>BO<sub>3</sub> into the vapor phase present in the wick chimney.

For typical AOA plant operating conditions CCM predicts that as the crud thickness increases, the concentration of boron species and Li<sup>+</sup> increase and the temperature of the deposit rises. Boiling point elevation due to the presence of solutes is a well known phenomena to elementary chemists, what the model used here has indicated is that this rise in temperature is very significant in the present system. The system saturation temperature at the bulk water/crud interface is approximately 345°C, but at the bottom of a 40µm deposit this could be in the region of 373°C, close to the critical temperature of water, for typical plant operating conditions. This rise in temperature has a number of consequences and in particular it lowers the solubility of LiBO<sub>2</sub>(s), so this precipitates out of solution and it also lowers the enthalpy of vaporization of water, which at the critical temperature is zero. Since the coefficient for evaporative heat transfer is proportional to vaporization enthalpy squared the rate of evaporative heat loss falls to zero as the crud thickness increases. A consequence of this is, for example, at a crud of thickness 60 µm, approximately 20µm of this deposit adjacent to the fuel will contain water that is not undergoing evaporation, so Li<sup>+</sup> and boron will have ceased to be concentrated in this layer and will be at a steady concentration containing LiBO<sub>2</sub>(s).

The results from CCM that have been presented here indicate for typical plant conditions LiBO<sub>2</sub>(s) precipitates out for cruds 35 to 40µm thick, which is where it has been suggested, from

plant observations, that the onset of AOA occurs. Also at this stage the concentration of B in the base of the deposit is 4M, approximately 2M of which is boric acid. For Callaway Cycle 6 it has been estimated the -9% AOA that was observed at 10.5 GWd/MTU was due to 650g of B within the fuel crud [4]. An estimate of the crud volume resulting in AOA has also been given in reference [4] as 7810cm<sup>3</sup>. The average B concentration within the Callaway crud is therefore 8.3M. It is clear therefore a significant fraction of the B within the crud may be soluble material; the amount will be less than 50% the actual value depending on the depth distribution of the crud over the surface of the fuel pin. The larger proportion of B within the crud is probably due to LiBO<sub>2</sub>(s), but again it is impossible to calculate the amount without knowing the depth distribution of crud over the fuel pin and what fraction of this crud is subject to nucleate boiling. The model predictions are consistent with the plant observations.

CCM has also been used to examine the behavior of pH, soluble Ni/Fe ratio and concentrations of radiolysis species within the crud. For thin crud (<35μm) the pH generally falls through the crud from the bulk water to the fuel interface. The change is not large (of the order of 0.3pH units) and is a consequence of the thermodynamics of the boron species as explained in reference [5]. For thick crud (40 - 60μm) the pH behavior is somewhat different with a pronounced minima approximately half to two thirds of the way through the crud. Initially the boric acid chemistry causes the pH to fall, but further into the crud the increase in Li<sup>+</sup> ion concentration, which result in an increase in OH<sup>-</sup> concentration, causes the pH to rise. For a 60μm crud the pH would become quite high [24], of the order of 9, except the precipitation of LiBO<sub>2</sub>(s) removes Li<sup>+</sup> buffering the pH close to what it is in the bulk solution. What is interesting though about this pH behavior is the relatively constant pH in the bottom of the crud close to the fuel pin followed by a sharp pH drop. Moving from a high to low pH zone in this way would cause any saturated Zirconium solution to precipitate out and the subsequent rise in pH towards the water/crud interface would encourage re-dissolution of the precipitated material. Such behavior might account for the band of ZrO<sub>2</sub> that has been found in a number of crud deposits [4]. The soluble Ni/Fe ratio generally mirrors the pH in that it is high when the pH is low and low when the pH is high. A low ratio means that Ni is less soluble than Fe under these conditions, implying a deposit which is becoming Ni rich. The conclusions of the model on the stoichiometry of the solid phase though are inconclusive at this stage, primarily because a number of factors have not been included in the model which will affect this, are discussed below. For thin crud the change in radiolysis species concentrations within the crud from their bulk values is small. Typically for a thin crud hydrogen peroxide changes from 1ppb in the bulk water to 3ppb at the bottom of the crud. For a 60μm deposit the change is larger with the peroxide concentration at the bottom of the crud at approximately 16ppb. This is a reflection of two factors, the increased alpha dose rate at the bottom of the crud and the increased depletion in hydrogen since more would have passed into the vapor phase along the longer wick chimney associated with the thicker crud.

The CCM results discussed in the previous paragraph were for 'standard' operating conditions and an investigation was carried out with the model to study the effect of the various operating conditions on the crud behavior. Changing the bulk lithium concentration had little to no effect. Changing the bulk water boron concentration though did have an effect in thick deposits. Lowering the B from 1800ppm to 300ppm resulted in a fall in the temperature at the base of the deposit from 403°C to 383°C. However, LiBO<sub>2</sub> is still precipitated but the thickness of crud required to cause this precipitation is relatively independent of bulk boron concentration. Similarly the behavior of pH within the crud and soluble Ni/Fe ratio is relatively independent of

## Discussion

bulk water boron concentration. What is relatively sensitive to the boron concentration is the concentrations of radiolysis species. In the case of a 60 $\mu\text{m}$  thick crud deposit with 600ppm of B this peroxide can reach as high as 350ppb at the base of the deposit. The change in peroxide concentration with changing boron concentration is not straight forward as explained. The calculated changes are the result of the fact that increasing boron increases the alpha dose rate, which should increase the peroxide concentration. However, increasing boron lowers the length of crud over which  $\text{H}_2$  gas partitioning is occurring, this increases the concentration of  $\text{H}_2$  in the liquid and lowers the peroxide levels. Which phenomena dominates determines how the concentration of peroxide changes.

The final chemistry parameter over which the plant operator has control in is the  $\text{H}_2$  concentration. Changing this parameter has little to no effect on the temperature, pH, Ni/Fe ratio through the deposit. What the bulk hydrogen concentration does affect is the level of peroxide within the deposit. Dropping the bulk  $\text{H}_2$  from 25 to 10 $\text{cm}^3/\text{kg}$  (STP) causes the peroxide concentration at the bottom of a 60 $\mu\text{m}$  deposit to increase from 16ppb to close to 400ppb. The next parameter that was investigated in the present study was the heat flux from the fuel pin. The temperature profile through the crud, the thickness of crud required to precipitate out  $\text{LiBO}_2(\text{s})$  and the concentration of soluble B within the crud were all very sensitive to this parameter. For example at a heat flux of  $1\text{MWm}^{-2}$   $\text{LiBO}_2(\text{s})$  precipitates out at 30 - 40 $\mu\text{m}$ , while for a heat flux of  $0.5\text{MWm}^{-2}$  precipitation doesn't occur until 70 - 80 $\mu\text{m}$ . The final parameter that was investigated with the model was the neutron flux. The crud property this would be expected to effect is radiolysis species concentrations. For thin crud the effect is small but for crud in the region of 60 $\mu\text{m}$  the increase in peroxide concentration is dramatic with concentrations as high as 4 to 5ppm being predicted by the model upon doubling the neutron flux. The model of course ignores the fact that peroxide decomposes on surfaces and this will lower predicted concentrations.

The two models that have been used in this study derive from basic chemical and physical principles, with no fitting of any parameters to any plant data. CDM gives approximately the correct deposit thickness for non-boiling and boiling conditions. Deposits of 10 to 100 $\mu\text{m}$  can be generated from soluble material without the need for particulate, however the addition of particulate exacerbates matters. CCM indicates that AOA is likely above 35 $\mu\text{m}$  deposit thickness, depending on heat flux and is due to  $\text{LiBO}_2(\text{s})$  precipitation but a significant amount of B within the deposit may be soluble boron. The model indicates the  $\text{ZrO}_2$  layer that has been observed within a number of thick deposits may be a result of the pH change through the deposit. The formation of bonaccordite, also observed in some deposits, could arise from the extreme conditions, high concentrations of boron and temperatures in excess of 400 $^\circ\text{C}$ . What the model does not clearly explain is the observed Ni-Fe stoichiometry changes of the crud and no attempt has been carried out to investigate this closely at this stage. This is because at this stage of the model development such an exercise was not worth while because certain phenomena are not included in the model. In particular the effect of radiolysis species on the cation chemistry has not been included in the model and this will effect the cation speciation, in particular the  $\text{Fe}^{2+}(\text{aq})$  to  $\text{Fe}^{3+}(\text{aq})$  ratio. Calculations here have indicated that under certain operating conditions high local peroxide concentrations can be achieved within the crud and this would certainly effect this ratio. Other factors such as formation of Li from the  $^{10}\text{B}(\text{n}, \alpha)^7\text{Li}$  reaction and adsorption of B on the crud substrate may also alter the pH behavior and therefore the Ni-Fe stoichiometry and these are also not modeled explicitly. Also CCM does not take into account of how the high local

alpha dose and high lithium concentrations may affect the ZrO<sub>2</sub> dissolution rate, and this needs some consideration. Further developments are needed with the models to explain all the plant observations.



# 7

## CONCLUSIONS

---

Two models have been used to investigate AOA, CDM models the crud deposition process and CCM models the chemistry inside the crud. CDM is a very simple model for crud deposition ignoring for example re-suspension processes. CCM is a sophisticated wick boiling model in which the thermal hydraulics is coupled to the chemistry in the crud. These models are based on fundamental chemistry and physical principles and do not involve any fitting of parameters to plant data. Running these models for typical plant conditions indicates:

- Soluble material can account for crud deposits 10 – 100 $\mu$ m thick under boiling conditions over a 12month cycle.
- Decreasing the amount of soluble material by increasing Li, decreasing B or decreasing H<sub>2</sub> will lower the amount of crud. Sensitivity studies with CDM indicate the relative importance of the parameters in determining crud thickness are heat flux>[B]>[H<sub>2</sub>]>[Li].
- Modeling crud chemistry indicates LiBO<sub>2</sub>(s) precipitates out for a crud thickness typical of that observed for AOA plants.
- Modeling crud chemistry indicates a significant amount of soluble boron in the crud.
- The temperature at the bottom of the crud can be as large as 400°C for thick crud. This might explain the formation of bonnacordite within the crud.
- Significant local concentrations (10s – 100s ppb) of hydrogen peroxide can be generated in the crud under certain operational conditions.
- The pH variation through the crud may explain the layer of ZrO<sub>2</sub> that has been observed in thick crud deposits.

Further developments are required to the models before they provide a more complete picture of crud deposition and crud chemistry. These developments are outlined in the following chapter.



# 8

## RECOMMENDATIONS - MODEL DEVELOPMENTS

---

The crud chemistry model that has been described in this report is a complex model of heat and mass transport through a porous deposit in which several different types of chemical processes are taking place. The conditions in the crud are extreme, at very high water temperatures and pressures and as a result a number of simplifications were undertaken to make the problem tractable. The predictions of the model are therefore dependent on whether these assumptions are valid. Also, although the model explains a number of the crud scrape data, it does not explain the fact that the Ni/Fe ratio in crud from AOA plants tends to be higher than in none AOA plants.

In order to test the assumptions and explain the observed Ni/Fe ratio behaviour several developments are recommended for changing the model and these are described here.

### 8.1 Physical Parameters

#### 8.1.1 *Enthalpy of vaporization*

The behaviour of this parameter with temperature is important to the new mechanism of boric acid concentration in the base of the deposit. The behaviour of this parameter with temperature for pure water is well known but its behaviour for water containing solutes has not been reviewed. Work should be performed to review such data and incorporate the results in the model to refine the thermal hydraulics.

#### 8.1.2 *Evaporative heat coefficient*

This parameter determines the rate of heat loss due to evaporation and is a function of the latent heat of vaporization. In the current model a particular formulation of this parameter has been implemented based on a limited number of references. This is also a critical parameter which has a large impact on the thermal hydraulics in the model and requires much greater in-depth review and investigation. There is a large body of data on boiling within porous deposits and review of this information should be performed in order to confirm that the current approach being adopted in this work is adequate.

#### 8.1.3 *Convection*

The model currently assumes that once evaporation stops the only method of heat loss from the base of the deposit is by conduction. The temperature in the base of the deposit rises greatly as a

*Recommendations - Model Developments*

result of this assumption. Heat loss, though, may occur by convection in this region and this should be investigated.

**8.1.4 Thermal conductivity of water**

This is an important parameter for the temperature behaviour of the deposit, especially when evaporative heat loss stops. At present this is modelled as a constant parameter equal to the thermal conductivity of water at the bulk coolant temperature. More data on this parameter at high temperatures, especially near the critical point, is required to have confidence in the thermal hydraulics in the model. A thorough review of the literature is therefore necessary.

**8.2 Chemistry Parameters****8.2.1 Boric Acid Adsorption**

In the current model boron is in solution or precipitated out as  $\text{LiBO}_2$ . Boron may also be adsorbed on the crud material and the importance of this needs to be investigated.

**8.2.2 MULTEQ data**

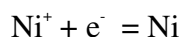
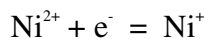
There is new MULTEQ data for Nickel Ferrite/Ni/NiO system and this data needs assessing and incorporating into the model. This data is critical to understanding the Ni/Fe ratio in the deposit.

**8.2.3 High Temperature Radiolysis Rate Constant**

The current radiolysis model is based primarily on the work of Elliot at AECL. Many of the rate constants (G-values) in this model have only been measured up to 250 °C or lower. The current model is predicting temperatures well in excess of 300 °C so how valid these constants are is uncertain. Recent work have started to measure these numbers at very high temperatures (including supercritical water >370 °C) and have found some unexpected results, for example the rate constant of the important reaction  $\text{OH} + \text{H}_2$  starts to fall with increasing temperature above 260 °C, unlike the “Elliot” rate constant which simply rises. The net result is that the solution is probably more oxidizing at elevated temperatures than predicted by the standard model. These results should be incorporated into CCM.

**8.2.4 Ni/Fe Radiolysis Chemistry**

The thermal Ni/Fe chemistry has been implemented into CCM, however, once in solution  $\text{Ni}^{2+}$  and  $\text{Fe}^{2+}$  can interact with the radiolysis species, e.g.



This chemistry is quite extensive and may influence where the Ni/NiO stability lies within the crud. This chemistry should be incorporated in the model.

### **8.3 General**

The CCM model simulates the extreme conditions within fuel crud deposits and many of the parameters used in the model have been extrapolated outside their range of validity. Many of the properties used in the model assume pure water properties perturbed by the presence of the boric acid and lithium compounds. Thus, for example, the critical temperature of the system is assumed to be that of water. In reality we have a complex mixture, which is predominantly water and boric acid and it is the properties of this mixture (its critical point, its saturation temperature, its enthalpy of vaporisation etc) which will be important. An approach for calculating these properties is therefore needed and work is required to develop an approach for calculating them that allows extrapolation of known experimental measurements in a more fundamental way.



## 9

## REFERENCES

- 
1. K Garbet, J Henshaw, M V Polley and H E Sims, 'Oxygen and hydrogen behavior in PWR primary circuits', AEAT-3698, 1998.
  2. I S Woolsey, K Garbett and M V Polley, 'Analysis of primary circuit activity behavior in KWU designed PWRs and its implications for UK designs', TD/RPB/REP/0024, PWR/CTG/P(90)736, 1990.
  3. FACSIMILE a computer package for solving stiff differential equations, licensed by MCPA software ltd.
  4. K Garbett, PWR Fuel Crud Characteristics, G/HSE/014/04, October 2002.
  5. S Dickinson, J Henshaw, J McGurk, H E Sims and A Tuson, Modeling Chemistry in Fuel Crud Deposits, AEAT/R/NS/0660, March 2003.
  6. P Cohen, Heat and mass Transfer for Boiling in Porous Deposits with Chimneys, AIChE Symposium Series, Vol. 70, No. 138, pp. 71-80, (1974).
  7. W L Marshall and E U Franck, Ionic Product of Water Substance, 0-1000oC, 1-10,000 bar. New International Formulation and its Background, J. Chem. Ref. Data 10, 295 (1981).
  8. W T Lindsay, Jr., Chemistry of Steam Cycle Solutions: Principles, in The ASME Handbook on Water Technology for Thermal Power Systems, Paul Cohen Editor-in-Chief, ASME, New York, 1989.
  9. MULTEQ Version 3.0 Manual, Volume 2, EPRI, Palo Alto, CA, 2000, 1000996.
  10. O Weres, Vapor pressure, Speciation, and Chemical Activities in Highly Concentrated sodium Borate Solutions at 277 and 317oC, J. Solution Chem. 24, 409 (1995).
  11. W A Byers, W T Lindsay Jr. and R H Kunig, Solubility of Lithium Monoborate in High Temperature Water, J. Solution Chem. 29, 541 (2000).
  12. J W Cobble and S W Lin, Chemistry of Steam Cycle Solutions: Properties, in The ASME Handbook on Water Technology for Thermal Power Systems, Paul Cohen Editor-in-Chief, ASME, New York, 1989.
  13. J Henshaw and A Tuson, Radiolysis Effects in Sub-cooled Nucleate Boiling, AEAT/R/NS/0579, CPTG/P(02)312, 2002.
  14. A J Elliot, Rate Constants and G-values for the Simulation of the Radiolysis of Light Water over the Range 0 – 300oC, AECL-11073, COG-94-167, 1994.
  15. See for example, K S Pitzer and L Brewer, Thermodynamics, Second Edition, McGraw-Hill, New York, 1961.
  16. W H Press, S A Teukolsky, W T Vetterling and B P Flannery, Numerical Recipes in C, Second Edition, Cambridge University Press, 1992.

*References*

17. J H Keenan and F G Keyes, Thermodynamic Properties of Steam, First Edition, Wiley, New York, 1936.
18. F D Hamblin, Abridged Thermodynamic and Thermochemical Tables, Pergamon Press, Oxford, 1971.
19. Handbook of Chemistry and Physics, 73rd Edition, CRC Press, Boca Raton, 1992.
20. A C Smith, Fluid Flow, Heat and Mass Transfer, in The ASME Handbook on Water Technology for Thermal Power Systems, Paul Cohen Editor-in-Chief, ASME, New York, 1989.
21. C Pan, B G Jones, and A J Michiels, Wick Boiling Performance in Porous Deposits with Chimneys, ASME/AIChE/ANS National Heat Transfer Symposium on Multiphase Flow and Heat Transfer, Denver, August 1985.
22. J G Collier, Convective Boiling and Condensation, Second Edition, McGraw-Hill, New York, 1982.
23. K Garbett, J Henshaw and H E Sims, "Hydrogen and Oxygen Behavior in PWR Primary Circuits", Water Chemistry in Nucl. Reactor Systems, BNES, Bournemouth, UK, Vol1, pg 85, 2000.
24. Presentation made to EPRI Working Group1, September 2003, by J Henshaw

# A

## APPENDIX A: NI-FE THERMODYNAMICS AND DEPOSITION TRANSPORT COEFFICIENTS

---

### Thermodynamics

The equilibrium concentrations in each box will be determined by the temperature in that box and pH. The pH for the box is determined from the thermodynamics for the boric acid and lithium hydroxide equilibrium and will depend on the local temperature as well as the initial boric acid and lithium concentrations. These pH values are calculated using a separate model and then input as parameters in the present model. The values that have been used in the simulations are given in Table 2-1. The equilibrium constants for the various reactions are derived from the enthalpy and entropy values for the relevant species in the reactions. These are functions of temperature the coefficients for which are given in Table A-1, and are derived from reference [A.1]. The enthalpy and entropy for a species are derived from the coefficients in Table A-1 using the functions

$$F(T) = a_2 T + \frac{1}{2} a_3 T^2 + \frac{1}{3} a_4 T^3 - \frac{a_5}{T} \quad (\text{A.1})$$

$$P(T) = a_2 \log(T) + a_3 T + \frac{1}{2} a_4 T^2 - \frac{1}{2} \frac{a_5}{T^2} \quad (\text{A.2})$$

From which the enthalpy and entropy (in kJ, mol, K) are given by

$$H_T = a_0 + F(T) - F(298) \quad (\text{A.3})$$

and

$$S_T = a_1 + P(T) - P(298) \quad (\text{A.4})$$

Note that T is in degrees Kelvin in these equations. For the thermodynamic properties of water coefficients were taken from the CHEMKIN data base [A.2] and use the following expressions to evaluate the enthalpy and entropy.

$$\frac{H_T}{RT} = a_0 + \frac{1}{2} a_1 T + \frac{1}{3} a_2 T^2 + \frac{1}{4} a_3 T^3 + \frac{1}{5} a_4 T^4 + \frac{a_5}{T} \quad (\text{A.5})$$

Appendix A: Ni-Fe Thermodynamics and Deposition Transport Coefficients

$$\frac{S_T}{R} = a_0 \log(T) + a_1 T + \frac{1}{2} a_2 T^2 + \frac{1}{3} a_3 T^3 + \frac{1}{4} a_4 T^4 + a_6 \quad (\text{A.6})$$

where R is the gas constant (8.314 J K<sup>-1</sup> mol<sup>-1</sup>) and the coefficients a<sub>0</sub> to a<sub>6</sub> are given in Table A-2.

The enthalpy, entropy, Gibbs energy and equilibrium constants can then be calculated in the model at temperature for the various reactions outlined above.

**Table A-1**  
**Thermodynamic coefficients for determining the enthalpy and entropy of formation.**

Species	a <sub>0</sub>	a <sub>1</sub>	a <sub>2</sub>	a <sub>3</sub>	a <sub>4</sub>	a <sub>5</sub>
Ni	0.0	2.9874E-1	5.2106E-2	-9.1040E-05	1.0950E-07	-7.6800E+02
NiO	-240580E-3	38.074E-3	-20.878E-3	0.15723E-3	0	1.63E+03
Ni <sup>2+</sup>	-54511E-3	-133.54E-3	-105.14E-3	0	0	0
NiOH <sup>+</sup>	-284140E-3	-51.806E-3	-77E-3	0	0	0
Ni(OH) <sub>2</sub>	-534605E-3	-73.08E-3	145.8E-3	0	0	0
Ni(OH) <sub>3</sub> <sup>-</sup>	-767556E-3	-55.36E-3	873E-3	-2.06E-3	0	0
Fe <sub>3</sub> O <sub>4</sub> (s)	-1118400E-3	145.27E-3	97.655E-3	0.19535E-3	0	-7.62E+02
Fe <sup>2+</sup>	-92726E-3	-107.2E-3	23.339E-3	-0.025282E-3	2.24E-08	-1.59E+03
FeOH <sup>+</sup>	-323240E-3	-30.171E-3	-8.5151E-3	0.252E-3	-2.4280E-07	3.6810E+02
FeOH <sub>2</sub>	-540520E-3	29.1E-3	133E-3	0	0	0
Fe(OH) <sub>3</sub> <sup>-</sup>	-773880E-3	29.9E-3	171E-3	0	0	0
NiFe <sub>2</sub> O <sub>4</sub>	-1.08E+03	1.26E-1	1.53E-1	7.78E-05	0	-1.49E+03
H <sub>2</sub> (aq)	-4.20E+00	5.80E-02	1.26E-01	0	0	0
OH <sup>-</sup>	-230.025	-0.01071	-0.163938802	0	0	0

**Table A-2**  
**Thermodynamic parameters for determining the enthalpy and entropy of water.**

Coefficient	Value
a <sub>0</sub>	6.5124E-03
a <sub>1</sub>	-9.0014E-06
a <sub>2</sub>	-1.1200E-08
a <sub>3</sub>	2.0800E-10
a <sub>4</sub>	-2.4100E-13
a <sub>5</sub>	-3.6100E+01
a <sub>6</sub>	-2.6600E-02

## Deposition and Transfer coefficients

The constants  $k_1$  to  $k_7$  determine the rate of material transport between the various compartments of the model.  $k_1$  is just the transfer of material due to bulk flow and is given by

$$k_1 = F / V \quad (\text{A.7})$$

where  $F$  is the volume flow rate through the core and  $V$  the volume of water in the core region. Using the parameters in Table A-2 gives  $k_1$  as  $1.9\text{s}^{-1}$ .

To calculate  $k_2$  the mass transfer rate of bulk water to the fuel surface,  $k_m$ , is required. This is obtained from the standard expression

$$k_m = \frac{1}{2} f v S c^{-\frac{2}{3}} \quad (\text{A.8})$$

where  $f$  is the fanning friction factor,  $v$  is the flow velocity and  $Sc$  is the Schmidt number. The fanning friction factor is calculated using

$$f = (1.58 \log(\text{Re}) - 3.28)^{-2} \quad (\text{A.9})$$

$\text{Re}$  is the Reynolds number for the flow, given by

$$\text{Re} = \frac{d v \rho}{\mu} \quad (\text{A.10})$$

and the Schmidt number is

$$Sc = \frac{\mu}{\rho D} \quad (\text{A.11})$$

where  $d$  is the effective diameter of the channel,  $\rho$  the density and  $\mu$  the viscosity of water and  $D$  the diffusion constant of the dissolved species being transported. The viscosity of water is given by the expression (in  $\text{kg m}^{-1} \text{s}^{-1}$ )

$$\mu = 1.0^{-4} \exp(-6.140834 - 1103.164/T + 457155.3/T^2) \rho \quad (\text{A.12})$$

where the density (in  $\text{kg m}^{-3}$ ) is given by

$$\rho = 997 + 2.01 \times 10^{-1} T(^{\circ}\text{C}) - 8.16 \times 10^{-3} T(^{\circ}\text{C})^2 + 2.91 \times 10^{-5} T(^{\circ}\text{C})^3 - 4.44 \times 10^{-8} T(^{\circ}\text{C})^4 \quad (\text{A.13})$$

The diffusion constant for  $\text{Fe}^{2+}$  is used to calculate the mass transfer rate which has a value of  $1.4 \times 10^{-8} \text{ m}^2 \text{ s}^{-1}$  at  $300^{\circ}\text{C}$ .

*Appendix A: Ni-Fe Thermodynamics and Deposition Transport Coefficients*

The rate constant  $k_2$  is then given by

$$k_2 = k_m \frac{S}{V} \quad (\text{A.14})$$

where  $S/V$  is the surface to volume ratio associated with the flow through the core. For the present simulations using the plant parameters in Table A-2 and the above equations give  $k_2$  in the core region as  $0.27\text{s}^{-1}$ .

Material transported to the surface is deposited in the boundary layer of water adjacent to the fuel. This has a thickness  $\delta$  given by

$$\delta = \frac{D}{k_m} \quad (\text{A.15})$$

The volume of this region is simply  $\delta S$ , so the constant  $k_3$  is given by

$$k_3 = \frac{k_m^2}{D} \quad (\text{A.16})$$

which in the present model has a value of  $9.2\text{s}^{-1}$ .

In the top half of the core 5% of the fuel surface is undergoing boiling and as a result of this mass flow of vapor away from the fuel surface an equivalent mass flow of water towards the surface will occur. This water will contain soluble and insoluble material which can be deposited on the fuel surface. The mass flux of liquid towards the surface is given by

$$\underline{j} = \frac{q}{h} \quad (\text{A.17})$$

where  $q$  is the evaporative heat flux ( $\text{J m}^{-2} \text{s}^{-1}$ ) and  $h$  is the latent heat of vaporization ( $\text{J kg}^{-1}$ ). The rate of change of species concentration within the boundary layer adjacent to the fuel is then given by

$$\frac{dc}{dt} = \frac{j}{\rho\delta} c \quad (\text{A.18})$$

and for the bulk water we have

$$\frac{dc}{dt} = \frac{jS}{\rho V} c \quad (\text{A.19})$$

so that

## Appendix A: Ni-Fe Thermodynamics and Deposition Transport Coefficients

$$k_4 = \frac{jS}{\rho V} \quad (\text{A.20})$$

and

$$k_5 = \frac{j}{\rho \delta} \quad (\text{A.21})$$

For a heat flux of  $5 \times 10^5 \text{ W m}^{-2}$   $k_4$  has a value of  $0.6 \text{ s}^{-1}$  and  $k_5$  is  $20.2 \text{ s}^{-1}$ .

The calculation of the rate constants  $k_6$  and  $k_7$  associated with the transport of particulate material to the fuel due to turbulence is exactly the same as for the soluble material, except that the diffusion constant used to determine the mass transfer rates is evaluated using the Stokes-Einstein relationship

$$D = \frac{k_B T}{6\pi\mu r} \quad (\text{A.22})$$

where  $k_B$  is the Boltzmann constant and  $r$  the radius of the particle. The values of all the rate constants 1 – 7 are tabulated in Table A-3.

**Table A-3**  
**Model rate constants.**

Rate Constant ( $\text{s}^{-1}$ )	Value
$k_1$	1.9
$k_2$	0.27
$k_3$	9.2
$k_4$	0.6
$k_5$	20.2
$k_6$	0.025
$k_7$	0.85

Appendix A: Ni-Fe Thermodynamics and Deposition Transport Coefficients

### Mass Flux equations

The mass flux of soluble and insoluble material to the fuel surface due to turbulent mass transport and boiling determines the rate of growth of the crud. From the above equations the mass fluxes to the boiling ( $j_B$ ) and non-boiling ( $j_{NB}$ ) parts of the fuel surface are given by

$$j_{NB} = \left( \sum_{i, \text{species}} [k_3(c_2^l - c_3^l)mw]_i + k_7 c_2^p m \right) \delta \quad (\text{A.23})$$

$$j_B = \left( \sum_{i, \text{species}} ([k_3(c_4^l - c_5^l) + k_5 c_4^l]mw)_i + (k_7 c_4^p + k_5 c_4^p) m \right) \delta \quad (\text{A.24})$$

where  $mw$  is the molecular weight of the species and  $m$  the mass of the particle. The summation is over all thirteen soluble species in the system. If  $x$  is the crud thickness then

$$\frac{dx}{dt} = \frac{1}{\rho_{crud}} j \quad (\text{A.25})$$

where  $\rho_{crud}$  is the density of the crud and  $j$  is either the boiling or non-boiling flux. In order to calculate the crud thickness a crud density of  $1000 \text{ kg m}^{-3}$  was assumed.

The above model has been implemented in FACSIMILE, a high level computer language for modelling chemical kinetics and transport. The FACSIMILE program is a robust numerical integration package ideally suited for the types of equations described above.

### References

- A.1 S Dickinson and H E Sims, Thermodynamic modelling of PWR coolant, AEAT/R/NT/0325, 2001.
- A.2 R J Kee, F M Rupley and J A Miller, 'The CHEMKIN thermodynamics data base', Sandia report SAND87-8215B, 1990.

---

If  $m$  is in kg and  $\delta$  is in m, then the concentrations should be expressed in moles  $\text{m}^{-3}$  and the molecular weight  $mw$  should be in  $\text{kg mole}^{-1}$ .

# B

## APPENDIX B: D CHAPMAN (WESTINGHOUSE) CALCULATION OF PLANT OPERATING CONDITIONS.

---

This appendix provides the radiation environment and supporting nuclear data and information needed for the chemistry analyses, including radiolysis chemistry related to crud buildup. The environment of specific interest is in the reactor coolant near the surface of the fuel rods. The general radiation environment parameters provided here include:

1. Neutron energy deposition rate (Rads/hour).
2. Gamma energy deposition rate (Rads/hour).
3.  $^{10}\text{B}$  neutron absorption cross-section (barns).
4. Neutron flux (neutrons/barn-sec).
5. Total heat flux (BTU/hour-foot<sup>2</sup>; gamma and neutron).

Three rods (and corresponding plant/cycles) were selected as a means to define the range of the radiation environment (as defined by the parameters stated above). The overall goal is to demonstrate that the investigated parameter ranges have limited sensitivity in the final radiolytic/chemistry calculations performed in this report. The rods selected came from cycle designs for Vogtle 2 Cycle 9 (4-loop, high duty, medium AOA), V. C. Summer Cycle 12 (3-loop, high duty, no AOA), and Diablo Canyon 1 Cycle 11 (4-loop, low duty, no AOA, zinc addition plant). While V.C. Summer is generally regarded as being an upper bound case in terms of fuel duty, Vogtle 2 Cycle 9 is being included to ensure three and 4-loop units, and their respective core designs, do not exhibit significantly different cases. Rod-specific and whole core data are provided for each of these cycle designs. Explicit calculations (using the Monte Carlo code MCNP) were performed in order to characterize the radiation environment (items 1, and 2). The supporting nuclear data (items 3, 4, and 5) were obtained from available nuclear models applicable to each of the cycle designs noted.

### Methodology and Calculations

#### *Radiation Data (Monte Carlo Calculations)*

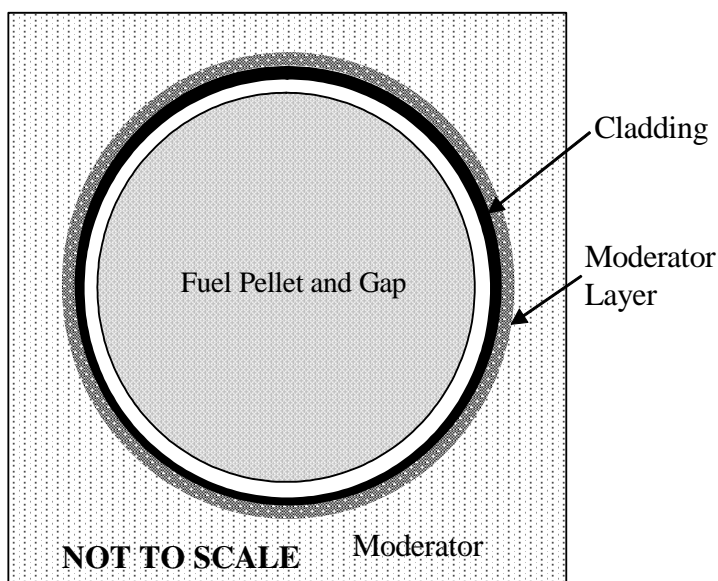
The radiation environment is comprised of the neutron and gamma energy deposition and related values. Calculations were performed using the three-dimensional Monte Carlo neutron transport code MCNP Version 4B. The one- and two-dimensional capability of MCNP was used for these calculations. MCNP is a general-purpose, continuous-energy, generalized geometry, time-dependent, coupled neutron-photon-electron, Monte Carlo transport code system. MCNP treats an arbitrary three-dimensional configuration of materials in geometric cells bounded by first- and

*Appendix B: D Chapman (Westinghouse) Calculation of Plant Operating Conditions.*

second-degree surfaces and some special fourth-degree surfaces. Point-wise continuous-energy cross-section data (including both neutrons and gammas) are used. For neutrons, all reactions in a particular cross-section evaluation are accounted for. Both free gas and  $S(\alpha, \beta)$  thermal treatments are available. A very general source and tally structure is available. Rapid convergence is enabled by a wide variety of variance reduction methods (References B.1 and B.2).

**Description of Models**

A one-dimensional (axial) model was used for most of the calculations. This basic MCNP model included the full axial length of the active portion (12 feet) of a fuel rod. Separate models were generated in order to represent the core average and the rods of interest for each of the cycle designs (six total). Each calculation represents cycle average conditions. Differing nuclide concentrations were used in order to simulate the variations in the nuclide inventory environment. The axial variation in the moderator density was also simulated, though this was determined to have a minimal effect on the neutron and gamma energy deposition results. Additional calculations were performed in order to define the axial variation attributed to the fuel power/flux. The MCNP models (using nominal dimensions) included: the active fuel pellets, a void (or fill gas) gap between the fuel and cladding, the fuel rod cladding, the surrounding water coolant and soluble boron.



A crud layer was not explicitly simulated, but is represented by a thin moderator layer surrounding the cladding, since the interest is primarily in the moderator region and due to the complexity of defining the composition/thickness applicable to the simulation. Miscellaneous fuel components (grids, thimble tubes, etc.) not described above were not modeled.

Two-dimensional (radial) MCNP calculations were also performed. Combined with the one-dimensional results, these calculations approximate a three-dimensional model. The radial calculations simulated an array of fuel rods, from which the contribution from adjacent rods could be assessed.

*Appendix B: D Chapman (Westinghouse) Calculation of Plant Operating Conditions.*

**Description of the Source**

The general source capability of the MCNP code was used. A neutron fission source energy distribution specific to each of the cases was used. The neutron source was applied in a single fuel rod (or portion of a rod) in each of the calculations. The MCNP source capability includes generating a specified number of particles (80,000 for these calculations), with random variation in the initial position, direction, and energy for the neutrons that will be started and tracked in the geometry by MCNP. Confirmation that a sufficient number of particles were generated is provided by review of the statistical results.

**Variance Reduction**

Elaborate variance reduction techniques (such as geometry truncation, source energy biasing, and geometry splitting / Russian roulette controlled by the use of space- and energy-dependent weight windows) were not used in the MCNP calculations.

**Radiation Environment Tallies**

The neutron and gamma energy deposition rates were calculated directly by MCNP. These parameters were calculated in MCNP using track length estimators for the neutron/gamma flux a portion of the moderator cells representing the moderator in close proximity to the fuel cladding. Segmentation of the tally cells was performed in order to provide distribution (axial and radial) information.

**Nuclear Data**

Supporting nuclear data was obtained from available three-dimensional nuclear models applicable to each of the cycle designs generated by the Westinghouse APA code system (References B.3 and B.4)

**Results**

Data are provided in Tables B-1, B-2, and B-3 for (respectively) Vogtle 2 Cycle 9, V. C. Summer Cycle 12 and Diablo Canyon 1 Cycle 11. Supplemental information is provided in Figures B-1 through B-3 for each of these cycle designs (respectively). Separate columns provide values for the core average and the specific rods of interest. The assembly, face and rod number are provided in the column heading for each specific rod of interest.

The neutron and gamma energy deposition rates (Rads/hour) into the coolant adjacent to the fuel rod cladding are provided first. The relative error (%) in the calculated energy deposition rates is included. Also provide is the energy deposition rate in the entire moderator surrounding the fuel rod (generally near-identical to the value adjacent to the cladding). Since these were modeled as a single rod (with reflective boundary conditions), they effectively represent an infinite lattice of like fuel rods. Since the fuel rods are not all alike (either in isotopic makeup and power/flux magnitude), the “Lattice Effect” value (based upon the two-dimensional radial calculations)

*Appendix B: D Chapman (Westinghouse) Calculation of Plant Operating Conditions.*

provides an estimate of the expected relative change in the specific rod for each of the cycle designs. In all cases, this is a reduction (ratio <1.00).

The boron absorption cross-sections ( $^{10}\text{B}$  isotope only) and neutron flux values are provided in two energy groups (“thermal” and “fast”). The energy breakpoint for the two groups is 0.625 eV. A one group absorption cross-section can be obtained by using a flux-weighted sum. The boron cross sections were determined for neutron absorption in boron from boric acid in the coolant. They also reasonably represent the boron microscopic absorption cross sections for any boron retained in the crud.

The values of the heat flux provided represent the heat flux transferred through the fuel cladding. An additional 2.7% is deposited directly in the coolant by gamma rays and neutron slowing down. The average core value does not change since the power production is constant. For a single rod, the value will change over the cycle due to changes in the power distribution. Three separate values are provided representing the beginning (BOC), middle (MOC), and end (EOC) of cycle. These values represent “snapshots” of the core at that time in the core life. A cycle average value is also provided.

The axial dependence of the heat flux distributions are provided in the corresponding figures. The figures use labels for the rod of EFPD (Effective Full Power Days) to represent the cycle time-dependence. Also provided is a plot of the cycle averaged value (determined using integration over the full cycle) illustrating the adequacy of assuming MOC values as a cycle-averaged value. Grid locations (both structural and intermediate flow mixing grids) and span numbering correspondence (relating the crud scrape numbering) are indicated by the vertical lines.

The power density for each cycle design is provided in order to provide a more ready comparison between the three designs for which data is being provided.

The relative power production is listed next. By definition, the average of the core is unity. Due to changes in the power distributions, the value for a given rod will change during the cycle life. These changes are reflected in the BOC, MOC, and EOC values provided.

The cycle-averaged relative power for the highest powered rod is also provided. This provides a comparison of the rods summarized in detail versus the highest powered rod.

The cycle-averaged relative axial power distribution is also provided. As noted in the discussions for the radiation doses, these values can be used to represent the relative axial dependency of the neutron and gamma dose rates.

## Conclusions

Boron absorption cross-sections are very similar, reflecting that these are basic nuclear data with some variation attributable to the specific plants/designs. Core average neutron flux and heat flux closely follow the trend of the core average power density; any differences are attributable to moderator temperature differences between the plants and/or specifics related to the

*Appendix B: D Chapman (Westinghouse) Calculation of Plant Operating Conditions.*

plant/design. The flux values for the specific rods of interest follow the trend of the “Relative Power Production.”

The variation in the core average energy deposition rates is relatively small, ranging from  $3.4\text{E}+9 \pm 3.2\%$  to  $3.8\text{E}+9 \pm 3.4\%$  Rads/hour for neutrons and  $4.9\text{E}+8 \pm 4.3\%$  to  $5.4\text{E}+8 \pm 4.4\%$  Rads/hour for gammas. Generally, the individual rods (all at a power greater than the core average) follow the trend of the average value (“AVG”) of the “Relative Power Production” in the tables. The variation is noted to be larger than that of the core average. This is primarily attributed to the changing nuclide concentrations for the rods and related impact on the fission source energy spectrum.

Parameter values for the peak (or highest-powered) rod are estimated to be 5-10% higher than the values for each of the specific rods of interest. This is determined by taking the ratio of the “Peak Rod Relative Power Production” and cycle average value (“AVG”) of the “Relative Power Production” for the specific rod. For Vogtle 2 Cycle 9, this is ~10% ( $1.40 / 1.271 = 1.10$ ).

MCNP calculations confirmed that the energy deposition rates closely follow axial core power distribution. The top and bottom 10% of the core (no crud scrapes taken) exhibited the greatest deviation from this approximation. Therefore, the axial variation in energy deposition rates can be estimated by multiplying by the “Core Average Relative Axial Distribution” at the axial height of interest. The axial variation in the heat flux is provided directly in Figures B-1 through B-3.

## References

- B.1 ORNL RSIC CCC-660, MCNP4B Monte Carlo N-Particle Transport Code System, March 1997.
- B.2 ORNL RSIC DLC-189, MCNPXS, Standard Neutron, Photon, and Electron Data Libraries for MCNP4B, April 1997.
- B.3 Nguyen, T. Q., et al., Qualification of the PHOENIX-P/ANC Nuclear Design System for Pressurized Water Reactor Cores, WCAP-11596-P-A, June, 1988.
- B.4 Liu, Y. S., et al., ANC-A Westinghouse Advanced Nodal Computer Code, WCAP10965-P-A, September, 1986.

Appendix B: D Chapman (Westinghouse) Calculation of Plant Operating Conditions.

**Table B-1**  
**Data for Vogtle 2 Cycle 9**

	Core	Assembly 6L23 Face 2 Rod 10
Neutron Energy Deposition Rate (Rads/hour) and error Cladding Layer (All Surrounding Moderator)	3.52E+09 ±3.1% (3.46E+09 ±3.1%)	4.54E+09 ±3.3% (4.46E+09 ±3.2%)
Gamma Energy Deposition Rate (Rads/hour) Cladding Layer (All Surrounding Moderator)	4.87E+08 ±4.3% (4.80E+08 ±4.2%)	5.82E+08 ±4.2% (5.81E+08 ±4.2%)
Lattice Effect (relative to single rod results)	1.00	0.97
Boron Absorption Cross-sections (barns)	Fast Thermal 47.1 2090	47.1 2090
Neutron flux (neutrons/barn-second)	Fast Thermal 0.3200E-09 0.4346E-10	0.4028E-09 0.5537E-10
Average Clad Surface Heat flux (BTU/hour-foot <sup>2</sup> ) (Total heat flux is 102.7% of this value)	205605	BOC 240352 MOC 262146 EOC 262146 AVG 261324
Height Dependent Heat Flux	Figure B-1	Figure B-1
Power Density (W/cc)	108.04	
Relative Power Production	1.00	BOC 1.169 MOC 1.275 EOC 1.212 AVG 1.271
Peak Rod Relative Power Production		AVG 1.40

Appendix B: D Chapman (Westinghouse) Calculation of Plant Operating Conditions.

**Table B-1 (continued)**  
**Data for Vogtle 2 Cycle 9**

Core Average Relative Axial Power Distribution	Height (cm)	Height (in)	Relative Power
	358.69	141.22	0.618
	347.24	136.71	0.760
	339.61	133.70	0.845
	328.16	129.20	0.931
	312.90	123.19	0.995
	297.63	117.18	1.024
	282.37	111.17	1.038
	267.11	105.16	1.044
	251.84	99.15	1.048
	236.58	93.14	1.050
	221.32	87.13	1.053
	206.05	81.12	1.056
	190.79	75.11	1.058
	175.53	69.11	1.062
	160.26	63.09	1.065
	145.00	57.09	1.069
	129.74	51.08	1.073
	114.47	45.07	1.078
	99.21	39.06	1.082
	83.95	33.05	1.085
	68.68	27.04	1.083
	53.42	21.03	1.067
	38.16	15.02	1.016
	26.71	10.52	0.936
	19.08	7.51	0.847
	7.63	3.00	0.663

*Appendix B: D Chapman (Westinghouse) Calculation of Plant Operating Conditions.*

**Table B-2**  
**Data for V. C. Summer Cycle 12**

	Core	Assembly P56 Face 2 Rod 12
Neutron Energy Deposition Rate (Rads/hour) and error Cladding Layer (All Surrounding Moderator)	3.81E+09 ±3.4% (3.75E+09 ±3.4%)	5.38E+09 ±3.4% (5.29E+09 ±3.4%)
Gamma Energy Deposition Rate (Rads/hour) Cladding Layer (All Surrounding Moderator)	5.39E+08 ±4.4% (5.37E+08 ±4.3%)	7.85E+08 ±4.4% (7.75E+08 ±4.4%)
Lattice Effect (relative to single rod results)	1.00	0.86
Boron Absorption Cross-sections (barns)	Fast Thermal 45.5 1996	45.5 1996
Neutron flux (neutrons/barn-second)	Fast Thermal 0.3198E-09 0.4124E-10	.4117E-09 .4958E-10
Average Clad Surface Heat flux (BTU/hour-foot <sup>2</sup> ) (Total heat flux is 102.7% of this value)	205603	BOC 268106 MOC 278181 EOC 267901 AVG 274480
Height Dependent Heat Flux	Figure B-2	Figure B-2
Power Density (W/cc)	108.04	
Relative Power Production	1.00	BOC 1.304 MOC 1.353 EOC 1.303 AVG 1.335
Peak Rod Relative Power Production		AVG 1.42

Appendix B: D Chapman (Westinghouse) Calculation of Plant Operating Conditions.

**Table B-2 (continued)**  
**Data for V. C. Summer Cycle 12**

Core Average Relative Axial Power Distribution	Height (cm)	Height (in)	Relative Power
	362.50	142.72	0.402
	354.87	139.71	0.488
	347.24	136.71	0.709
	340.88	134.20	0.787
	337.07	132.70	0.835
	328.16	129.20	0.911
	312.90	123.19	0.993
	297.64	117.18	1.032
	282.37	111.17	1.049
	263.29	103.66	1.060
	240.40	94.65	1.067
	217.50	85.63	1.072
	194.61	76.62	1.078
	171.71	67.60	1.083
	148.82	58.59	1.089
	125.92	49.57	1.095
	103.03	40.56	1.101
	83.95	33.05	1.102
	68.68	27.04	1.097
	53.42	21.03	1.073
	38.16	15.02	1.002
	29.25	11.52	0.924
	25.44	10.02	0.874
	19.08	7.51	0.784
	11.45	4.51	0.530
	3.82	1.50	0.401

Appendix B: D Chapman (Westinghouse) Calculation of Plant Operating Conditions.

**Table B-3**  
**Data for Diablo Canyon Unit 1 Cycle 11**

	Core	Assembly DD52 Face 2 Rod 10
Neutron Energy Deposition Rate (Rads/hour) and error Cladding Layer (All Surrounding Moderator)	3.39E+09 ±3.2% (3.34E+09 ±3.2%)	4.61E+09 ±3.2% (4.55E+09 ±3.2%)
Gamma Energy Deposition Rate (Rads/hour) Cladding Layer (All Surrounding Moderator)	4.71E+08 ±4.4% (4.70E+08 ±4.3%)	6.48E+08 ±4.1% (6.39E+08 ±4.1%)
Lattice Effect (relative to single rod results)	1.00	0.98
Boron Absorption Cross-sections (barns)	Fast Thermal 46.4 2007	46.4 2007
Neutron flux (neutrons/barn-second)	Fast Thermal 0.3019E-09 0.4334E-10	3828E-09 5220E-10
Average Clad Surface Heat flux (BTU/hour-foot <sup>2</sup> ) (Total heat flux is 102.7% of this value)	196723	BOC 238428 MOC 260658 EOC 247674 AVG 256330
Height Dependent Heat Flux	Figure B-3	Figure B-3
Power Density (W/cc)	103.4	
Relative Power Production	1.00	BOC 1.212 MOC 1.335 EOC 1.259 AVG 1.304
Peak Rod Relative Power Production		AVG 1.38

Appendix B: D Chapman (Westinghouse) Calculation of Plant Operating Conditions.

**Table B-3 (continued)**  
**Data for Diablo Canyon Unit 1 Cycle 11**

Core Average Relative Axial Power Distribution	Height (cm)	Height (in)	Relative Power
	358.67	141.21	0.628
343.41	135.20	0.797	
328.15	129.19	0.932	
312.88	123.18	0.997	
297.62	117.17	1.026	
282.36	111.17	1.039	
267.10	105.16	1.045	
251.83	99.15	1.047	
236.57	93.14	1.049	
221.31	87.13	1.051	
206.05	81.12	1.053	
190.78	75.11	1.055	
175.52	69.10	1.058	
160.26	63.09	1.061	
144.99	57.08	1.064	
129.73	51.07	1.068	
114.47	45.07	1.072	
99.21	39.06	1.076	
83.94	33.05	1.078	
68.68	27.04	1.076	
53.42	21.03	1.059	
38.16	15.02	1.005	
25.44	10.02	0.904	
17.81	7.01	0.815	
7.63	3.00	0.668	

Appendix B: D Chapman (Westinghouse) Calculation of Plant Operating Conditions.

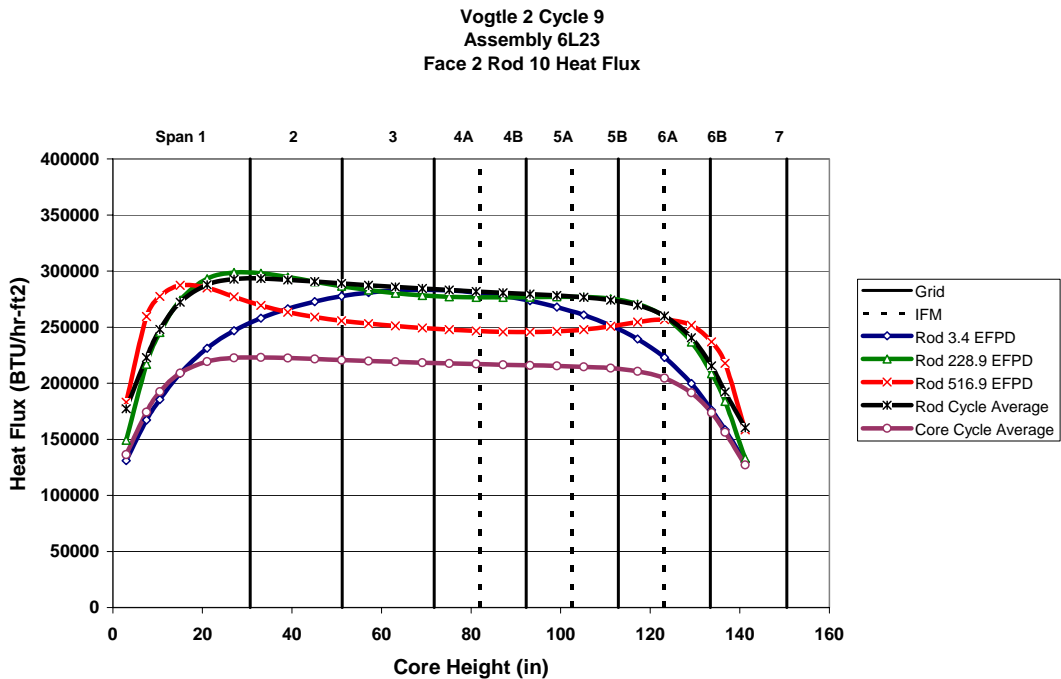


**Figure B-1  
Vogtle Unit 2 Cycle 9 Heat Flux**

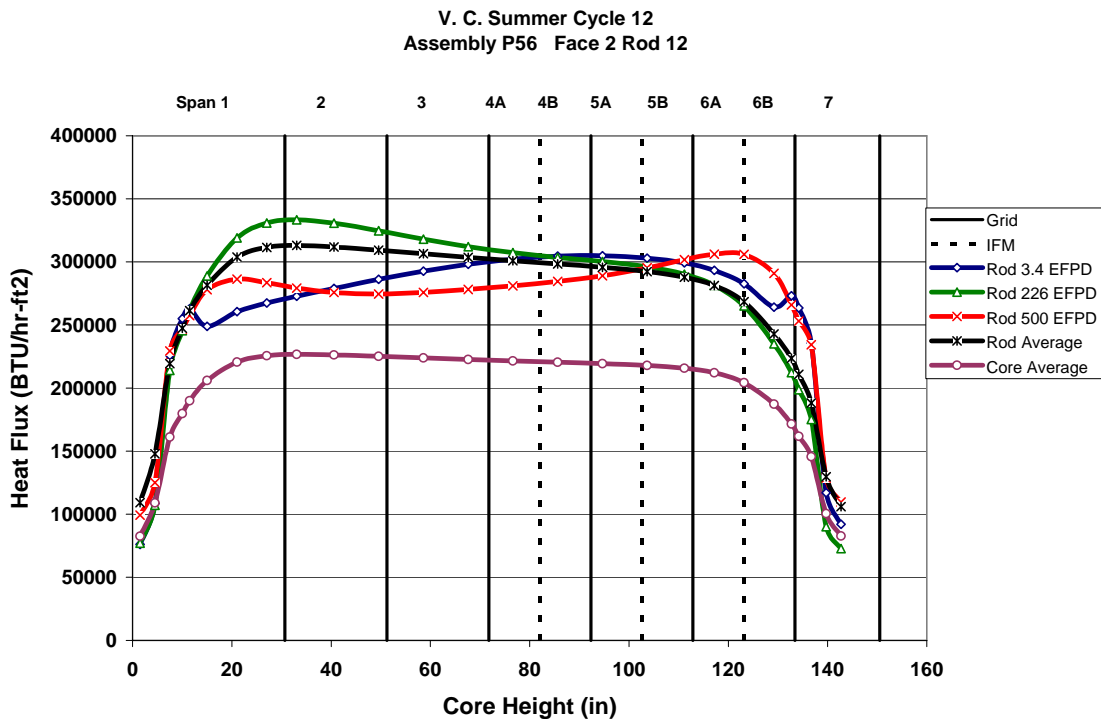


**Figure B-2  
V. C. Summer Cycle 12 Heat Flux**

Appendix B: D Chapman (Westinghouse) Calculation of Plant Operating Conditions.

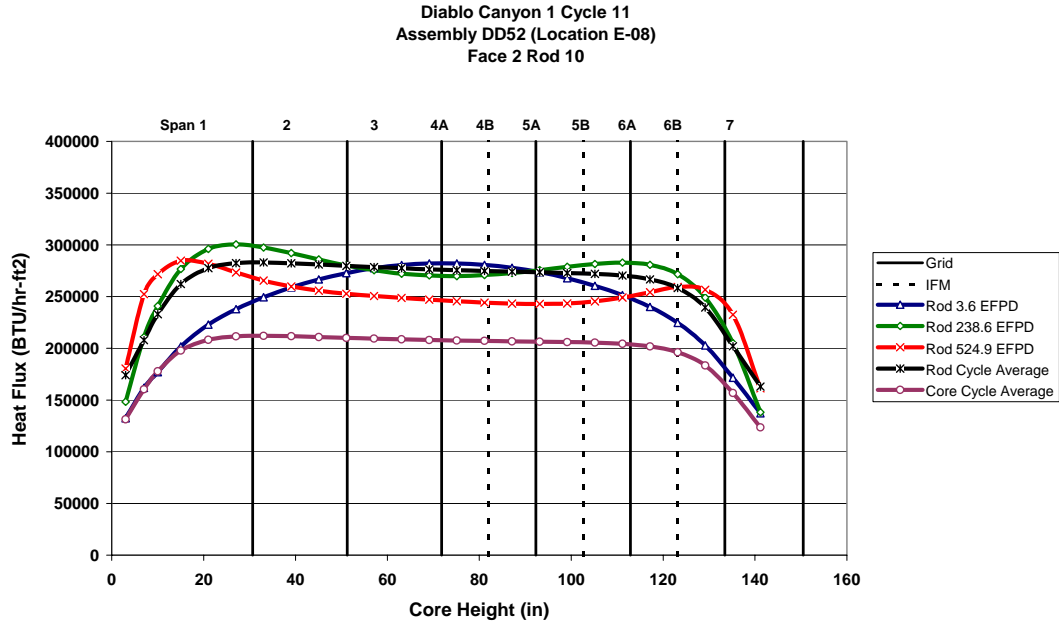


Figure B-3  
 Diablo Canyon Unit 1 Cycle 11 Heat Flux



# C

## APPENDIX C: NUMERICAL SOLUTION OF CCM

---

### Numerical Solution of CCM

This section describes how the equations are prepared for solution by FACSIMILE. The transport and chemical reaction rate equations are solved by the stiff differential equation solver in FACSIMILE, making use of the powerful high-level language facilities to simplify setting up the equations. The thermal hydraulic equations are solved using a stand-alone routine and this will be described first.

#### *Thermal Hydraulic Equations*

The thermal hydraulic equations are solved separately from the rest of the model because they are differential equations in  $x$  and only depend on  $t$  via the dependence of saturation temperature on concentration and the dependence of the properties of water on temperature. The deposit from  $x = 0$  to  $x = d$  is divided into  $n$  elements or cells of length  $h$  and each cell is numbered in the direction of increasing  $x$  from 0 to  $n-1$ .

Differential equation (28) for the temperature profile in the deposit is discretised to give the following series of difference equations for the temperature  $T_i$ ,

$$-T_{i-1} + (2 + h^2 a_i^2)T_i - T_{i+1} = h^2 a_i^2 T_i^s, \quad i = 0..(n-1) \quad (\text{C.1})$$

Here  $T_i^s$  is the saturation temperature and  $a_i^2$  is the value of the parameter defined by equation (56), namely

$$a_i^2 = \frac{2\pi r_c N_c h_i^e}{fk_i^c} \quad (\text{C.2})$$

where  $h_i^e$  and  $k_i^c$  are the values of the evaporative heat transfer coefficient and the thermal conductivity in cell  $i$ . The solution is facilitated by adding fictitious points at  $i = -1$  and  $n$ . The first boundary condition in equation (29) is  $T_{-1} = T_b$  and this together with equation (C.1) for  $i = 0$  gives

$$(2 + h^2 a_0^2)T_0 - T_1 = h^2 a_0^2 T_0^s + T_b \quad (\text{C.3})$$

The second boundary condition in equation (29) is equivalent to

Appendix C: Numerical Solution of CCM

$$\frac{1}{h}(T_n - T_{n-1}) = \frac{q_0}{fk_i^c} \quad (C.4)$$

This together with equation (C.1) for  $i = n-1$  is used to eliminate  $T_n$  to give

$$-T_{n-2} + (1 + h^2 a_{n-1}^2)T_{n-1} = h^2 a_{n-1}^2 T_{n-1}^s + \frac{hq_0}{fk_{n-1}^c} \quad (C.5)$$

Equations (C.1), (C.3) and (C.5) are equivalent to the following set of equations,

$$\begin{aligned} b_0 T_0 - T_1 &= 0 \\ :-T_{i-1} + b_i T_i - T_{i+1} &= c_i \quad \{i = 1..(n-2)\} \\ :-T_{n-1} + b_{n-1} T_{n-1} &= c_{n-1} \end{aligned} \quad (C.6)$$

where

$$b_i = 2 + h^2 a_i^2, \quad i = 0..(n-2) \quad \text{and} \quad b_{n-1} = 1 + h^2 a_{n-1}^2 \quad (C.7a)$$

$$c_i = h^2 a_i^2 T_i^s, \quad i = 0..(n-2) \quad \text{and} \quad c_{n-1} = h^2 a_{n-1}^2 T_{n-1}^s + \frac{hq_0}{fk_{n-1}^c} \quad (C.7b)$$

Equations (C.6) are solved by elimination without pivoting. Consider the following stage of the process where  $T_0 \dots T_{i-2}$  have been eliminated,

$$\begin{aligned} \beta_{i-1} T_{i-1} - T_i &= S_{i-1} \\ -T_{i-1} + b_i T_i - T_{i+1} &= c_i \end{aligned} \quad (C.8)$$

Eliminating  $T_{i-1}$  gives

$$T_i = (S_i + T_{i+1}) / \beta_i \quad (C.9)$$

where

$$\begin{aligned} \beta_0 &= b_0 \quad \text{and} \quad \beta_i = b_i - \beta_{i-1}^{-1}, \quad i > 0 \\ S_0 &= c_0 \quad \text{and} \quad S_i = c_i + S_{i-1} / \beta_{i-1}, \quad i > 0 \end{aligned}$$

Eliminating  $T_{n-2}$  from the last pair of equations (C.6) gives

$$T_{n-1} = S_{n-1} / \beta_{n-1} \quad (C.11)$$

Equations (C.9) and (C.11) along with (C.7) and (C.10) constitute the solution to equations (C.1) for the temperature  $T_i$  in the deposit. It may be shown that this solution, obtained by elimination without pivoting, is always numerically stable, that is, with no growth of rounding errors<sup>(C.1)</sup>.

Equation (31) for the liquid velocity in the porous shell is discretised to give the following set of equations,

$$\frac{1}{h} [\rho_{i+1}^w u_{i+1}^l - \rho_i^w u_i^l] + \frac{b}{2} \left[ \frac{h_{i+1}^e}{H_{i+1}^v} (T_{i+1} - T_{i+1}^s) + \frac{h_i^e}{H_i^v} (T_i - T_i^s) \right] = 0, \quad i = 0..(n-2) \quad (C.12a)$$

$$-\frac{\rho_{n-1}^w u_{n-1}^l}{h} + \frac{b}{2} \frac{h_{n-1}^e}{H_{n-1}^v} (T_{n-1} - T_{n-1}^s) = 0 \quad (C.12b)$$

where  $u_i^l$  is the liquid velocity,  $\rho_i^w$  is the density of water,  $h_i^e$  is the evaporative heat transfer coefficient,  $H_i^v$  is the vaporization enthalpy of water,  $T_i^s$  is the saturation temperature, and the constant  $b$  is given by

$$b = \frac{2\pi r_c N_c}{f} \quad (C.13)$$

Equation (C.13b) was obtained using the boundary condition at  $x = d$ , namely,  $u_i(d) = 0$ . The solution to equations (C.13) is obtained starting with equation (C.13b) to give  $u_{n-1}^l$  and then using equation (C.13a) successively to give  $u_i^l$  for  $i = (n-2)..0$ . This gives

$$u_{n-1}^l = \frac{hb}{2\rho_{n-1}^w} \frac{h_{n-1}^e}{H_{n-1}^v} (T_{n-1} - T_{n-1}^s)$$

$$u_i^l = \left( \rho_{i+1}^w u_{i+1}^l + \frac{hb}{2} \left[ \frac{h_{i+1}^e}{H_{i+1}^v} (T_{i+1} - T_{i+1}^s) + \frac{h_i^e}{H_i^v} (T_i - T_i^s) \right] \right) / \rho_i^w, \quad i = (n-2)..0 \quad (C.14)$$

The vapor velocity  $u_i^v$  is obtained directly from the liquid velocity  $u_i^l$  using equation (36).

Table C-1 compares the numerical solution of the thermal hydraulic equations for the temperature  $T_i$  and fluid velocity  $u_i^l$  with the analytical solution given by equations (55) and (56) in Section 4.1.4. The numerical solution was calculated for a 25  $\mu\text{m}$  thick deposit, a bulk coolant temperature of 345°C and a heat flux of 1 MW  $\text{m}^{-2}$  at the surface of the fuel pin. The values for all the other parameters were typical of those found in a PWR fuel crud deposit and all temperature dependent quantities were held constant. A total of twenty cells were used in the numerical solution and the corresponding analytical values were calculated at the centre of each cell. It can be seen from Table C-1 that the two solutions agree very closely with one another.

In more realistic calculations where the effect of concentration on saturation temperature is included, the temperatures in the cells at the bottom of thick deposits can increase up to such a value that the vaporization enthalpy and the evaporative heat transfer coefficient decrease to

### Appendix C: Numerical Solution of CCM

zero. There is then no evaporative heat transfer in these particular cells. It can also happen, shortly before the evaporative heat transfer coefficient decreases to zero in a cell, that its temperature falls below the local saturation temperature. This temperature reversal is another manifestation of the loss of evaporative heat transfer. When either of these two events occur, it is necessary to switch off evaporative heat transfer in the affected cells. This is done by multiplying the evaporative heat transfer coefficient  $h_i^e$  in the model equations by the parameter  $\theta_i$ , whose value is equal to 1 or 0, depending on whether evaporative heat transfer is switched on or off in cell  $i$ . The parameter  $\theta_i$  also multiplies the liquid velocity  $u_i^l$  in the east transport coefficient to prevent flow into the non-evaporating cells, and to the mass transfer rate constant  $k_i^m$  to prevent liquid to vapor partitioning from these cells.

#### **Transport and chemical kinetic equations**

For the solution of the transport and chemical kinetic equations in the porous shell, the concentrations  $C_i^l$  are referred to the centre of the cells, while the potential gradient  $\phi_i^l$  is referenced to the boundary between cells  $i-1$  and  $i$ . The potential gradient is not referenced to the centre of a cell because the resulting system of equations is numerically unstable. For any dissolved species, the flux from cell  $i$  to cell  $i+1$  is obtained directly from equation (37) as

$$J_i^l = -2D_{i+1}^l \left( \frac{C_{i+1}^l - C_i^l}{h} \right) - \frac{zFD_{i+1}^l}{RT_{i+1}^a} \left( \frac{C_i h_{i+1} + C_{i+1} h_i}{h} \right) \phi_{i+1}^l + u_i^l C_i^l \quad (\text{C.15})$$

The temperature dependent diffusion coefficient  $D_{i+1}^l$  is given by the average of its values in cells  $i$  and  $i+1$ , using the equation

$$D_{i+1}^l = \frac{\varepsilon}{2\tau} (D_i^w + D_{i+1}^w) \quad (\text{C.16})$$

and the temperature  $T_{i+1}^a$  is an average of the deposit temperatures in cells  $i$  and  $i+1$ . This averaging procedure for  $D^l$  and  $T$  proved to be important for maintaining charge balance during the integration by FACSIMILE.

Partial differential equation (49) for the species concentration takes the following form

$$\frac{dC_i^l}{dt} = \left( \frac{dC_i^l}{dt} \right)_R - \left( \frac{dC_i^l}{dt} \right)_P + \frac{(J_{i-1}^l - J_i^l)}{V^l} \quad (\text{C.18})$$

where the transport volume  $V^l$  is given by

$$V^l = \varepsilon h \quad (\text{C.19})$$

In FACSIMILE equation (C.18) is represented by a set of rate equations applied to each cell, representing chemical reactions of the species in solution and its partitioning from liquid to

vapour, together with a transport equation. The transport equation for each species is specified by the volume  $V^l$  together with the east and west coefficients  $e_i^l$  and  $w_i^l$ , defined by

$$J_i^l = e_i^l C_i^l - w_i^l C_{i+1}^l. \quad (\text{C.20})$$

Using equation (C.18) gives

$$e_i^l = D_{i+1}^l \left( \frac{1}{h} - \frac{zF}{2RT_{i+1}^a} \phi'_{i+1} \right) + u_i^l \quad (\text{C.21})$$

$$w_i^l = D_{i+1}^l \left( \frac{1}{h} + \frac{zF}{2RT_{i+1}^a} \phi'_{i+1} \right) \quad (\text{C.22})$$

Discretised equations for the potential gradient, the diffusion current density and the conductivity are obtained straightforwardly from equations (41), (42) and (43) to give

$$\sigma_i \phi'_i = -j_i^D \quad (\text{C.23})$$

$$j_i^D = F \sum z D_i^l \left( \frac{C_i^l - C_{i-1}^l}{h} \right) \quad (\text{C.24})$$

$$\sigma_i = \frac{F^2}{2RT_i^a} \sum z^2 D_i^l (C_{i-1}^l + C_i^l) \quad (\text{C.25})$$

The boundary conditions in the first cell are derived from the following equation for the flux of dissolved species from the bulk coolant into the  $i = 0$  cell,

$$J_b^l = -2D_0^l \left( \frac{C_0^l - C_b^l}{h} \right) - \frac{zFD_0^l}{RT_0^a} C_b^l \phi'_0 + u_0^l \quad (\text{C.26})$$

where suffix  $b$  denotes the value in the bulk coolant above the porous deposit. The diffusion coefficient  $D_0^l$  is given by

$$D_0^l = \frac{\varepsilon}{2\tau} (D_b^w + D_0^w) \quad (\text{C.27})$$

and the temperature  $T_0^a$  is an average of the temperatures in the bulk coolant and cell 0.

The equation for the rate of change of concentration  $C_0^l$  due to the flux  $J_b^l$  is

$$\frac{dC_0^l}{dt} = \frac{J_b^l}{V^l} \quad (\text{C.28})$$

Appendix C: Numerical Solution of CCM

Using equation (C.26), this may be written in the following form

$$\frac{dC_0^l}{dt} = k_{in}^l C_b^l - k_{out}^l C_0^l \quad (C.29)$$

with the rate constants  $k_{in}^l$  and  $k_{out}^l$  given by

$$k_{in}^l = \frac{D_0^l}{V^l} \left( \frac{2}{h} - \frac{zF}{RT_b^a} \phi_0' + u_0^l \right) \quad (C.30)$$

$$k_{out}^l = \frac{2D_0^l}{V^l h} \quad (C.31)$$

Equation (C.23) relating the potential gradient to the current densities applies in cell  $i = 0$ , but the conductivity and the diffusion current density in this cell are given by

$$\sigma_0 = \frac{F^2}{RT_0^a} \sum z^2 D_0^l C_b^l \quad (C.32)$$

$$j_0^D = 2F \sum z D_0^l \frac{(C_0^l - C_b^l)}{h} \quad (C.33)$$

The transport of volatile species in the steam chimney is treated in a similar way to dissolved species in the porous shell. For any volatile species, the flux from cell  $i$  to cell  $i+1$  is obtained directly from equation (51) as

$$J_i^v = -D_i^v \left( \frac{C_{i+1}^v - C_i^v}{h} \right) + u_{i+1}^v C_{i+1}^v \quad (C.34)$$

where  $D_i^v$  is the vapor phase diffusion coefficient in cell  $i$  and the last term in the equation reflects the fact that  $u_i^v < 0$ . The absence of ionic species and the requirement to maintain charge balance coupled with the relatively weak temperature dependence of  $D_i^v$  obviates the need to average its value between consecutive cells. Partial differential equation (54) for the species concentration in the vapor phase takes the following form,

$$\frac{dC_i^v}{dt} = \left( \frac{dC_i^v}{dt} \right)_p + \frac{J_{i-1}^v - J_i^v}{V^v} \quad (C.35)$$

in which the vapor phase transport volume is simply  $V^v = h$ . In FACSIMILE equation (C.35) is represented by a rate equation applied to each cell, representing the partitioning of the volatile species from liquid to vapour, together with a transport equation. The transport equation for each species is specified by the volume  $V^v$  together with the east and west coefficients  $e_i^v$  and  $w_i^v$ , defined by

$$J_i^v = e_i^v C_i^v - w_i^v C_{i+1}^v. \quad (\text{C.36})$$

Using equation (C.34) gives

$$e_i^v = \frac{D_i^v}{h} \quad (\text{C.37})$$

$$w_i^v = \frac{D_i^v}{h} - u_{i+1}^v \quad (\text{C.38})$$

The boundary conditions in the first vapor cell are derived from the following equation for the flux of volatile species from cell  $i = 0$  into the bulk coolant,

$$J_b^v = u_0^v C_0^v \quad (\text{C.39})$$

in which diffusion between the chimney and the bulk coolant has been neglected in comparison with vapor flow. The equation for the rate of change of concentration  $C_0^v$  due to the flux  $J_b^v$  is

$$\frac{dC_0^v}{dt} = \frac{J_b^v}{V^v} \quad (\text{C.40})$$

Using equation (C.39), this may be written in the following form

$$\frac{dC_0^v}{dt} = -k_{out}^v C_0^v \quad (\text{C.41})$$

with the rate constant  $k_{out}^v$  given by

$$k_{out}^v = -\frac{u_0^v}{h} \quad (\text{C.42})$$

## References

- C.1 G D Smith, Numerical Solution of Partial Differential Equations: Finite Difference Methods, Second Edition, Clarendon Press, Oxford, 1984

Appendix C: Numerical Solution of CCM

**Table C-1**  
**Comparison between the analytical and numerical solutions to the thermal hydraulic equations.**

l	Analytical		Numerical	
	T (°C)	u <sub>l</sub> (cm/s)	T (°C)	u <sub>l</sub> (cm/s)
0	345.00	0.318	345.00	0.318
1	345.00	0.318	345.00	0.318
2	345.00	0.318	345.00	0.318
3	345.00	0.318	345.00	0.318
4	345.00	0.318	345.00	0.318
5	345.00	0.318	345.00	0.318
6	345.00	0.318	345.00	0.318
7	345.00	0.318	345.00	0.318
8	345.00	0.318	345.00	0.318
9	345.00	0.318	345.00	0.318
10	345.00	0.317	345.00	0.317
11	345.00	0.317	345.01	0.317
12	345.01	0.317	345.01	0.317
13	345.02	0.316	345.02	0.315
14	345.05	0.314	345.05	0.313
15	345.10	0.309	345.11	0.307
16	345.22	0.298	345.24	0.295
17	345.50	0.274	345.52	0.268
18	346.10	0.221	346.13	0.211
19	347.43	0.104	347.45	0.086

# D

## APPENDIX D: USING THE FACSIMILE CCM

---

### FACSIMILE CCM

This section first outlines the FACSIMILE implementation of the PWR deposit model. It then discusses some problems that were encountered with the model and describes how these were resolved.

The program comprises a number of routines of which the most important is EQUATIONS. This routine is called at every time step during the integration to calculate the time derivatives of the concentrations of the solution, vapor and solid species. The routine lists the chemical reactions amongst the various solution species, followed by the precipitation reactions and then the liquid to vapor partition reactions. FACSIMILE interprets these chemical reactions as rate equations for the concentrations of the products and reactants in each of the  $n$  cells of the deposit. The chemical reactions are followed by the transport instructions for the solution and vapor species. These specify the transport volume and the east and west transport coefficients for each species.

Routine GENERAL is called at the start of each time step to calculate the rate constants and transport coefficients required by EQUATIONS. The routine first calls TDEPARM to calculate some temperature dependent water parameters: liquid and vapor densities, saturation pressure, vaporization enthalpy, thermal conductivity of the deposit and the coefficient of evaporative heat transfer. GENERAL then calculates the non-ideal parameters and the saturation temperature. It then calls THERMHYD to solve the thermal hydraulic equations for the deposit temperature and the liquid and vapor velocities. GENERAL then calls RATES to calculate the temperature dependent rate coefficients and equilibrium constants for the chemical reactions included in the model. GENERAL then corrects the rate constants derived from equilibrium expressions for the change in units between the two and the solution non-idealities. It then calculates the diffusion coefficients for the solution and vapor species. Diffusion coefficients for the solution species are calculated by the method given by Elliot [14], which involves scaling the 25°C values by the ratio of the diffusion coefficients of water at temperature  $T$  and at 25°C. The diffusion coefficients for the volatile species are calculated by the method of Wilke and Lee [D.1]. GENERAL then calculates the potential gradient from the conductivity and diffusion current. This together with the diffusion coefficients and fluid velocities is used to calculate the east and west transport coefficients and the boundary rate constants. The other routines included in the program are concerned with initializing some parameters and variables, and controlling output.

The program is run until a steady state for the solution and volatile species is reached. This typically takes 10 s of model time and from 10 s to around 5 min of actual time. Table 5-1 lists the standard input conditions used for the model runs. The deposit parameters were taken from

### Appendix D: Using the FACSIMILE CCM

Pan et al. [D.2], as typical of those found in PWR fuel crud deposits. The model is always run starting with a deposit thickness of 25  $\mu\text{m}$  divided into 20 cells. The temperature in the bottom cell increases with increasing deposit thickness until the vaporization enthalpy decreases to zero resulting in the loss of evaporative heat transfer. Just before reaching this point, the temperature in the bottom cell will fall below the local saturation temperature. This is another manifestation of the loss of evaporative heat transfer from the bottom cell. This temperature inversion is detected in the last few lines of code in GENERAL and the program brought to a stop. The procedure is then to increase the number of cells from 20 to 21, but to turn off evaporative heat transfer in the last cell. This is done by the method described in Appendix C. In the program the total number of cells and the number of non-evaporating cells are simply controlled by two parameters (#nh and #noff). The program should then run successfully to a steady state with an appropriate temperature distribution in the deposit for one non-evaporating and 20 evaporating cells. Further increases in deposit thickness can then be made by increasing the number of non-evaporating cells, while keeping the number of evaporating cells fixed at 20. It is convenient to refer to such a model as a 20+n cell model. The largest model run to date was a 20+10 cell model for a deposit thickness of 59.1  $\mu\text{m}$ .

The value of n in a 20+n cell model is determined from the thickness of the deposit,  $d_{20+n}$ , according to

$$d_{20+n} = \frac{n+20}{20} d_{20}^{\max} \quad (\text{D.1})$$

where  $d_{20}^{\max}$  is the maximum thickness of a 20 cell model to support evaporative heat transfer throughout. This makes the thickness of the top 20 cells in a 20+n cell model equal to  $d_{20}^{\max}$ . When this is done, it is found that the concentration and temperature profiles in these 20 cells change very little with n. If precipitation of  $\text{LiBO}_2$  is suppressed in the bottom n cells, then the concentration and temperature profiles in the top 20 cells become totally independent of n. This occurs because the fluxes of heat, fluid and concentration at the bottom of the 20 cells in a 20+n cell model become identical to those determined by the boundary conditions in a 20 cell model. The constant thickness of the top 20 cells then ensures that their concentration and temperature profiles are identical to those in the 20 cell model of the same thickness. It was necessary to suppress precipitation in the bottom n cells to ensure zero concentration flux from the top 20 cells.

One particular parameter that must be carefully set in the FACSIMILE program is the error tolerance. If this is set too high, the program will either take a very long time to run or never even finish. On the other hand, if the error tolerance is set too low, the program will either take a long time to finish or else be stopped by a temperature inversion, caused by manifestly ridiculous temperatures. Table D-1 lists the error tolerances used for a series of runs in which the deposit thickness was progressively increased from 25 to 59.1  $\mu\text{m}$ . The table also lists the run time and the model size for each deposit thickness. The three different error tolerances used for 35  $\mu\text{m}$  and the four different values used for the 43.34  $\mu\text{m}$  deposit illustrate the sensitivity of the run time towards this parameter. The reduction in error tolerance from  $10^{-2}$  to  $5 \times 10^{-3}$  in going from a 49.25 to a 59.1  $\mu\text{m}$  thick deposit was mandated by a temperature inversion stop with ridiculous temperatures at the higher tolerance.

When the FACSIMILE program was first tested on thick deposits, it proved impossible to run on deposits thicker than about 45  $\mu\text{m}$ . The problem persisted with greatly simplified versions of the program with most of the chemistry removed. Small changes in deposit thickness close to the value at which failure occurred resulted in large changes in temperature. Such behavior is characteristic of a numerical instability. Moreover, it was found that the temperature and concentration profiles in the top 20 cells of a 20+n cell model depended on n, even though the thickness of the top 20 cells remained constant and there were no precipitation reactions. As explained above, independence of n is guaranteed by the structure of the equations and their boundary conditions; hence, this failure was another symptom of some underlying problem. The root cause of these problems was tracked down by a process of elimination to the temperature dependence of the thermal conductivity of water. This parameter partly determines the thermal conductivity of the deposit,  $k_c$ , which is an important parameter in the equation for the deposit temperature. That this should be the source of a numerical instability is very surprising since the temperature dependence of  $k_c$  is small compared to that of another important parameter in the equation for the deposit temperature, the evaporative heat transfer coefficient. The numerical instability possibly arises as a result of a missing term,  $(d\ln k_c/dT)(dT/dx)^2$ , in equation (4) for the deposit temperature, which occurs when the temperature dependence and therefore the x dependence of  $k_c$  is recognized. However, the magnitude of this term is no more than a few percent of the existing terms in equation (4), so this explanation seems unlikely. The instability problem has been circumvented in the existing program by calculating  $k_c^w$  at the bulk coolant temperature.

**Table D-1**  
**Error tolerances, run times and model sizes used for various deposit thicknesses**

Thickness (mm)	Size	Error tolerance	Run Time (min:s)
25	20	$2 \times 10^{-3}$	0:09
30	20	$2 \times 10^{-3}$	1:41
35	20	$4 \times 10^{-3}$	6:44
35	20	$1 \times 10^{-2}$	2:15
35	20	$4 \times 10^{-2}$	1:10
37	20	$4 \times 10^{-2}$	1:32
39	20	$4 \times 10^{-2}$	2:13
39.40	20	$4 \times 10^{-2}$	2:54
41.37	20+1	$4 \times 10^{-2}$	2:19
43.34	20+2	$4 \times 10^{-2}$	12:51
43.34	20+2	$2 \times 10^{-2}$	5:35
43.34	20+2	$1 \times 10^{-2}$	3:09
43.34	20+2	$5 \times 10^{-3}$	5:44
49.25	20+5	$1 \times 10^{-2}$	
59.10	20+10	$5 \times 10^{-3}$	8:57

*Appendix D: Using the FACSIMILE CCM*

**References**

- D.1 Wilke and Lee, *Ind. Eng. Chem.* 47, 1253 (1955)
- D.2 C Pan, B G Jones, and A J Machiels, Concentration Levels of Solutes in Porous Deposits with Chimneys under Wick Boiling Conditions, Proceedings of the Third International Meeting on Reactor Thermal Hydraulics, October 15-18, American Nuclear Society, 1985

# E

## APPENDIX E: THE $^{10}\text{B}(\text{n}, \alpha)^7\text{Li}$ REACTION

---

The  $^{10}\text{B}(\text{n}, \alpha)^7\text{Li}$  reaction is not only responsible for the neutron flux suppression, but also for local radiolysis caused by the  $\alpha$  and  $^7\text{Li}$  products. In order to calculate the dose it is important to know the reaction rate constant,  $R$ , given by:

$$R = \sigma\phi \times 10^{-24} \quad (\text{E.1})$$

Where

$\sigma$  = reaction cross-section in barns ( $/ 10^{-24} \text{ cm}^2$ )

$\phi$  = neutron flux  $\text{cm}^{-2} \text{ s}^{-1}$ .

In a PWR the neutron energies range from thermal,  $<1\text{eV}$ , to fast neutrons with energies of several MeV. It is necessary to obtain a fission averaged cross-section by summing a number of cross-sections multiplied by the neutron flux for the appropriate fraction of energy spectrum for which the cross-sections apply:

$$\sigma_{\text{ave}} = \sum_{i=1}^n \frac{\sigma_i \phi_i}{\phi_{\text{total}}} \quad (\text{E.2})$$

This procedure may be done over a large range of energy bands, by codes such as WIMS or using a restricted range of energy bands such as “thermal”, “epithermal” and “fast” as done by Polley [E.1], clearly both should give similar answers. It is important to use cross-sections appropriate to the neutron energy ranges being used, for example thermal neutrons are normally taken to be  $2200 \text{ m s}^{-1}$  however that is only true at 293K because at 573K (PWR temperature) the relevant velocity is  $3100 \text{ m s}^{-1}$ . For the  $^{10}\text{B}(\text{n}, \alpha)^7\text{Li}$  reaction, the thermal neutron reactions will be dominant.

The fission averaged, or 1 group, cross-section provided by WIMS calculation is 346 barns, which when using a neutron flux of  $3.6 \times 10^{14} \text{ n cm}^{-2} \text{ s}^{-1}$  gives  $\sigma\phi = 1.25 \times 10^{-7} \text{ s}^{-1}$  ( $t_{1/2} = 25.6 \text{ d}$ ).  $^{10}\text{B}$  dissolved in circulating coolant only spends a fraction of its time in the core (0.05) so it is removed much more slowly than the half-life above implies whereas  $^{10}\text{B}$  deposited on fuel surfaces would react at the above rate. The calculated rate constant compares well with the value calculated by Polley of  $1.47 \times 10^{-7} \text{ s}^{-1}$ .

Appendix E: The  $^{10}\text{B}(n, \alpha)^7\text{Li}$  Reaction

The energy released from the  $^{10}\text{B}(n, \alpha)^7\text{Li}$  reaction can be obtained from the Q value of the reaction, that is, the difference in masses of products and reactants assuming that no major  $\gamma$ -rays are released simultaneously.

**Table E-1**  
Q value for  $^{10}\text{B}(n, \alpha)^7\text{Li}$  reaction

	n	$^{10}\text{B}$	$^7\text{Li}$	$^4\text{He}$	Q, MeV
Mass excess/MeV	8.071	12.052	14.908	2.425	2.79

This decay energy is divided between the Li and He ions. Assuming equal momentum for the fragments gives an energy split of 1.78 MeV  $^4\text{He}$  and 1.01 MeV  $^7\text{Li}$ . These values maybe used for calculation of range and radiation chemical yields. However only 6.35% of the reactions occur without emission of a  $\gamma$ -ray; in the other 93.7%, a 0.48MeV photon is also emitted and so the corresponding  $^4\text{He}$  and  $^7\text{Li}$  energies are 1.48MeV and 0.84MeV respectively. The combined mean energy of  $^4\text{He}$  and  $^7\text{Li}$  is 2.35 MeV.

Taking a  $\sigma\phi = 1.25 \times 10^{-7} \text{s}^{-1}$  and a  $^{10}\text{B}$  concentration of 240 ppm gives an energy deposition of 226 Mrad/h for the combined  $^4\text{He}^{2+}$  and  $^7\text{Li}^{3+}$  radiation, equivalent to a power of 0.63 W/g. In deposits on fuel surfaces where boron may be concentrated by a factor of 10 or more the  $\alpha$  dose rate would be expected to be dominant.

As well as dose-rate it is also important to know the range of  $^4\text{He}^{2+}$  and  $^7\text{Li}^{3+}$  in relevant materials in the deposits in order to know the typical volume affected. Ranges for these particles were obtained using the SRIM program by Ziegler with results shown below:

**Table E-2**  
Particle ranges

Ion	Target	Range/ $\mu\text{m}$ 1.78 MeV $^4\text{He}^{2+}$ 1.01 MeV $^7\text{Li}$	Range/ $\mu\text{m}$ 1.47 MeV $^4\text{He}^{2+}$ 0.84 MeV $^7\text{Li}$
$^4\text{He}^{2+}$	$\text{H}_2\text{O}$ (density $1 \text{ g cm}^{-3}$ ) <sup>*</sup>	9.56	7.91
$^4\text{He}^{2+}$	NiO	2.83	2.22
$^7\text{Li}^{3+}$	$\text{H}_2\text{O}$ (density $1 \text{ g cm}^{-3}$ ) <sup>*</sup>	4.6	4.19
$^7\text{Li}^{3+}$	NiO	1.33	1.1

\* for other densities of water, divide the range by the appropriate density

It will be noted that the ranges of these ions are very small so energy deposition is very localized, but to a certain extent compensated for by the 20% abundance of  $^{10}\text{B}$ .

Another effect is self-shielding because the neutron capture cross-section is relatively high. The flux varies with distance through a sample:

$$I = I_0 = e^{-n\sigma x} \tag{E.3}$$

where  $I_0$  is the incident flux. Taking a cross-section of 340 barns, a density of  $\text{B}_2\text{O}_3$  of  $1.8 \text{ g cm}^{-3}$  gives values for  $I/I_0 = 0.88$  for a thickness of  $100 \mu\text{m}$  – important for reactor operation, but not for the purposes of these calculations.

Finally the radiation chemical yields from radiolysis of water by  $^4\text{He}^{2+}$  and  $^7\text{Li}^{3+}$  ions are needed. There are no experimental measurements in this range of LET in high temperature water. The average LET for the  $^4\text{He}^{2+}$  ions is  $140 \text{ eV/nm}$  assuming the density of water is  $0.75$ . The LET for the Li ions is  $150 \text{ eV/nm}$ . Swiatla-Wojcik and Buxton [E.2] calculated yields as a function of LET for protons resulting from neutron interaction with water. Unfortunately this was for a rather lower LET ( $70 \text{ eV/nm}$ ) than for  $^4\text{He}^{2+}$  and  $^7\text{Li}^{3+}$  ions but it can be reasonably assumed that the only products are  $\text{H}_2$ ,  $\text{H}_2\text{O}_2$  and  $\text{OH}$ , with yields of approximately 1.6, 1.2 and 0.8 molecules/100 eV respectively. In the presence of large  $\beta$ ,  $\gamma$  and  $n$  radiation fields only yields of  $\text{H}_2$  and  $\text{H}_2\text{O}_2$  need be considered because the radical yields from these radiations will be much larger than those from  $^4\text{He}^{2+}$  and  $^7\text{Li}^{3+}$  ions.

## Neutron Fluxes

Polley quotes the following Sizewell B neutron flux values

**Table E-3**  
**Sizewell B neutron fluxes**

Position	Total flux $\text{cm}^{-2} \text{ s}^{-1}$
Core centre	$4.8 \times 10^{14}$
Core outer radius mid height	$2.1 \times 10^{14}$
Core top on axis	$2.2 \times 10^{14}$
Core bottom on axis	$2.3 \times 10^{14}$

Polley also quotes a neutron flux for an average PWR of  $3.65 \times 10^{14} \text{ cm}^{-2} \text{ s}^{-1}$ . This latter value seems a reasonable average until other values become available from Westinghouse. It may be possible to check these values against more recent estimates for Sizewell B.

## References

- E.1 V Polley, private communication
- E.2 D Swiatla-Wojcik and G V Buxton, J. Chem. Soc., Faraday Trans., 94, 2135, (1998)







**WARNING:** This Document contains information classified under U.S. Export Control regulations as restricted from export outside the United States. You are under an obligation to ensure that you have a legal right to obtain access to this information and to ensure that you obtain an export license prior to any re-export of this information. Special restrictions apply to access by anyone that is not a United States citizen or a Permanent United States resident. For further information regarding your obligations, please see the information contained below in the section titled "Export Control Restrictions."

**Export Control Restrictions**

Access to and use of EPRI Intellectual Property is granted with the specific understanding and requirement that responsibility for ensuring full compliance with all applicable U.S. and foreign export laws and regulations is being undertaken by you and your company. This includes an obligation to ensure that any individual receiving access hereunder who is not a U.S. citizen or permanent U.S. resident is permitted access under applicable U.S. and foreign export laws and regulations. In the event you are uncertain whether you or your company may lawfully obtain access to this EPRI Intellectual Property, you acknowledge that it is your obligation to consult with your company's legal counsel to determine whether this access is lawful. Although EPRI may make available on a case by case basis an informal assessment of the applicable U.S. export classification for specific EPRI Intellectual Property, you and your company acknowledge that this assessment is solely for informational purposes and not for reliance purposes. You and your company acknowledge that it is still the obligation of you and your company to make your own assessment of the applicable U.S. export classification and ensure compliance accordingly. You and your company understand and acknowledge your obligations to make a prompt report to EPRI and the appropriate authorities regarding any access to or use of EPRI Intellectual Property hereunder that may be in violation of applicable U.S. or foreign export laws or regulations.

**About EPRI**

EPRI creates science and technology solutions for the global energy and energy services industry. U.S. electric utilities established the Electric Power Research Institute in 1973 as a nonprofit research consortium for the benefit of utility members, their customers, and society. Now known simply as EPRI, the company provides a wide range of innovative products and services to more than 1000 energy-related organizations in 40 countries. EPRI's multidisciplinary team of scientists and engineers draws on a worldwide network of technical and business expertise to help solve today's toughest energy and environmental problems.

EPRI. Electrify the World

**SINGLE USER LICENSE AGREEMENT**

**THIS IS A LEGALLY BINDING AGREEMENT BETWEEN YOU AND THE ELECTRIC POWER RESEARCH INSTITUTE, INC. (EPRI). PLEASE READ IT CAREFULLY BEFORE REMOVING THE WRAPPING MATERIAL.**

BY OPENING THIS SEALED PACKAGE YOU ARE AGREEING TO THE TERMS OF THIS AGREEMENT. IF YOU DO NOT AGREE TO THE TERMS OF THIS AGREEMENT, PROMPTLY RETURN THE UNOPENED PACKAGE TO EPRI AND THE PURCHASE PRICE WILL BE REFUNDED.

**1. GRANT OF LICENSE**

EPRI grants you the nonexclusive and nontransferable right during the term of this agreement to use this package only for your own benefit and the benefit of your organization. This means that the following may use this package: (I) your company (at any site owned or operated by your company); (II) its subsidiaries or other related entities; and (III) a consultant to your company or related entities, if the consultant has entered into a contract agreeing not to disclose the package outside of its organization or to use the package for its own benefit or the benefit of any party other than your company.

This shrink-wrap license agreement is subordinate to the terms of the Master Utility License Agreement between most U.S. EPRI member utilities and EPRI. Any EPRI member utility that does not have a Master Utility License Agreement may get one on request.

**2. COPYRIGHT**

This package, including the information contained in it, is either licensed to EPRI or owned by EPRI and is protected by United States and international copyright laws. You may not, without the prior written permission of EPRI, reproduce, translate or modify this package, in any form, in whole or in part, or prepare any derivative work based on this package.

**3. RESTRICTIONS**

You may not rent, lease, license, disclose or give this package to any person or organization, or use the information contained in this package, for the benefit of any third party or for any purpose other than as specified above unless such use is with the prior written permission of EPRI. You agree to take all reasonable steps to prevent unauthorized disclosure or use of this package. Except as specified above, this agreement does not grant you any right to patents, copyrights, trade secrets, trade names, trademarks or any other intellectual property, rights or licenses in respect of this package.

**4. TERM AND TERMINATION**

This license and this agreement are effective until terminated. You may terminate them at any time by destroying this package. EPRI has the right to terminate the license and this agreement immediately if you fail to comply with any term or condition of this agreement. Upon any termination you may destroy this package, but all obligations of nondisclosure will remain in effect.

**5. DISCLAIMER OF WARRANTIES AND LIMITATION OF LIABILITIES**

NEITHER EPRI, ANY MEMBER OF EPRI, ANY COSPONSOR, NOR ANY PERSON OR ORGANIZATION ACTING ON BEHALF OF ANY OF THEM:

- (A) MAKES ANY WARRANTY OR REPRESENTATION WHATSOEVER, EXPRESS OR IMPLIED, (I) WITH RESPECT TO THE USE OF ANY INFORMATION, APPARATUS, METHOD, PROCESS OR SIMILAR ITEM DISCLOSED IN THIS PACKAGE, INCLUDING MERCHANTABILITY AND FITNESS FOR A PARTICULAR PURPOSE, OR (II) THAT SUCH USE DOES NOT INFRINGE ON OR INTERFERE WITH PRIVATELY OWNED RIGHTS, INCLUDING ANY PARTY'S INTELLECTUAL PROPERTY, OR (III) THAT THIS PACKAGE IS SUITABLE TO ANY PARTICULAR USER'S CIRCUMSTANCE; OR
- (B) ASSUMES RESPONSIBILITY FOR ANY DAMAGES OR OTHER LIABILITY WHATSOEVER (INCLUDING ANY CONSEQUENTIAL DAMAGES, EVEN IF EPRI OR ANY EPRI REPRESENTATIVE HAS BEEN ADVISED OF THE POSSIBILITY OF SUCH DAMAGES) RESULTING FROM YOUR SELECTION OR USE OF THIS PACKAGE OR ANY INFORMATION, APPARATUS, METHOD, PROCESS OR SIMILAR ITEM DISCLOSED IN THIS PACKAGE.

**6. EXPORT**

The laws and regulations of the United States restrict the export and re-export of any portion of this package, and you agree not to export or re-export this package or any related technical data in any form without the appropriate United States and foreign government approvals.

**7. CHOICE OF LAW**

This agreement will be governed by the laws of the State of California as applied to transactions taking place entirely in California between California residents.

**8. INTEGRATION**

You have read and understand this agreement, and acknowledge that it is the final, complete and exclusive agreement between you and EPRI concerning its subject matter, superseding any prior related understanding or agreement. No waiver, variation or different terms of this agreement will be enforceable against EPRI unless EPRI gives its prior written consent, signed by an officer of EPRI.

---

*Program:* 1009734

Nuclear Power

---

© 2004 Electric Power Research Institute (EPRI), Inc. All rights reserved. Electric Power Research Institute and EPRI are registered service marks of the Electric Power Research Institute, Inc. EPRI. ELECTRIFY THE WORLD is a service mark of the Electric Power Research Institute, Inc.

Printed on recycled paper in the United States of America